論文 / 著書情報
Article / Book Information

題目(和文)	X線マイクロトモグラフィーを用いた多孔質内の空隙スケールにおける置換と溶解に関する研究
Title(English)	Pore-scale study of displacement and dissolution in porous media using X-ray microtomography
著者(和文)	HU Yingxue
Author(English)	Yingxue Hu
出典(和文)	学位:博士（工学）, 学位授与機関:東京工業大学, 報告番号:甲第12075号, 授与年月日:2021年9月24日, 学位の種別:課程博士, 審査員:末包 哲也,花村 克悟,岡村 哲至,奥野 喜裕,伏信 一慶
Citation(English)	Degree:Doctor (Engineering), Conferring organization: Tokyo Institute of Technology, Report number:甲第12075号, Conferred date:2021/9/24, Degree Type:Course doctor, Examiner:,,,,
学位種別(和文)	博士論文
Type(English)	Doctoral Thesis

Pore-scale study of displacement and dissolution in porous media using X-ray microtomography

Yingxue HU

A dissertation submitted the Department of Mechanical Engineering

and the committee of graduate studies of Tokyo Institute of Technology

in partial fulfilment of the requirements for

the degree of Doctor of Engineering

Supervisor: Prof. Tetsuya SUEKANE

June 2021

Abstract

A better understanding of multiphase flow in porous media is essential for various geophysical processes, such as CO_2 geological sequestration, soil and groundwater remediation, and enhanced oil recovery. Pore-scale imaging provides new insights on the complex dynamics of two-phase flow and reveals the underlying transport mechanism. In this thesis, an X-ray tomography-based experimental and image analysis method was devised for investigating the displacement and dissolution between two immiscible fluids in natural porous media.

In Chapter 1, we introduced the background of CO_2 geological sequestration, and soil and groundwater remediation. Three typical engineering behaviors involved in the geophysical applications were simplified into three scientific issues, namely drainage displacement, imbibition displacement, and dissolution process. Factors affecting these processes in porous media were discussed and reviewed.

In Chapter 2, the drainage displacement was studied in a three-dimensional porous medium. Three typical drainage displacement patterns were observed, *e.g.*, viscous fingering, capillary fingering, and stable displacement, which is governed by the competition between viscous and capillary forces. Then the pore-scale characteristic of finger structures at breakthrough was quantitatively analyzed, including saturation, finger width, and fractal dimension. According to static features and the dynamic invasion process, a phase diagram for 3D porous media was proposed for the first time. The result will help predict displacement patterns under various fluid properties and flow conditions in natural porous media.

In Chapter 3, a series of imbibition displacements (also known as capillary trapping) were conducted in porous media with various flow rates and particle sizes. Morphological characterizations of trapped bubbles, including residual saturation, bubble size distribution and interfacial area, were determined from reconstructed three-dimensional images. The results show that the critical number of capillary desaturation curves depends on the initial state of the non-wetting phase. A well-connected initial state has a much smaller critical value. In addition, the capillary has a significant effect on the size

distribution of residual phase, and a higher flow rate generate smaller bubbles. The specific interfacial area is proportional to the residual saturation, and the effect of particle size can be normalized by multiplying the median particle diameter.

In Chapter 4, we experimentally elucidated the pore-scale dissolution process and the macroscopic interphase mass transfer coefficient inside a 2D micromodel and a 3D packing. The dissolution process was directly observed inside porous media. Results indicated that not all blobs are equally exposed to flowing water and the dead-end pores considerably decreased the dissolution rate. According to the linear driving force model, the NAPL concentration in mobile water was predicted from the residual saturation. Then, the local and overall mass transfer coefficients corrected with concentration and interfacial area were estimated. The overall mass transfer coefficient was higher in the 3D packing under Darcy flow conditions. The major differences between the 3D packing and 2D micromodel can be attributed to the heterogeneity of pore geometry and the differences in pore connectivity.

In Chapter 5, the impact of wettability of pore surfaces on the residual NAPL dissolution was investigated in natural porous media. Three-dimensional pore-scale characteristics of NAPL blobs were determined in water-wet and neutral-wet media. Time-resolved images enable to estimate the temporal changes in the residual saturation and interfacial area, then to calculate the mass transfer coefficient. The results showed that the wettability has a significant impact on the morphology of residual NAPL; thus, affecting the dissolution behavior in natural porous media. The NAPL dissolution rate in the neutral-wet media is faster due to the higher specific interfacial area and more uniform spatial distribution. However, the wettability has a slight effect on the mass transfer coefficient. At the end, several mass transfer empirical correlations were formulated for dissolution in water-wet and neutral-wet porous media.

The details of the pore scale multiphase flow in porous media revealed with the experimental methods presented here can lead to better fundamental understanding of the physical processes and optimized CO_2 geological sequestration, and soil and groundwater remediation.

Nomenclature

Symbol	Description
A	Interfacial area [m^2]
A_b	Surface area of bubble [m^2]
A_c	Cross-sectional area of porous medium [m^2]
A_n	Interfacial area of non-wetting phase [m^2]
$A_{n\text{-}w}$	Capillary interfacial area [m^2]
A_s	Interfacial area of particles [m^2]
A_w	Interfacial area of wetting phase [m^2]
a	Specific interfacial area [1/m]
a_g	Specific interfacial area of gas [1/m]
a_p	Specific interfacial area of particles [1/m]
Bo	Bond number
C	Bulk aqueous phase concentration [Kg/m^3]
Ca	Capillary number
C_s	Solubility [Kg/m^3]
$C_{x=L}$	Solute concentration at the outlet [Kg/m^3]
D	Molecular diffusivity [m^2/s]
d_{50}	Median particle diameter [m]
D_f	Fractal dimension
d_{pore}	Diameter of pores [m]
G	Sphericity of particles
g	Gravitational acceleration [m/s^2]
H	Distance from inlet [m]
h	Hight of a object [m]
j	Numbering
K	Lumped mass transfer coefficient [m/s]
k	Mass transfer coefficient [m/s]
k_a	Absolute Permeability [1/m]
k_{rw}	Relative permeability
L	Length of the measurement region [m]
l	Length of ganglion [m]
l_c	Characteristic length in dissolution [m]
M	Viscosity ratio
m	Mass [Kg]
N_{cutoff}	Number of bubbles with size lager than cutoff value
$N(s)$	Number of boxes
n	Number of fingers
p	Power law exponent

P_c	Capillary pressure [Pa]
P_{nw}	Pressure in non-wetting phase [Pa]
P_w	Pressure in wetting phase [Pa]
ΔP	Viscous pressure drop [Pa]
Q	Volumetric flow rate [mL/min]
Re	Reynold number
$r_{p.median}$	Median pore radius [m]
r, r_1, r_2	Principal radius of interface curvature [m]
S_i	Saturation of invading phase
S_n	Saturation
S_i^{br}	Saturation of invading phase at breakthrough
S_i^{eq}	Saturation of invading phase at equilibrium state
ΔS_i	Difference saturation at equilibrium and breakthrough
Sh	Sherwood number
Sh_c	Sherwood number calculated with capillary interfacial area
Sh_t	Sherwood number calculated with total interfacial area
Sh'	Modified Sherwood number
s	size of box to calculate the fractal dimension [pixel]
T	Time [s]
Δt	A finite time [s]
V	Volume [m^3]
V_b	Volume of bubble [m^3]
V_{br}	Volume at breakthrough [m^3]
V_{cutoff}	Volume fraction of cutoff size bubble
v	Velocity of water[m/s]
v_i	Velocity of invading fluid [m/s]
$\overline{w}$	Finger width [pixel]
x	Distance from inlet [m]
Δx	A finite length [m]

Greek alphabet	**Description**
θ	Contact angle
θ_n	Volumetric fraction
$\beta_0, \beta_1, \beta_2$	Betti number
σ	Interfacial tension [mN/m]
μ_d	Dynamic viscosity of defending phase [Pa·s]
μ_w	Dynamic viscosity of wetting phase [Pa·s]
μ_{nw}	Dynamic viscosity of non-wetting phase [Pa·s]
μ_i	Dynamic viscosity of invading phase [Pa·s]
ρ_w	Density of wetting phase [Kg/m^3]

ρ_{nw}	Density of non-wetting phase [Kg/m^3]
χ	Euler number
ε	Porosity
τ	Fisher exponent

Abbreviations	**Description**
CDC	Capillary desaturation curve
CDF	Cumulative size distributions frequency
CT	Computed tomography
DDI	Degassed deionized
NAPL	Nonaqueous phase liquid
OTS	Octadecyl-trichloro-silane
PDF	Probability distribution frequency
PP	Plastic particles
ROI	Region of interest
TCE	Trichloroethylene

Contents

Chapter 1. Introduction

1.1 Multiphase flow in porous media

Multiphase fluid flow and transport in porous media are encountered in many industrial and geophysical processes, including geologic carbon dioxide sequestration, enhanced oil recovery, soil and groundwater remediation, transport in polymer electrolyte fuel and membrane system. Groundwater is a vital resource and remediation of contaminated soil and water is critical for protecting human health and stewarding the environment. More than 50% of the world's population rely on it as their drinking water source and even larger than 80% in some regions. Sequestration of carbon dioxide in geological formations is recognized as a key, proven technology to cut greenhouse gas emissions and, hence, prevent global warming. A thorough understanding of these processes is important to achieving sustainable development goals (SDGs), especially for Goal 6: *Clean Water and Sanitation* and Goal 13: *Climate Action*. Therefore, the emphasis in this thesis is on contaminant transport and remediation in soil and groundwater, and geological carbon dioxide storage in oilfields and aquifers.

1.1.1 Soil and groundwater remediation

Currently, soil and groundwater contamination by a variety of organic compounds, such as hydrocarbons, chlorinated solvents, coal tar and creosote, has become one of the major threats to drinking water safety as the increasing use of petroleum products. The contaminant sources are diverse, such as the release of surface spills, industrial accidents and leaking from an underground storage tank and transport pipes of gas and oil (Teramoto et al., 2019). Because of the high oil/water distribution coefficient and low water-solubility, these chemicals are regarded as non-aqueous phase liquids (NAPLs). The NAPLs are classified as light NAPL with a density less than water (LNAPL) or dense NAPL with a density greater than water (DNAPL).

As illustrated in Fig. 1.1, once released into the ground, DNAPL and LNAPL can infiltrate downward through the vadose zone and reach the water table. Because it is less dense than water, LNAPL will typically stop near the water table and be trapped in pore space within the presence of water and air. After penetrating through the water table, DNAPLs will migrate downward further into the groundwater and finally accumulates in the underlying low-

permeability layers. After groundwater flow or water table fluctuations, NAPLs will be trapped in the form of disconnected blobs due to capillary force (Al-Raoush, 2009). The entrapped NAPL blobs become stable against flowing water. Then they serve as a long-term source of groundwater contaminant, because of the low water solubility. The polluted site poses a continuous threat to the safety of downstream drinking water. Every year, billions of dollars are spent on global site surveys and cleanup activities, and millions of dollars are spent on scientific research to improve remediation strategies (AIP, 2003).

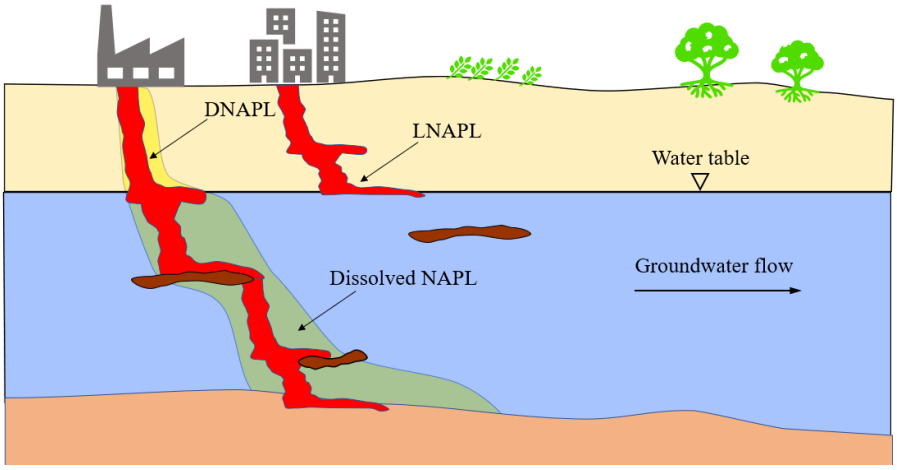

Figure 1.1. Illustration of NAPL migrate downward in soil and groundwater

Many technologies have been developed to remove contaminants from soil and groundwater or convert them into harmless products. According to the treatment procedures and parameters, the remediation methods may be grouped into: (i) Physical treatment technologies, refers to the use of physical remediation methods to remediate soil and groundwater. (ii) Chemical treatment technologies, which can be achieved through a variety of methods, including carbon absorption, ion exchange, oxidation, and chemical precipitation. (iii) Biological treatment technologies are those processes that remove dissolved and suspended organic chemical constituents through biodegradation, as well as suspended matter through physical separation (Speight, 2019). The type and extent of treatment are strongly dependent on the type of the pollution source and the intended use of the water.

Physical treatment technique is a mechanical method including but not limited to: pump and treat, air sparging, and dual-phase extraction (Reddy, 2008). Pump and treat is one of the most common and cost-effective methods to remove a wide range of contaminants (organic solvents,

metals and fuel oil) that are dissolved in groundwater. As illustrated in Fig. 1.2, the process involves installing one or more wells to extract the contaminated groundwater. Groundwater is pumped from the subsurface to the above surface and then is introduced to a holding tank. The treatment system may consist of a single cleanup method, such as air stripping, or granular activated carbon, to clean the water (Speight, 2019). Treatment occurs above the ground, and the cleaned water is either discharged into the surface water system or rejected into the subsurface system.

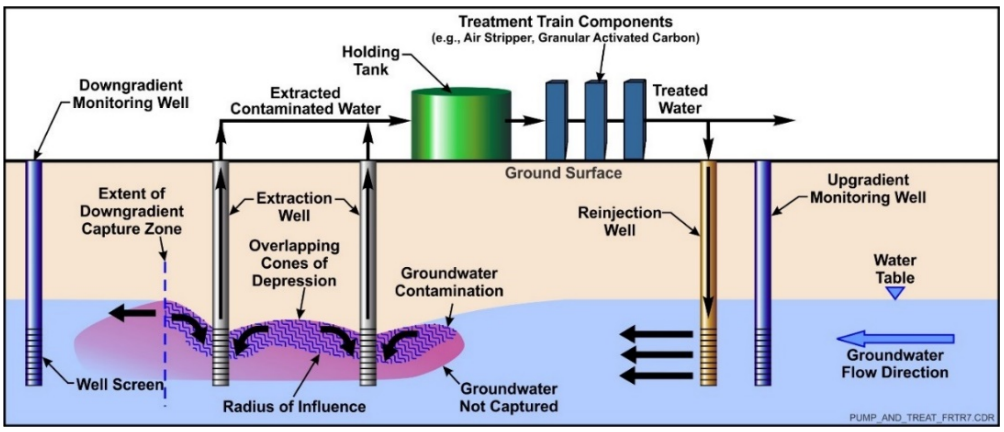

Figure 1.2. Schematic of pump and treat remediation (https://frtr.gov/matrix/Groundwater-Pump-and-Treat/)

Although pump and treat is a safe way of soil and groundwater remediation, it may last a very long time in practice. The main reason is that the trapped NAPL blobs within pore space are very stable against the flowing water and the mass transfer coefficient between NAPL and water is low. To enhance the mobilization and solubility of the entrapped NAPL, surfactant-enhanced remediation methods are usually applied by co-injecting surfactant and water into a reinjection well. The actual cleanup time and efficiency strongly depend on the mass transfer coefficient. The basic process of describing the fate of NAPL in different sites is similar, that is, NAPL migrates downward through the soil, resides in the pore space, and finally dissolves into the groundwater. In other words, NAPL in groundwater involves several typical multiphase flow problems, including drainage, imbibition, and dissolution processes. Thus, a better understanding of the drainage, imbibition, and dissolution behaviors of NAPL are critical to formulating remediation strategies.

1.1.2 Carbon capture and storage

In the past 50 years, the earth's global surface average temperature has risen by approximately 1 degree Celsius (Andrew, 2014). Global warming is believed to be driven by human activities, which increase the concentration of greenhouse gas concentration in the atmosphere, such as methane and carbon dioxide. The main reason for the increase in CO_2 concentration is fossil fuel burning, which currently contributes to 85% of primary energy consumption (IEA, 2012). Under currently proposed policies, it is estimated that by 2035, fossil fuels such as oil, natural gas and coal will still account for 75% of the global energy. The global energy-related CO_2 emissions are expected to rise to 37.0 Gt/yr, which may cause a global temperature rise of 3.6 degrees Celsius (IPCC, 2007).

Carbon capture storage (CCS) is one of the key emission reduction technologies. In order to constrain the global temperature rises less than 2℃ by 2050, many technology areas are developed for the global cumulative CO_2 reduction. As illustrated in Fig. 1.3, modeling conducted by the International Energy Agency (IEA) suggests that CCS is the third-largest single contributor and will need to contribute approximately 14% of the global emissions reductions (IEA, 2017). Among the proposed CCS technologies, the geological sequestration in depleted oil and gas reservoirs and deep saline aquifers appear to be the most promising (Orr, 2009). In this process, CO_2 is compressed into a supercritical state that represents the reservoir condition and then is injected into rock formations to displace the remaining oil or brine, so that the CO_2 can be security sequestrated underground for hundreds to thousands of years.

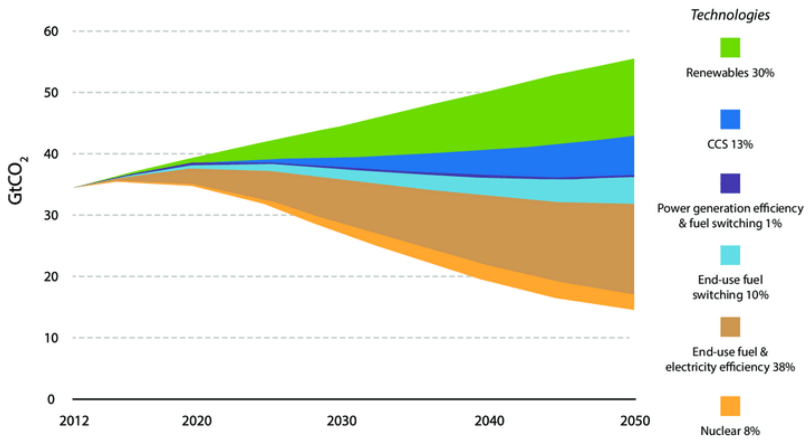

Figure 1.3. Technology area contribution to global cumulative CO_2 reductions as expected by IEA (https://www.iea.org/reports/energy-technology-perspectives-2020)

Recently, the challenge of CO_2 geological storage projects is to improve storage efficiency and prevent potential leakage. Therefore, it is essential to have a thorough understanding of the underground trapping mechanism from multiple scales. Trapping mechanisms can be grouped into physical trapping and chemical trapping. Physical trapping consists of structural and stratigraphic trapping and residual trapping. Chemical trapping consists of solubility trapping and mineral trapping. Fig. 1.4 shows the schematic illustration of fluid dynamics and trapping mechanisms associated with geologic sequestration of CO_2 in saline aquifers. The contribution of different trapping mechanisms varies from site to site and changes dynamically over time. Generally, the physical decrease and the chemical process increase over time, which slowly improves storage security (IPCC, 2007).

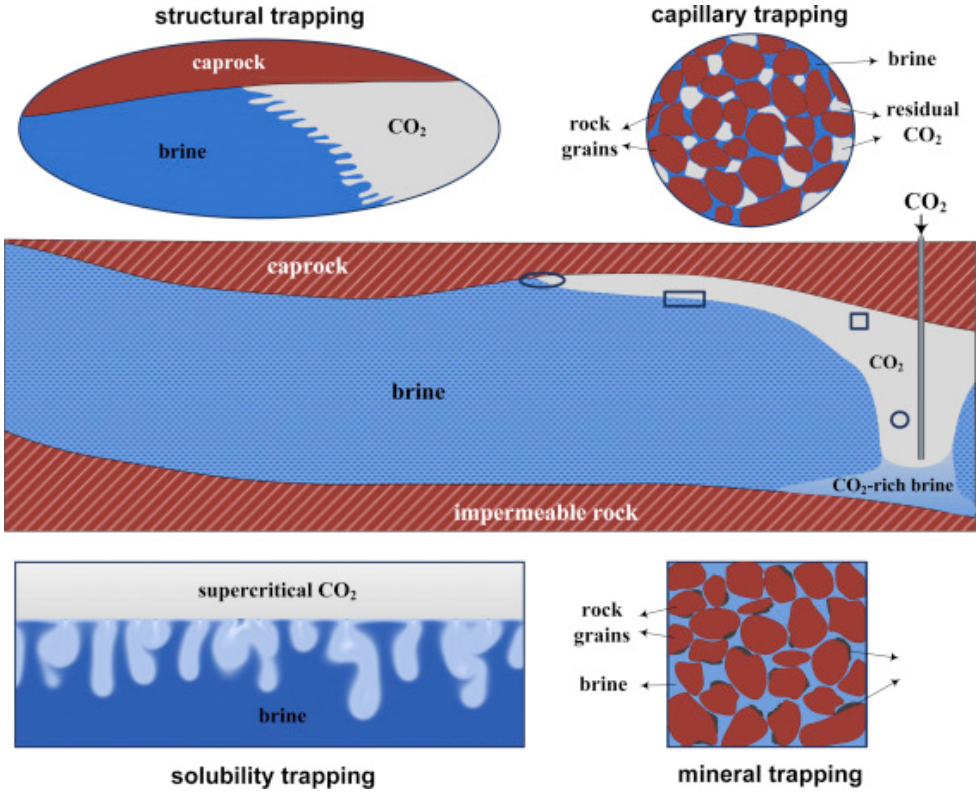

Figure 1.4. Schematic illustration of fluid dynamics and trapping mechanisms associated with geologic sequestration of CO_2 in saline aquifers (Emami-Meybodi et al., 2015).

In the saline aquifer, these four trapping mechanisms work together to store the injected CO_2 safely and efficiently. When supercritical CO_2 is injected into a storage reservoir, it displaces saline formation water and fills the rock's pore spaces. Then, supercritical CO_2 migrates upwards due to its less density than water. The caprock or impermeable layer precludes the

buoyant CO_2 plume from mobilizing upwards to the surface. This process is regarded as structural and stratigraphic trapping, which contributes most of the trapping capacity in the early stage of geological sequestration. Once the injection is stopped, the saline will flow back to the storage site, then the mobilized, well-connected CO_2 will be separated into isolated blobs. These small CO_2 blobs are trapped in pore space and become immobilized, which is the mechanism of capillary (also known as residual) trapping. Dissolution trapping occurs when supercritical CO_2 fluid dissolves into the resident brine of the formation and forms aqueous carbonate species (solubility trapping). These aqueous carbonate species can react with metal cations in the host rock that yields precipitation of the stable carbonate phase. This process is considered to be the mineral trapping mechanism, which is the most permanent and safe form of geological storage. Therefore, a thorough understanding of the flow and transport of CO_2 in saline aquifer is essential to improve the safety of CO_2 geological storage.

1.2 Multiphase flow at pore scale

According to the objectives and methods during the investigation of multiphase flow in the subsurface, the observation scale can be categorized into three scales, namely field-scale, core-scale and pore-scale. Fig. 1.5 shows a schematic diagram of CO_2 flow and distribution after injecting into underground at different scales. Field-scale flow processes are examined in order of hundreds of meters to kilometers depending on the size of the reservoir. As shown in Fig.1.5 (a), field-scale investigations of CCS mainly focus on the spatial and temporal evolution of the CO_2 plume across a storage reservoir with the infectivity, storage capacity and potential pathways for leakage (Middleton et al., 2012). Core-scale flow processes are typically examined in the laboratory at sub-meter to meter length scales. In this scale, Darcy flow approach is usually used to describe the behavior of multiphase flow through homogenous porous media. Pore-scale processes refer to the scale of behaviors taking place within pore space and the length scale is in the order of millimeters to centimeters.

The findings obtained from pore-scale processes are used to understand multiphase flow experiments conducted on the core-scale samples, and then provide valuable information to simulate CO_2 geological sequestration at the field scale. For instance, at the pore scale, viscous forces and capillary forces acting on a single CO_2 bubble control the mobility of CO_2. The balance of viscous forces and capillary forces decides the immiscible displacement patterns, capillary trapping of CO_2 within the pore spaces. When studying multiphase flow in porous

media at the pore level, factors such as capillary pressure, viscous pressure, and wettability should be considered.

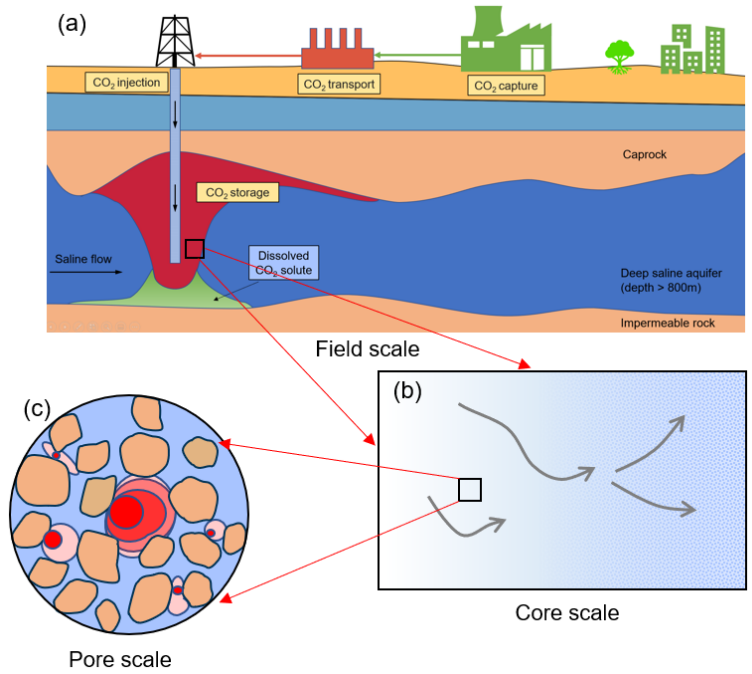

Figure 1.5. Schematic diagram of fluid dissolution in underground at different scale, (a) field scale, (b) core scale and (c) pore scale.

1.2.1 Wettability

Wettability describes the tendency of one fluid to adhere to a solid surface in the presence of other immiscible fluids and is commonly represented by the contact angle (θ). The contact angle is commonly measured from the denser phase. According to the value of contact angle, the fluids are classified into the wetting phase and the non-wetting phase. When a contact angle $\theta < 90°$, it means that the denser fluid is more preferentially spread on the solid surface and is regarded as the wetting phase; when a contact angle $\theta > 90°$, the denser fluid is the non-wetting phase. Various reasons may alternate the solid wettability, such as the heterogeneity of mineral composition of porous media, organic matter distribution, surface roughness, and nonuniform sorption of active agents on the porous media surface. In the geophysical conditions, the wettability of rock surface may vary from strongly water-wet to strongly non-wetting to water, as shown in Table 1.1.

Table. 1.1. Definitions of wettability based on contact angle measurements (Iglauer et al., 2015).

Wettability site	Contact angle (degrees)
Strongly water-wet	0−50
Weakly water-wet	50−70
Neutrally wet	70−110
Weakly non-wetting to water	110−130
Strongly non-wetting to water	130−180

1.2.2 Capillary pressure

Capillary pressure (P_c) is the pressure difference across the curved interface between two immiscible phases arising from the capillary forces. In this study, the two immiscible phases are the wetting phase and the non-wetting phase determined by the contact angle. The capillary pressure is defined as

$$P_c = P_{nw} - P_w, \tag{1-1}$$

where P_{nw} is the pressure in the non-wetting phase, and P_w is the pressure in the wetting phase.

As given by the Young-Laplace equation, the value of P_c depends on the curvature and the interfacial tension (Blunt, 2017), then it can be expressed as

$$P_c = \sigma\left(\frac{1}{r_1} + \frac{1}{r_2}\right), \tag{1-2}$$

where σ is the interfacial tension between the two phases, r_1 and r_2 are the principal radius of the curvature of the interface.

When two phases move in a cylindrical tube with radius r and a contact angle θ, the radius of curvature can be expressed as $r_1 = r_2 = r/\cos\theta$. The capillary pressure is given as

$$P_c = \frac{2\sigma cos\theta}{r}. \tag{1-3}$$

In porous media, the pores and throats are treated as the cylinder, thus the capillary pressure can be calculated from Eq. (1-3).

1.2.3 Viscous pressure

Viscous pressure refers to the pressure drop along the fluid flow caused by the friction between the fluid and the fluid or the fluid and the solid. When analyzing the mobilization of a single

ganglion resided in pores, it is necessary to analyze the force balance acting on the ganglion. At the pore scale, the viscous pressure drop across the ganglion and the capillary pressure between fluids are estimated. The capillary pressure can be calculated from Eq. (1-4) (Datta et al., 2014). According to the Darcy's law, the viscous pressure drop across a ganglion of length l is

$$\Delta p = \frac{\mu_w}{k_{rw}} \frac{Q}{A} l, \tag{1-4}$$

where Q is the volumetric flow rate, A is the cross-sectional area of the porous medium, μ_w is the wetting phase dynamic viscosity, l is the length of the ganglion, k_{rw} is the wetting phase relative permeability. Once the viscous pressure drop across the ganglion beyond the capillary pressure, the ganglion will be displaced from the pore space.

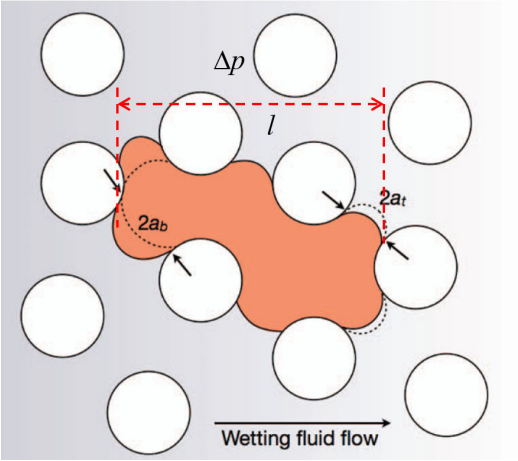

Figure 1.6. Schematic showing a ganglion (orange) trapped within the pore space, with wetting fluid flowing from left to right; beads are shown by white circles (Adapted from Data et al., 2014).

1.3 Displacement and dissolution

Although the goals and strategies for soil and groundwater remediation and CO_2 geological sequestration are different, the main scientific issues involved are similar in these applications. In general, they all belong to multiphase flow in geological porous media. Table 1.2 list three main stages describing the fate of NAPL and CO_2 in the geophysical processes, as well as the corresponding scientific issues. It is worth noting that the natural rock is generally considered to be hydrophilic, therefore NAPL and CO_2 are regarded as the non-wetting phases in subsurface processes. Drainage process describes the released NAPL migrates downward

through the vadose zone, and compressed CO_2 is injected into aquifers. Imbibition process describes NAPL or CO_2 are trapped in the pore space due to the capillary forces. NAPL or CO_2 slowly dissolves into the flowing water are typical dissolution processes.

Table. 1.2. The basic scientific issues involved in soil and groundwater remediation and geological sequestration.

Scientific issue	Geophysical processes	
	Soil and groundwater remediation	Geological sequestration
Drainage	NAPL migrates through the vadose zone	Injecting CO_2 into oilfields and aquifers
Imbibition	NAPL is trapped in pore space	CO_2 is trapped in pore space
Dissolution	NAPL dissolves into flowing water	CO_2 dissolves into brine

1.3.1 Drainage displacement

Drainage refers to the immiscible fluid displacement of a wetting phase by a non-wetting phase in a porous medium. As the non-wetting phase continues to invade the pores initially occupied by the wetting phase, the saturation of the non-wetting phase increases. For example, injecting CO_2 into the aquifer for the first time is a representation of the primary drainage process. To simplify the process, we start with a single pore space that is entirely saturated with the wetting phase and allow a non-wetting phase to enter. Initially, the capillary pressure is insufficient to pass through the narrowest region (throat) of the pore space. As the non-wetting phase is continuously injected into the pore space, the capillary pressure increases progressively. Once the maximum capillary pressure is reached at the throat, the terminal meniscus between the wetting phase and the non-wetting phase passes the throat and then moves rapidly to the adjacent pore at a lower capillary pressure. As shown in Fig. 1.7, the solid arcs in pore 1and the dash arcs in pore 2 represent the terminal meniscus before and after passing through the throat, respectively.

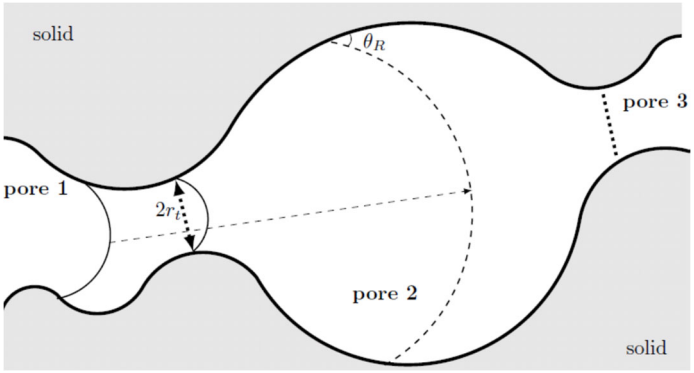

Figure 1.7. An illustration of the primary drainage process, where the wetting phase is placed by the non-wetting phase (Blunt, 2017).

In a real porous medium, it consists of many pores and pore throats, which can usually be represented by a pore network. Assuming the throat is a circular cylinder of radius *r*, then the threshold capillary pressure is $P_c = \frac{2\sigma cos\theta}{r}$, where σ is the interfacial tension, and θ is the receding contact angle. For very slow displacements, the invasion path is controlled by the threshold entry pressures for invasion, where the non-wetting phase can only pass through the widest throats and then progressively the next largest available ones. With the increase of flow rate, the viscous force becomes also important, the pressure difference may force the non-wetting phase into smaller throats. In that case, it is not possible to predict the displacement pattern based on the pore and throat size distribution alone. According to the pioneering work of Lenormand et al. (1988) under drainage conditions, the fluid-fluid displacement is governed by the competition of viscous and capillary forces. The effect of these forces on displacement processes can be characterized by the two most important parameter, the capillary number, $Ca = \mu_i v_i/\sigma$, where μ_i, v_i, and σ are the viscosity, velocity of invading phase, and interfacial tension, respectively; and the viscosity ratio, $M = \mu_i/\mu_d$, where μ_d is the viscosity of the defending phases. In the drainage displacement, the non-wetting phase is the invading phase, and the wetting phase is the defending phase. Experimental and numerical results in the pore network were mapped on a phase diagram with three typical displacement patterns, namely viscous fingering, capillary fingering, and stable displacement, where the axes are the capillary number *Ca* and the viscosity ratio *M* (see Fig. 1.8).

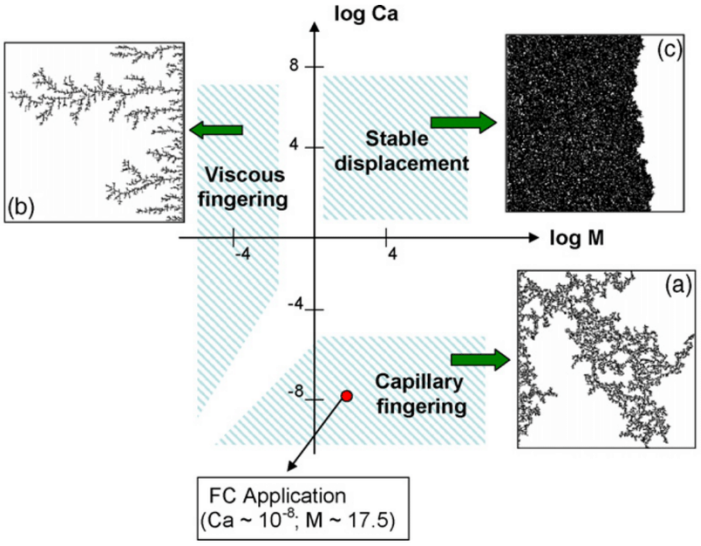

Figure. 1.8. Schematic representation of phase diagram according 2D micromodel experiment (Lenormand et al., 1988).

1.3.2 Imbibition displacement

Related to drainage, imbibition refers to the immiscible fluid displacement of a non-wetting phase by a wetting phase in a porous medium. In a porous medium, the imbibition process can be classified into primary imbibition and second imbibition. Primary imbibition describes the invasion of a wetting phase in a porous medium initially entirely saturated with the non-wetting phase. Second imbibition refers to an imbibition process in a porous medium where some wetting layers are already present in the corner of pores and throats. In the geophysical processes, it is more normal to encounter secondary imbibition. In this thesis, imbibition process specifically refers to the secondary imbibition.

As shown in Fig. 1.9, there are two distinct processes in the secondary imbibition, namely snap-off and piston-like displacement. Snap-off occurs when the corner wetting layers continue to swell, and the well-connected non-wetting phase is disconnected into many isolated blobs. Then the non-wetting phase can become trapped in the larger pores. High pore-to-throat aspect ratio facilities the snap-off event. Piston-like displacement describes the process where the non-wetting phase is completely displaced from the pores and throats. Piston-like displacement alone leads to a rather flat advance of fluid and very little trapping (Blunt, 2017).

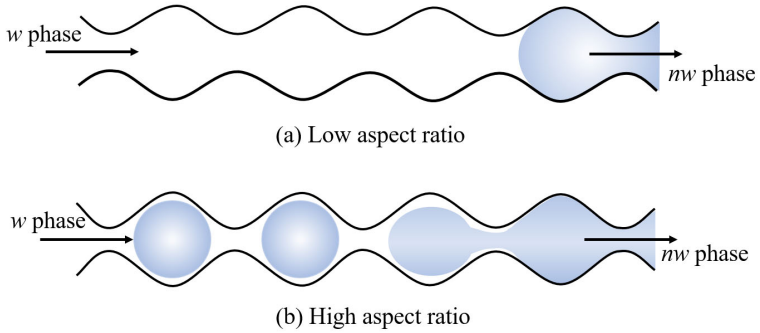

Figure 1.9. Piston-like displacement in low aspect ratio (up image) and snap-off in high aspect ratio (down image) during the imbibition process.

The competition between these two distinct processes controls the residual saturation, cluster size distribution and morphology of trapped non-wetting phase during imbibition processes (Blunt, 2017). In the CO_2 geological sequestration, snap-off is the primary mechanism of residual trapping, which will have a large contribution to the security of CCS. While in the soil and groundwater remediation, a large amount of NAPL blobs will be trapped after snap-off, resulting in a lower efficiency of clean up. The influence of initial saturation on the residual saturation of the non-wetting phase is described in the capillary trapping curves, according to core-flooding experimental results (Mansoori et al., 2009; Pentland et al., 2010; Suekane and Nguyen, 2013). In addition, the pore structure (e.g., topology (Herring et al., 2013), connectivity (Guo et al., 2018) and pore-throat aspect ratio (Wardlaw and Yu, 1988)), roughness (Geistlinger et al., 2016), and wettability (Herring et al., 2016) inside porous media also exert a significant effect on displacement mechanism. The flow rate and fluid properties have an important impact on the competition of these two distinct processes. The capillary desaturation curves describe the relationship between the flow rate and the residual saturation. It has received widespread attention since decades ago due to its importance for EOR. However, a few studies have examined the capillary desaturation curve from a pore-scale perspective in porous media.

1.3.3 Dissolution process

Dissolution is a mass transfer process in which a gas, liquid, or solid phase dissolve into a solvent to form a solution. Dissolution occurs at a non-equilibrium state and equilibrium state (Chang et al., 2019, 2016). During the drainage and imbibition processes, the mass transfer occurs at the movement interface between the non-wetting phase and the wetting phase. After

NAPL or CO_2 is trapped in the pore space, the mass transfer occurs at a relatively fixed interface, since the trapped phase becomes immobile. In the real reservoir, CO_2 is compressed into a liquid or supercritical state. In this study, we only conduct the experiment at ambient pressure and room temperature. Thus, we studied the dissolution process between NAPL and water in porous media to mimic liquid-liquid mass transfer behavior.

Over the previous few decades, many attempts have been made to model the dissolution process of the entrapped NAPL in porous media from pore scale to field scale (Agaoglu et al., 2015). The dissolution of the single-component NAPL in groundwater is influenced by many factors, including the solubility, interfacial area, and flow velocity. Based on the mass balance equation, the interphase mass transfer rate coefficient can be described by using the linear driving force model (see Fig. 1.10),

$$-\frac{d_m}{d_t} = kA(C - C_s), \tag{1-5}$$

where d_m/d_t is the mass transfer of NAPL dispelled into the water, k is the mass transfer coefficient, A is the effective NAPL-water interfacial area, and C is the bulk aqueous phase concentration, and C_s is the solubility of NAPL in water.

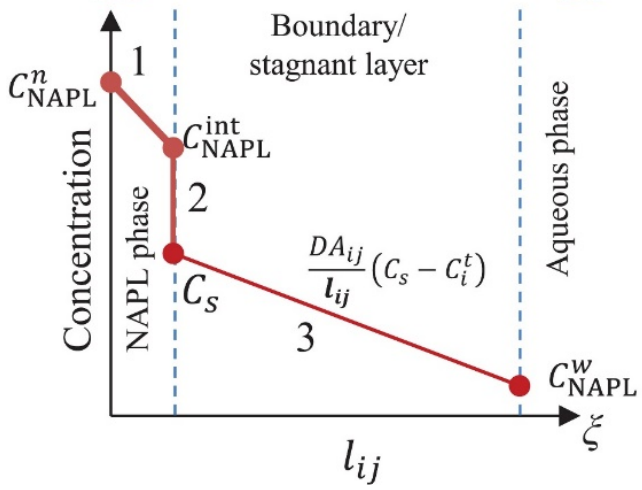

Figure 1.10. Schematic diagram of linear driving force model of dissolution process (Aminnaji et al., 2019).

In previous studies, dissolution experiments were mainly conducted in opaque sand packings at core scale. The dissolved phase concentration was measured from the effluent and the amount of trapped phase was determined by gravimetrical measurement. It was considerably

difficult to directly and accurately measure the interfacial area inside porous media because of the heterogeneous pore structures and limitation of experimental apparatus. Therefore, the mass transfer rate was estimated by using only the lumped mass transfer coefficient ($K = ka$), which is the product of the mass transfer coefficient k and specific interfacial area a (Miller et al., 1990). k and K are often expressed as dimensionless numbers, Sherwood number Sh and modified Sherwood number Sh', respectively:

$$Sh = kl_c/D, \tag{1-6}$$

$$Sh' = Kl_c^2/D, \tag{1-7}$$

where l_c is the characteristic length scale and D is the molecular diffusivity in water.

Several empirical correlations have been proposed that correlating Sh' with relevant system parameters in column experiments. Most of these correlations ignored the effect of the spatial distribution of residual phase on the dissolution process. The interfacial area exhibits a complex interdependency with the morphology of the trapped NAPL because of the highly heterogeneous pore structures. The local dissolution behavior at the pore scale cannot be accurately described using the lumped mass transfer coefficient and assumption model.

1.4 Research objectives

The aim of this work is to investigate the displacement and dissolution processes in porous media from a pore-scale perspective and their implications on the geological applications, such as soil and groundwater remediation, and CO_2 geological sequestration. In the last decades, much attention has been paid to these processes from core-scale to field scale; however, the pore-scale has received less attention, as the opaque porous media bring a challenge for direct observation. Recently, with the development of nondestructive visualization technologies (see Appendix 1), pore-scale multiphase flow studies are conducted to reveal the underlying mechanism and to provide benchmark data for large-scale modeling. There are still some questions that are unclear and need to be addressed:

1. What happens during drainage displacement in 3D porous media?

2. Can the phase diagram obtained from 2D media be used to predict the displacement patterns that occur in 3D media?

3. How does the injection strategies affect the capillary desaturation curves?

4. How doses flow rates affect the morphology of the residual phase?

5. How does pore structures affect the dissolution process?

6. How does wettability affect the dissolution process?

To address these questions, a laboratory-based X-ray tomography experimental and image analysis method was devised for investigating pore-scale displacement and dissolution processes. This thesis is organized as follows:

Chapter 1 provides the background information of multiphase flow in porous media. Two specific geological applications related to the *Sustainable Development Goals* were emphasized.

Chapter 2 demonstrates the results of drainage displacement in a 3D porous medium with a wide range of capillary number and viscous ratio. The pore-scale characterizations of static and dynamic displacement patterns were analyzed. A phase diagram was then proposed to identify viscous fingering, capillary fingering, and stable displacement in 3D media at various conditions.

Chapter 3 examines the effect of capillary number on morphological characterizations of the residual phase in porous media. Two injection strategies were compared to identify the influence of initial states on capillary trapping and blobs remobilization. The universal characterizations of the residual phase were summarized from various porous media.

Chapter 4 visualizes the dissolution process of residual NAPL inside a 2D micromodel and a 3D packing, where the pore structures have significant differences, such as dimensionality, pore connectivity and coordination number. The empirical correlations of mass transfer coefficient in porous media with different pore structures were formulated.

Chapter 5 examines the influence of wettability on the dissolution of NAPL inside natural porous media. The pore-scale features of NAPL blobs in water-wet and neutral-wet systems were compared. In the end, the empirical mass transfer coefficient in natural porous media with different wettability was summarized, which provides the benchmark data for large-scale modeling.

Chapter 6 presents the conclusions of this research and provides some possible future works.

Chapter 2. Drainage displacement patterns and phase diagram in 3D porous media

In this chapter, we experimentally studied the drainage displacement in porous media with a wide range of capillary number *Ca* and viscosity ratio *M*.

2.1 Introduction

According to the pioneering work of Lenormand et al. in 2D micromodels (Lenormand et al., 1988), the fluid–fluid displacement is governed by the competition of viscous and capillary forces. Experimental and numerical results in the pore network were mapped on a phase diagram with three typical displacement patterns, namely viscous fingering, capillary fingering, and stable displacement, where the axes are the capillary number *Ca* and the viscosity ratio *M*. Similar works were supplemented to improve the accuracy of the phase diagram with a micromodel experiment and a numerical simulation (Liu et al., 2013; Zhang et al., 2011). In addition to micromodel, Chen et al. (2018, 2017) experimentally investigated the two-flow in rough fractured media and proposed a full phase diagram from unfavorable (Log$M$ < 0) to favorable displacement (Log$M$ > 0) conditions. Although, many other reservoir parameters, including interfacial tension, surface roughness, wettability, and heterogeneity of media, also play a significant role on the displacement patterns (Hu et al., 2017a, 2017b; Jiang et al., 2014; Wang et al., 2018; Zhao et al., 2016). The phase diagram proposed by Lenormand et al. (1988) and Zhang et al. (2011) generally provides researchers a pithily and reliable reference to define immiscible fluid–fluid displacement patterns in 2D porous media.

In these literatures (Chen et al., 2018, 2017; Hu et al., 2017a, 2017b; Jiang et al., 2014; Lenormand et al., 1988; Liu et al., 2013; Wang et al., 2018; Zhang et al., 2011; Zhao et al., 2016), the 2D micromodel was treated as the porous media to directly observe the dynamic behavior of the invading fluid, where only the viscous and capillary forces were considered. However, the situation will become more complex in 3D porous media, such as in natural sandstones and packed beds. In 3D porous media, when the density difference of invading and defending fluid is large, the buoyancy force has a significant effect on the displacement processes (Wilkinson, 1984).The inherent pore structures (i.e., pore size distribution and connectivity) is influenced by the system dimension, which further affects fluid behaviors in porous media. The penetration process is mainly controlled by the pore size and pore

connectivity. For two fluids immiscible displacement, the displacement efficiency in heterogeneous pore networks is lower than in homogeneous one, resulting from the heterogeneity weakens the displacement stability (Liu et al., 2015).

For a highly heterogeneous 3D porous media, the mechanism of immiscible fluid displacement process is not yet fully understood. The numerical method, such as lattice Boltzmann method (LBM), smoothed particle hydrodynamics (SPH), and finite volume method (FVM), provides a high temporal and spatial resolution to investigate the pore scale events, such as Haines jumps, snap-off, and pore filling events (Armstrong et al., 2015; Singh et al., 2017; Yamabe et al., 2015). Many researchers have recently applied numerical method to simulate the immiscible fluid displacement process in digital rocks (Bakhshian et al., 2019; Tsuji et al., 2016; Yamabe et al., 2015; Zacharoudiou et al., 2018). Tsuji et al. performed a series of simulations on the two-phase fluid displacement patterns in a Berea sandstone under various reservoir conditions (Tsuji et al., 2016). Stable displacement was not observed in the 3D porous media, while it could be found in the 2D homogeneous model at the same condition. The difference may be caused by the pore connectivity and coordination number in a 3D system is higher than that of a 2D system. However, the computation source limits the scale of porous media to hundreds of microns, which are even far smaller than the laboratory scale. For a model with a length is only 1.2 mm, sometimes the calculation must be terminated in advance to save the computing resources under low *Ca* conditions (Tsuji et al., 2016). In previous literatures studying immiscible displacement in 3D porous media (Armstrong et al., 2015; Bakhshian and Hosseini, 2019; Singh et al., 2017; Tsuji et al., 2016; Yamabe et al., 2015), the capillary number and the viscosity ratio only reached a relatively small range compared with the laboratory experiments (e.g., Log$M = -4.7 - 2.9$ in Lenormand et al.'s work (Lenormand et al., 1988)).

Thus, it is necessary to study the immiscible fluid–fluid displacement patterns for 3D porous media with a broad range of *Ca* and *M*. In addition, the main research on the 3D drainage process were mainly numerical simulation and few experimental studies had been reported.

2.2 Materials and methods

2.2.1 Porous media

An unconsolidated packed bed was chosen as a porous medium for the drainage displacements. Glass beads fabricated with soda lime glass have an oil-wet surface (BZ-04, As-one, Inc., Japan). The typical diameters of the particle, pore, and throat are 400 µm, 300 µm, and 100 µm, respectively (Fig. 2.1). The same glass beads washed with toluene, ethanol, and water to remove the chemical coating, were treated as the water-wet porous medium for the favorable displacement (Setiawan et al., 2014). The packed bed was assembled by pouring the particles into an acrylic resin cylinder with an inner diameter of 10 mm to a height of 16 mm. During particle pouring, the cylinder was kept shaken to make the packed bed more compact. Fine beads were filled near the inner tube forming a low permeable layer to avoid the invading fluid from preferably passing through near the tube wall (Fig. 2.2). Two thick sintered glass filters were placed at the bottom and top of the packed bed, which not only can provide a uniform fluid distribution, but also support the unconsolidated structure.

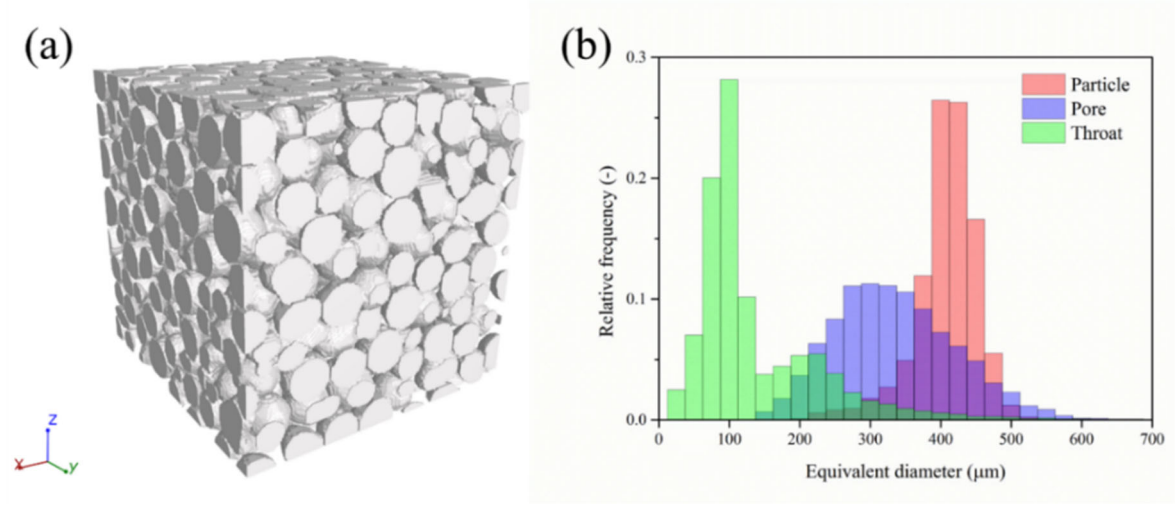

Figure 2.1. The glass bead packing used in this experiment. (a) 3D structure reconstructed from the micro-CT images (b) Particle, pore, and throat diameter distributions of the packed bed.

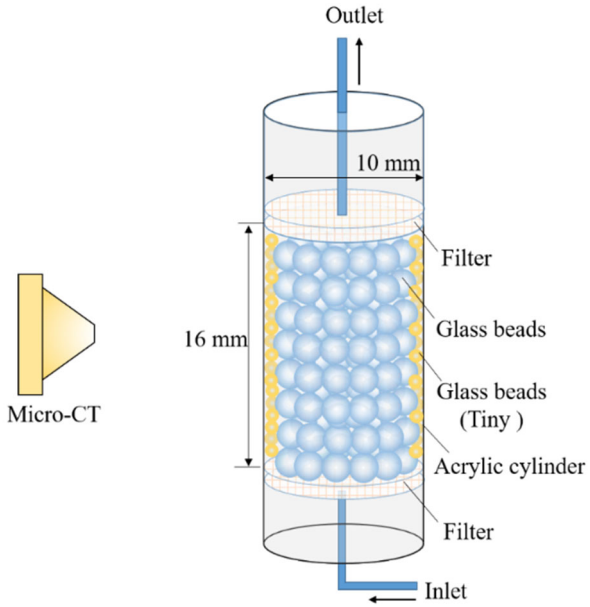

Figure 2.2. The apparatus used to conduct the two-phase immiscible drainage experiment in an unconsolidated porous medium.

2.2.2 Fluid pairs

Water and silicone oil were chosen as the fluid pairs to investigate the immiscible fluid–fluid displacement in the porous media. Silicone oil is available with a broad range of viscosity from 0.65×10^{-6} to 1.0 m^2/s depending on the polymer length (Barca et al., 2014). Five kinds of silicone oil were selected herein: KF-0.65, KF-10, KF-100, KF-1 000, and KF-10 000 (Shin-Etsu Chemical Co., Ltd). The corresponding density ranged from 760 to 975 kg/m^3. To eliminate the buoyancy effect, a proportionate of tetrachloroethylene (PCE) was mixed with the silicone oil to match the density of water. 1-Iododecane was added to the silicone oil to enhance the contrast with water during the micro-CT scan. Table 2.1 presents the mass fraction of the three components and the mixture density. The largest density different between water and the mixture is only 40 kg/m^3, corresponding $Bo = 1.18 \times 10^{-3}$ ($Bo = gl^2\Delta\rho/\sigma$, where g is the gravitational acceleration; l is the characteristic pore size; $\Delta\rho$ is the fluid density difference; and σ is the interfacial tension). The buoyancy effect on the displacement patterns could be ignored in this study. Deionized water and five kinds of mixtures were selected with viscosity ratio ranging seven orders of magnitude. Table 2.2 presents the physical properties of these fluid pairs.

Table 2.1. Summary of the mixture properties

	Mass fraction			Silicone oil	ρ (kg/m^3)
	Silicone oil	1-Iododecane	PCE		
Fluid -1	96%	4.0%	-	KF-10 000	973
Fluid -2	96%	4.0%	-	KF-1 000	969
Fluid -3	96%	4.0%	-	KF-100	965
Fluid -4	87.9%	3.7%	8.4%	KF-10	965
Fluid -5	58.9%	-	41.1%	KF-0.65	960

Table 2.2. Summary of the fluid pairs

Exp.	Defending phase	Invading phase	Wettability	μ_i[a] (mPa·s)	μ_d[a] (mPa·s)	Log$M$	σ[b] (mN/m)	Bo
1	Fluid -1	Water	Oil-wet	9451	1.00	–4.0	35.9	6.63E–04
2	Fluid -2	Water	Oil-wet	940	1.00	–3.0	35.9	7.60E–04
3	Fluid-3	Water	Oil-wet	90.0	1.00	–2.0	35.9	8.60E–04
4	Fluid -4	Water	Oil-wet	9.23	1.00	–1.0	34.5	8.95E–04
5	Fluid -5	Water	Oil-wet	0.73	1.00	0.2	29.8	1.18E–03
6	Water	Fluid -4	Water-wet	1.00	9.23	1.0	34.5	8.95E–04
7	Water	Fluid -5	Water-wet	1.00	90.0	2.0	35.9	8.60E–04

[a] Viscosity was measured with viscometer at 20°C (SV-10)

[b] Interfacial tension was measured at 0.1MPa and 20°C (DAS25S)

2.2.3 Experimental procedures

Prior to each experiment, the sample was placed into the vacuum chamber, forming the initial situation that the packed bed was completely saturated by the defending phase. The outlet of the sample was blocked up, and the inlet was immersed in the defending phase fluid. The vacuum chamber valve was opened after no bubble could be observed in the defending phase fluid for 10 min. The pressure difference between inside and outside the sample pushed the fluid into the pore. Before the invading fluid was introduced through the inlet, the packed bed saturation was carefully checked according to the CT images.

In the drainage process, the invading fluid was upwardly injected with a syringe pump (IC3100, KD Scientific, Inc.), and the corresponding capillary number varied from LogCa = −8 to

LogCa = −2. At high Ca condition, a breakthrough occurs after a very short injection time. It is hard to catch the 3D images of breakthrough time under continues injection conditions, due to the limitation in our micro-tomography. Thus, a discontinuous injection method was implemented, where an interval volume fluid was injected, then stopped and scanned. The process was repeated until the invading phase reached the outlet, and this is referred as the breakthrough time. In some cases, the injection process was continued after breakthrough to investigate the invasion dynamics for the typical viscous and capillary fingerings. Under continuous flow condition, the saturation of the invading fluid increases until reaches a steady state, which is referred to as the equilibrium state.

2.2.4 Image processing

Micro-tomography with a micro-CT (ScanXmate-RB090SS, Comscantechno Co., Ltd.) was used to visualize the fluid morphology during the displacement process. Each scan captured 992 images along a 360° rotation in approximately 125 s, enabling the production of a 3D image of the packed bed with an image resolution of 992 × 992 × 992 voxels (16.491 μm/pixel). All images were collected after the invading phase was injected. This image resolution corresponded to 16.36 × 16.36 × 16.36 mm^3, which was enough to capture the whole packed bed region. The same X-ray intensity, 8.12 W (I = 116 μA, V = 70 kV), was used for all the experiments. The packed bed sample remained vertical during the scanning, while the X-ray source and detector rotated horizontally.

The raw images were filtered to remove the noise and preserve the edges using a non-local means filter (Buades et al., 2011; Darbon et al., 2008). A simple gray-scale segmentation algorithm according to the 2D histogram was used. In this case, the simple segmentation method was enough to separate the solid and fluid phases because the particle shape was regular. After being filtered, the pore and the solid were first separated, and the threshold value was set to match the porosity measured with the weighing method (ε = 0.37). The watershed algorithm was used to define the individual pore and particle. The diameter of the pores and the particles were then described by way of the equivalent sphere diameter with the same volume. Figure 1 presents detailed information on the packed bed, including the probability density function of the pore, throat, and particle.

Accurately segmenting the two fluid phases from the pore space was quite difficult, especially when the image resolution was not very high (Sheppard et al., 2004). The gray value in the

acquired images increased from water, silicone oil, to particles because of the difference absorption of X-ray. A pseudo-interface was found between the particles and the water, like the oil film covering the particles (Andrew, 2014). The captured images' resolution (16.49 μm/pixel) was not enough to observe the thin oil film (~ 1 μm) (Krummel et al., 2013); thus, the pseudo-interface was treated as water using the followed procedure. An automated calculated threshold value was introduced to separate the water and oil phases in ImageJ programs (NIH Image). The water and particle regions were then dilated twice following a Boolean intersection, and the pseudo-interface was obtained. The Boolean result was added to the primary water region. After that, the particle image was taken as a reference to remove overvaluation using a Boolean subtraction. The saturation of invading phase was measured from these obtained images. Then the spatial structure reconstructed from images stack was applied to estimate the fractal dimension and the finger width. The detailed estimation method will be discussed in below.

2.3 Viscous fingering, capillary fingering, and stable displacement

Fig. 2.3 shows the visualization of the displacement patterns at the breakthrough time for a wide range of capillary number and viscosity ratio, including favorable and unfavorable displacements. The capillary number decreased from the top row to the down row with seven orders of magnitude (LogCa ranges from −8 to −2), and the viscosity ratio increased from the left column to the right column with seven orders of magnitude (Log$M$ ranges from −4 to 2). Three typical displacement patterns, namely viscous fingering, capillary fingering, and stable displacement were observed.

2.3.1 Static displacement patterns

***Viscous fingering*:** The displacement of the defending phase by the invading phase is widely recognized to exhibit viscous fingering under high Ca and low M condition, because of the competition between the capillary and viscous forces (Saffman and Taylor, 1958). In the regime of viscous fingering (upper-left in Fig. 2.3), thin fingers followed a number of preferential flow path in the same direction as injection and no backward movement. To note, many invading phase discrete ganglions were observed at the lowest viscosity ratio (Log$M$ = −4) with a relatively high capillary number (LogCa = −6, −5, and −4). The snap-off event during drainage process leads to these discrete ganglions, which can also be found in 3D

simulation and experimental results (Bakhshian et al., 2019; Herring et al., 2018). The behavior of viscous fingering is principally controlled by viscous forces due to the viscosity of the defending phase. When the velocity of the invading phase is high, the front of displacement advances very fast and soon reaches the outlet. Thus, the saturation of viscous fingering is usually lower than capillary fingering and stable displacement.

***Capillary fingering*:** In the regime of capillary fingering (bottom in Fig. 2.3), the injected non-wetting fluid invaded not only along the outlet direction but also to radial direction and even inlet direction. The flow paths merged to a main stout finger; hence, the invading phase saturation was much higher. At low Ca, the viscous forces are negligible in both defending and invading fluid and the principal force is due to capillarity. The invasion process of capillary fingering can be described with the invasion percolation theory (Dias and Wilkinson, 1986). The invading fluid only passed through the largest throat where the capillary entry pressure was the lowest. Thus, the average throat size invaded by the invading phase for capillary fingering was much larger than that for viscous fingering. It also contributed the higher invading phase saturation for capillary fingering.

***Stable displacement*:** In the regime of stable displacement (upper-right in Fig. 2.3), the defending phase was almost completely displaced by the invading phase, and only near outlet presented some irregularities. At high *Ca* and high *M*, the principal force is due to the viscosity of the invading fluid. The stable displacement occurs at the unfavorable condition ($\mathrm{Log}M > 0$), where the lower viscosity defending fluid is displaced by a higher viscosity fluid. During the invasion process of invading phase, some unstable fingers occurred at the main flow front. These fingers would be overtaken by the followed main flow, since the fingers have a lower pressure than the main flow front (Zhang et al., 2011). Therefore, the stable displacement with compact structure usually has a very high saturation (e.g., 94% at $\mathrm{Log}Ca = -2$, $\mathrm{Log}M = 2$).

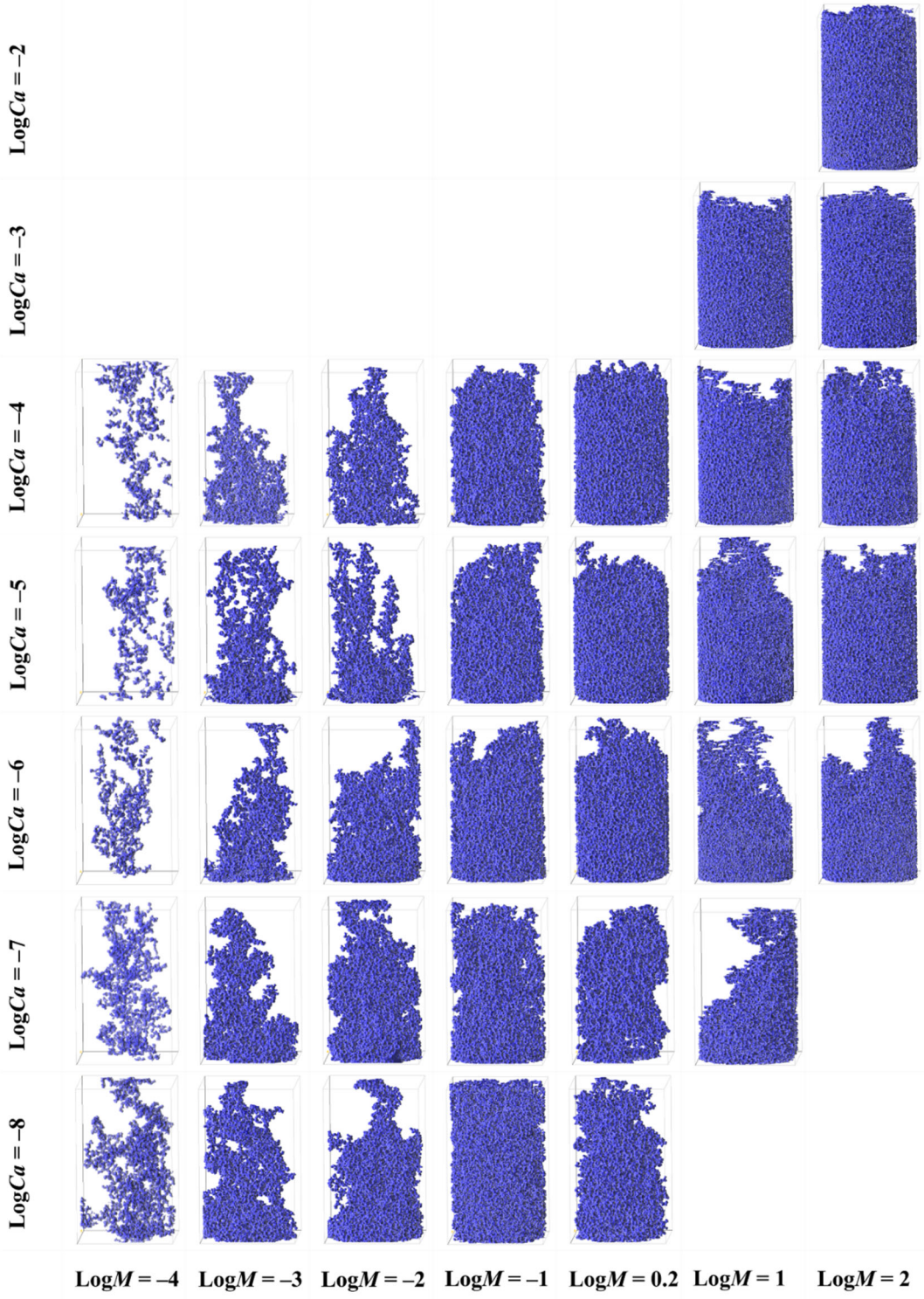

Figure 2.3. Visualization of the 3D fluid–fluid displacement morphologies at the breakthrough time under a wide range of viscosity ratio Log*M* and capillary number Log*Ca*.

2.3.2 Dynamic displacement patterns

Fig. 2.4 presents the growth behavior of the invading phase (Log$M$ = −3) to gain an insight into how the competition between the capillary and viscous forces affects the invasion dynamic. The displacement pattern at V/V_{br} =1.00 represents the breakthrough time when the invading phase first reached the top of the porous media. The displacement patterns indicate typical viscous and capillary fingering, respectively. The invading phase invasion processes are mainly controlled by the viscous force for viscous fingering (Fig. 2.4(a)). Before the breakthrough, thin figures with 1–2 pore bodies followed a number of preferential flow paths along the injection direction (Ferer et al., 2004; Tsuji et al., 2016). The invading phase rapidly grew at the front position, while the bulk of the invading fluid at the near inlet area grew forward with a relatively lower speed. After the main flow reached to the outlet of the porous medium, its structure remained stable, and other fingers at the front of the bulk fluid shown an accelerate growth. As shown in Figure 10a, the saturation of invading phase increased rapidly at the front than that at the bottom after breakthrough.

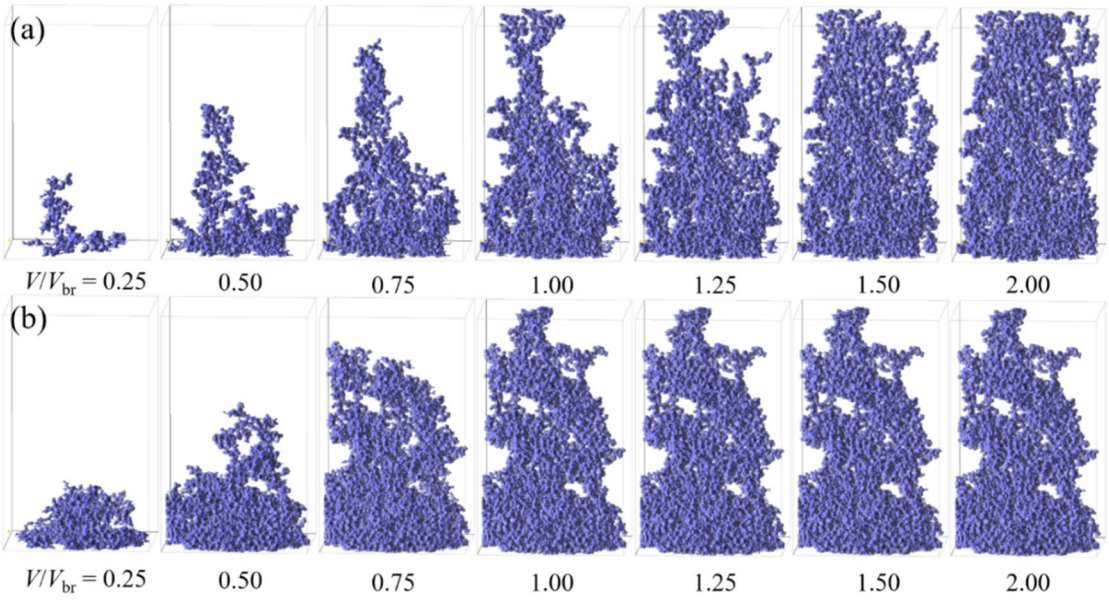

Figure 2.4. Invasion dynamic of the invading phase before and after the breakthrough time under the experimentad conditions of (a) Log$M$ = −3, LogCa = −4 viscous fingering, and (b) LogCa = −8 capillary fingering.

Decreasing four orders of magnitude of the capillary number to $Ca = 1.0 \times 10^{-8}$, the capillary forces overpassed the viscous forces, and controlled the invasion dynamic in drainage process. The iconic backward structure of the invading phase and the defending phase trapping occurred during the whole invasion process. Before the breakthrough time ($V/V_{br} < 1.0$), the main finger front was not strictly growing along the injection direction (Fig. 2.4(b)). A lot of invasion processes were also observed at the bulk fluid (bottom region). Once the invading phase reached the outlet, continue to inject, no new fingers could be observed either at the front or at the bottom. As shown in Fig.2.5(b), the invading phase saturation profiles almost fixed after breakthrough ($V/V_{br} > 1.0$), except slightly different at the bottom compared with that at breakthrough time ($V/V_{br} = 1.0$). For the capillary fingering, the imposed pressure was not sufficient to invade new throats and pores after breakthrough. Therefore, the fluid could only flow through the formed displacement pathways, and the invading phase saturation remained constant. It indicated that the displacement efficiency cannot be further improved by injecting excessive volume of invading phase for capillary fingering conditions.

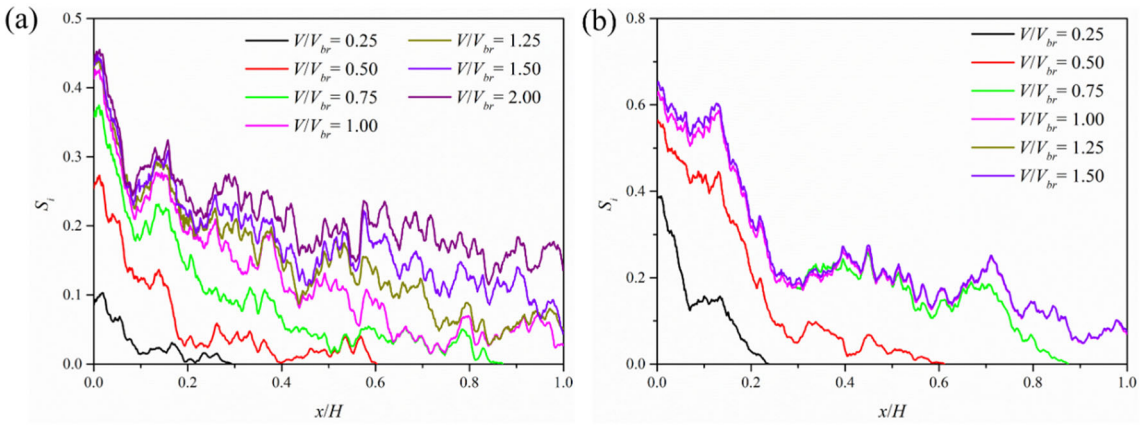

Figure 2.5. Saturation distribution of the invading phase along the flow direction during the injection under the experimentl conditions of (a) Log$M$ = −3, LogCa = −4 viscous fingering, and (b) LogCa = −8 capillary fingering. x/H is the dimensionless distance, where x the distance from inlet part, H is the height of the porous media, respectively.

Fig. 2.6 shows that the displacement efficiency at the breakthrough time increased with the decreasing the injection flow rate, thereby agreeing with the previous numerical results (Lenormand et al., 1988; Tsuji et al., 2016). However, a reverse trend could be found at the equilibrium state (Zhang et al., 2011). The invasion dynamics of the invading phase provides an explanation as to this phenomenon. After the breakthrough time, the invading phase

saturation continued to linearly increase with the injection volume for the high capillary number cases (Fig. 2.6 (a–b)). Meanwhile, no further increase was observed at the low-flow rate condition (Fig. 2.6(e)). Thus, S_i of the viscous fingering will be larger than that of the capillary fingering at the same viscosity ratio when the displacement pattern achieves an equilibrium state.

The difference between ΔS_i^{br} at the breakthrough time and S_i^{eq} at the equilibrium state was measured to classify the displacement patterns (i.e., $\Delta S_i = S_i^{eq} - S_i^{br}$). Fig. 2.6 illustrates that the ΔS_i value is larger than 13% for the viscous fingering but is almost equal to zero for the capillary fingering. At the transition zone, the invading phase saturation linearly increased with the injection volume after the breakthrough, and then trended to a constant value (Fig. 2.6(c−d)). Subsequently, ΔS_i roughly increased with the increasing of capillary number, which can also be found in rough fracture and natural sandstone (Bakhshian et al., 2019; Chen et al., 2018).

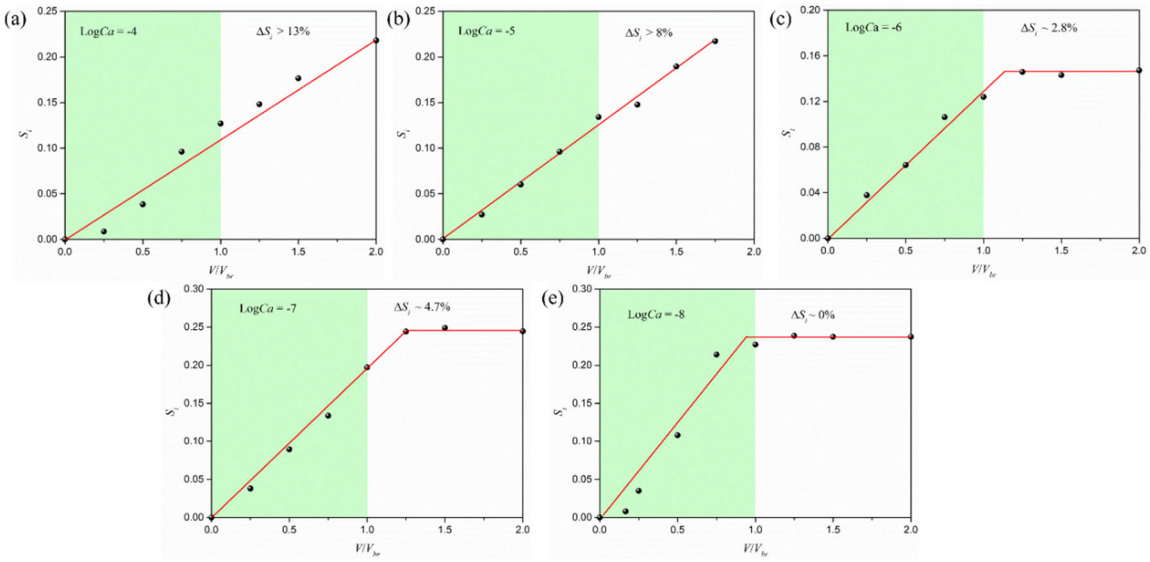

Figure 2.6. Saturation of the invading phase as a function of the injection volume V/V_{br}. The green shadow represents that before the breakthrough time. ΔS_i equals to the difference between S_i^{br} at the breakthrough time and S_i^{eq} at the equilibrium state.

2.4 Characterization of fingering structures at breakthrough

2.4.1 Saturation of non-wetting phase

Fig. 2.7(a) shows the saturation distribution of the invading phase on the diagram of *Ca* and *M*. Generally, the invading phase saturation at breakthrough time increase from viscous fingering to capillary fingering, then to stable displacement. To quantify the boundaries of the three regimes in *Ca*–*M* diagram, we estimated the effect of the three displacement patterns on the saturation at breakthrough time.

Fig. 2.7(b) shows the effect of the viscosity ratio on the invading phase saturation, which can be used to distinguish the boundaries from viscous fingering to stable displacement (Lines A and B, Fig. 2.11). The saturation curve as a function of the viscosity ratio consisting of two plateaus and a sharply growing middle segment qualitatively agrees with the simulation result proposed by Lenormand et al., (1988). The two plateaus represent two distinct regimes, the viscous fingering with low saturation and close stable displacement with high saturation, respectively. An increasing stage with a constant slope occurred from Log$M$ = −2 to 0.2 for high *Ca* condition (i.e., LogCa = −4 and −5), indicating a transition zone from viscous fingering to close stable displacement (Lines A and B, Fig. 2.11).

Fig. 2.7(c) and d depict the effect of the capillary number on the invading phase saturation for unfavorable (Log$M$ < 0) and favorable displacements (Log$M$ > 0), respectively. The invading phase saturation generally decreased with the increasing capillary number for the unfavorable displacement, reflecting a transition zone from viscous fingering to capillary fingering; but increased for the favorable displacement, reflecting a transition zone from capillary fingering to stable displacement. As shown green dot line in Fig. 2.7(c), at Log$M$ = 2, the curve consists of two plateaus and a descending segment. The two plateaus represent two distinct regimes, the capillary fingering with high saturation and viscous fingering with low saturation, respectively. A decreasing stage with a constant slope occurred from LogCa = −7 to −5, indicating a transition zone from capillary fingering to viscous fingering (Lines E and F, Fig. 2.11). For the two lowest *M* (i.e., Log$M$ = −3 and −4), only one plateau with low saturation exists at high *Ca* condition, which represents the viscous fingering regime. However, the capillary number of decrement stage remains in two orders of magnitude. It indicates that the width of transition zone from viscous fingering to capillary fingering is stable with different

M. For the highest *M* (i.e., Log*M* = −1), the invading phase saturation changes slightly from Log*Ca* = −8 to −6, indicating a capillary fingering regime (Line D, Fig. 2.11).

As shown in Fig. 2.7(d), the invading phase saturation increases with the capillary number under favorable displacement. At low *Ca* (i.e., Log *Ca* = −8 and −7), the invading phase saturation in all three experimental conditions remains almost constant, about 40%. With the increasing of the capillary number, the role of viscous forces of displacing fluid become more important. Therefore, the invading phase saturation increases with the increasing of capillary from Log*Ca* = −7 to −3, which is referred as a transition zone from capillary fingering to stable displacement (Lines D and C, Figure 5). At high *Ca* (i.e., Log*Ca* = −3 and −2), the invading phase saturation is close to 90%, suggesting that stable displacements have taken place and only near outlet exists some irregularities.

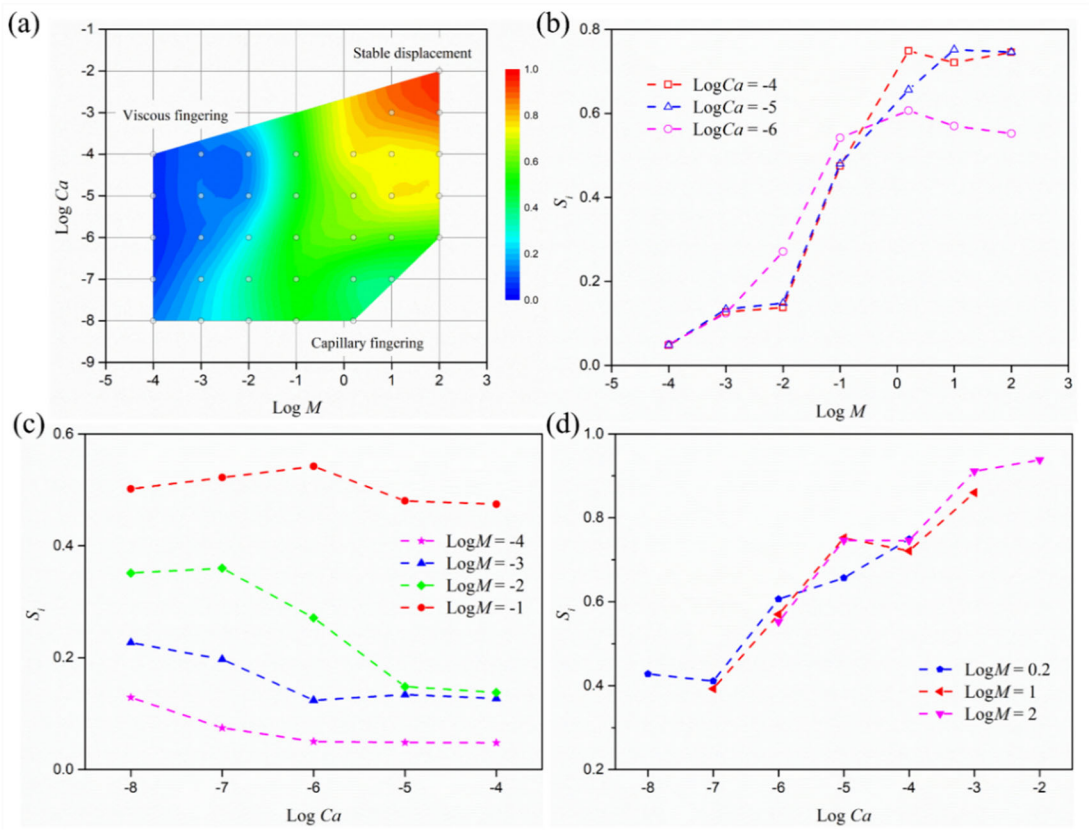

Figure 2.7. Saturation of the invading phase at the breakthrough time for the drainage experiments in the 3D porous media. (a) Saturation contour mapping. (b) S_i variations of as a function of Log*M*. (c) S_i variations as a function of Log*Ca* for the unfavorable displacement Log*M* < 0. (d) S_i variations as a function of Log*Ca* for the favorable displacement Log*M* > 0.

2.4.2 Fractal dimension

The observation in Fig. 2.3 shows that the finger structure exhibits complex spatial distribution for three typical displacement patterns. To estimate the complexity of finger structures, the fractal dimension was introduced using the standard box counting method. The 3D structure of invading phase was separated into some several parts based on the size of the box s. Every box was then checked whether it contained the displacing fluid or not. The data of the number of boxes that contained the displacing fluid $N(s)$ and the length of boxes $1/s$ were used to calculate the fractal dimension. As shown in Fig 2.8 (a), the estimate slop of ln $N(s)$–ln $1/s$ is the fractal dimension value.

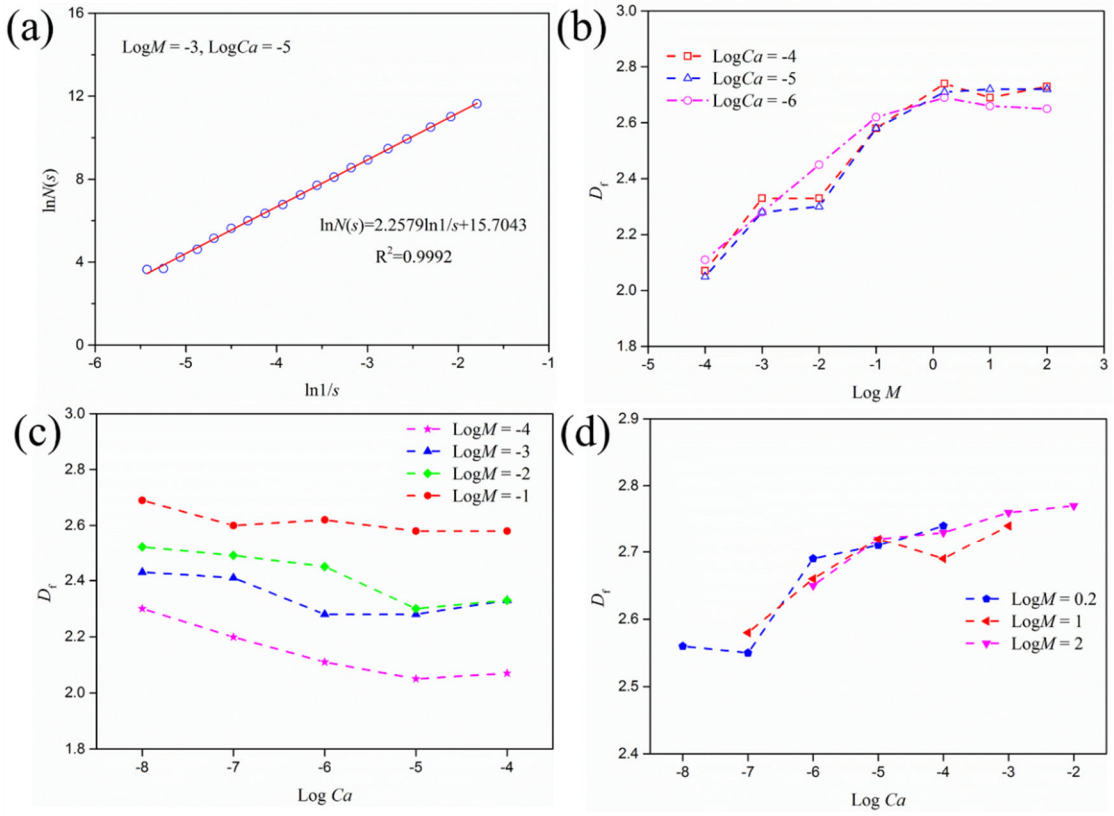

Figure 2.8. Fractal dimension (D_f) of the invading phase at the breakthrough time for the drainage experiments in the 3D porous media. (a) Box counting method to obtain the fractal dimension. (b) D_f variations as a function of Log$M$. (c) D_f variations as a function of LogCa for the unfavorable displacement Log$M$ < 0. (d) D_f variations as a function of LogCa for the favorable displacement Log$M$ > 0.

Fig. 2.8(b–d) depict the effects of the capillary number and the viscosity ratio on the fractal number of the invading phase, including the favorable and unfavorable displacements. The curves of fractal dimension as a function of *Ca* and *M* show a similar tendency with curves of invading phase saturation. The fractal dimension increases from viscous fingering to capillary fingering, and a transition zone exists between them. Six cases were selected as the typical capillary fingering inside of the capillary fingering regime in Fig. 2.11. The average fractal dimensions for the six typical capillary fingerings equaled 2.58 ± 0.05. The value was in a reasonable agreement with the value of 2.55 in the simulation results when invasion percolation theory was considered (Dias and Wilkinson, 1986). For the lowest viscosity ratio (Log$M$ = −4), the fractal dimensions of the 3D viscous fingering structures, which were very close to 2.00, were 2.05 and 2.07 for the capillary numbers of LogCa = −4 and LogCa = −5. In the extreme condition, lower M and higher Ca, the viscous fingering structures could be looser and corresponding lower fractal dimension. The limitation of fractal dimension predicted by the diffusion limited cluster aggregation (DLCA) was 1.80 (Eggersdorfer et al., 2011; Mandelbrot, 1983). The pores filled by the invading phase was treated as the clusters in the DLCA method.

2.4.3 Finger width

A more relevant distinguishing feature for different displacement patterns (e.g., viscous fingering and capillary fingering) is the finger width (Løvoll et al., 2004; Stokes et al., 1986). When viscous fingering occurs, loosely connected or disconnected flow paths progress forward toward the outlet. It is very difficult to directly measure the width of a three-dimensional finger due to its complex spatial structure. Here, we presented a statistical averaging method to estimate the finger width of these 3D fingerings. Firstly, the fingering structure was divided into several parts (n) along the vertical direction, as shown inset in Fig. 2.9 (n = 4) . Then the 3D object count method was applied to detect all unconnected objects, which was treated as the cross-sectional of a finger. The information of these objects, including volume V, height h and numbering j, was stored in a matrix. Each object was assumed as a cylinder of diameter d, and the value of d could be calculated by $d_j = (4/\pi \cdot V_j/h_j)^{1/2}$. After, a volume-weighted average was used to estimate the average diameter, $\bar{d} = \sum V_j d_j / \sum V_j$. Finally, the average diameter divided by the pore diameter d_{pore} to get the dimensionless finger width $\bar{w}$.

Fig. 2.9 shows two different trends of $\bar{w}$ as a function of n for the viscous fingering (Log$M$ = −3, LogCa = −5) and capillary fingering (Log$M$ = −3, LogCa = −7). For viscous fingering, the average finger width is uniform and equals to the single flow path width. With the increasing of n, the average width does not change, and each object has a same finger width. For capillary fingering, the average finger width decreases sharply (n < 20) and then tends to be constant. At low n, the average finger width is overestimated due the interconnected flow path. The height of each part decreases with the increasing of n. When the height is smaller than the size of trapped blobs, single flow path without trapped blobs start to be detected. The average width of these single flow path is selected to evaluate the finger width of capillary fingering. The effective finger width $\bar{\bar{w}}$ for each displacement pattern was defined by further averaging the average finger width $\bar{\bar{w}}$ between n = 20 and 30 (Trojer et al., 2015).

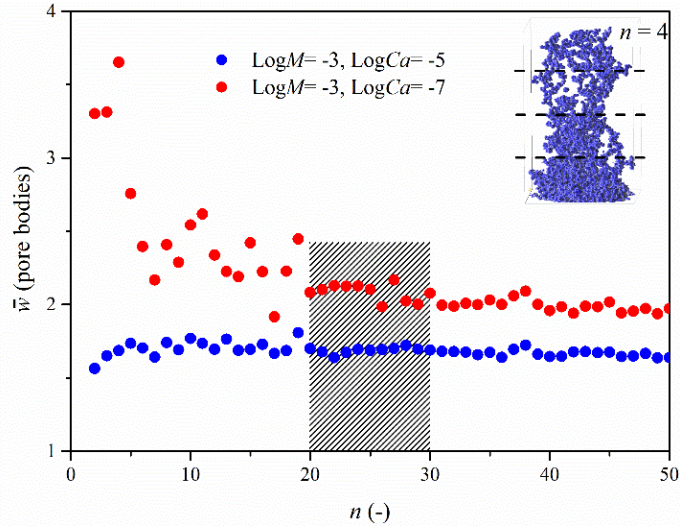

Figure 2.9. Average finger width $\bar{w}$ as a function of the number of parts for Log$M$= −3, LogCa = −5 and −7.

Fig. 2.10 presents the effective finger width $\bar{\bar{w}}$ as a function of capillary number and viscosity ratio. As shown in Fig. 2.10(a), with the increasing of capillary number, the effective finger width slightly decreases from 2 to 1.75 at Log$M$ = −3. Although a transition from capillary fingering to capillary fingering is expected, the effective finger width remains at a small value under all condition. The capillary fingering still presents some features of viscous fingering under low M condition. At a fixed capillary number LogCa = −6, the effective finger width changes significantly with capillary number, increasing from 2 to 7. It indicates the displacement patterns changes from viscous fingering to capillary fingering, which

qualitatively agrees the prediction of phase diagram. Generally, the effective finger of viscous fingering is 1–2 pore bodies, while capillary fingering is 6–7 pore bodies.

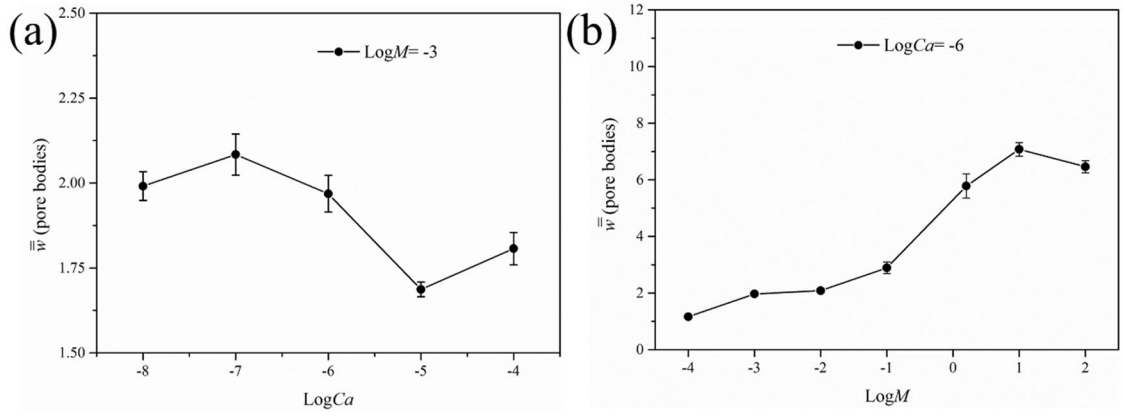

Figure 2.10. Effective finger width $\overline{\overline{w}}$ as a function of (a) LogCa and (b) Log$M$. The error bars represent the standard deviation of the measured results with different n.

2.5 Phase diagram for 3D porous media

The boundaries of the three displacement regimes on the phase diagram for 3D unconsolidated porous media were determined based on the 35 experimental results, as shown in Fig. 2.11. The shape of the three regimes was similar with the result obtain in the 2D periodic homogenous pore model (Lenormand et al., 1988; Zhang et al., 2011). Two parallel lines with slop = 1 represent the boundaries of transition zone from viscous fingering to capillary fingering. This indicates the displacement process in 3D porous media is also controlled by the competition between viscous forces and capillary forces (Lenormand et al., 1988). However, the locations of these boundaries are different from the 2D micromodel experiment results (Zhang et al., 2011). A broader transition zone between any two regimes could be found in 3D heterogeneous porous media. The primary contribution to this different is the inherent pore heterogeneity. As shown in Figure 1b, the pore and throat size distributions in 3D porous media show a very wide range, where the multiple displacement patterns easy occurred simultaneously (Chen et al., 2017; Liu et al., 2015). The system dimension affects the inherent connectivity of porous media. The coordination number of pores is 4 and 4.6 for the 2D homogenous micromodel (Zhang et al., 2011) and the 3D packed bed, respectively. In highly connected porous media, the fingers easily merge with adjacent fingers and show a multiple

displacement pattern. As shown in Fig. 2.3, even for viscous fingering, the thin finger is connected with neighboring one at some pores.

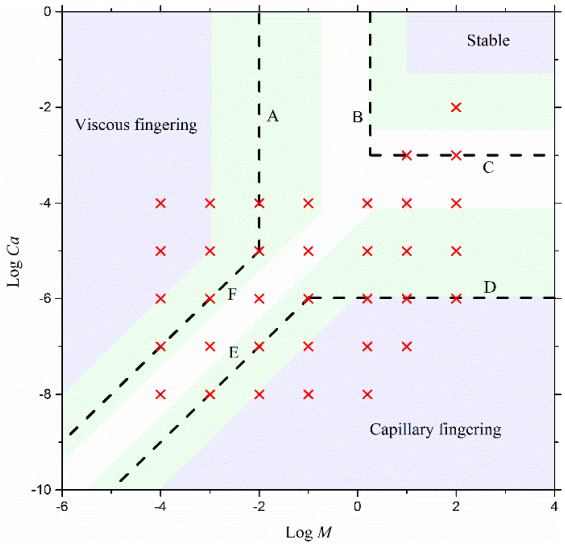

Figure 2.11. Phase diagram of the fluid–fluid displacement morphologies for the drainage experiments in the 3D porous media (dash lines). The 35 red crosses indicate the experimental conditions. The 2D results proposed in the previous studies of Lenormand et al. (1988) (light purple background) and Zhang et al. (2011) (light green background) have defined the boundaries of the displacement patterns according to the simulation and experiment in the micromodels.

2.6 Summary

The fluid–fluid immiscible displacement in the 3D porous media was experimentally studied herein using micro-CT. An unconsolidated packed bed with glass beads was chosen as the porous media. Seven fluid pairs were selected as the defending and invading phases to provide a wide range of viscosity ratio ranging from Log$M$ = −4 to 2, including favorable and unfavorable displacements. The invading phase was injected to displace the initial saturated defending phase under different flow rates, and the capillary number ranged from LogCa = −8 to −2. The displacement patterns at the breakthrough time and the invasion dynamic during the drainage process were visualized. The main findings in this study include:

All 35 displacement patterns obtained at breakthrough time were mapped on a Ca–M diagram, including unfavorable (Log$M$ < 0) and favorable displacement (Log$M$ > 0). Three typical displacement patterns, namely viscous fingering, capillary fingering and stable displacement, were observed in 3D porous media. The rough location of three displacement patterns was consistent with previous studies in 2D micromodel. Viscous fingering was observed at high

Ca and low *M*, and capillary fingering occurred at low *Ca* condition. The compact displacement is referred as stable displacement at high *Ca* and high *M* condition.

The corresponding saturation distribution for the different patterns was also mapped on a *Ca*–*M* diagram. With the increasing of capillary number, the saturation of the invading phase decreases for unfavorable displacement and increases for favorable displacement. Based on the quantitative analyses of the saturation distribution as a function of *Ca* and *M*, the boundaries for three regimes, namely viscous fingering, capillary fingering and stable displacement, were determined. We then for the first time proposed a phase diagram for 3D porous media describing the displacement patterns as a capillary number and viscosity ratio. Compared to Zhang et al.'s result in 2D micromodel (Zhang et al., 2011), a broader transition zone between the viscous fingering, capillary fingering and stable displacement was found in 3D porous media.

The characterization of finger structures (e.g., fractal dimension and finger width) were to reveal the mechanism of how the displacing fluid invades the pores and throats inside porous media for different displacement patterns. The average fractal dimension of capillary fingering is 2.58 ± 0.05, which is in reasonable agreement with 2.55 defined by the invasion percolation (IP) theory. This indicates that IP can be used to describe the invasion process of capillary fingering in 3D porous media. The finger width increases from viscous fingering (1–2 pore bodies) to capillary fingering (6–7 pore bodies), reflecting that the invasion process is more controlled by capillary forces than viscous forces.

The invasion dynamic during the drainage process from a pore scale view was illuminated for typical viscous and capillary fingering. Under continues injection condition, the saturation of invading phase continues to increase after breakthrough for viscous fingering but remains stable for capillary fingering. The experimental observation clarifies that new pores and throats would be invaded by the followed flow and formed several flow paths for viscous fingering. At low *Ca*, capillary fingering, the subsequent fluid would only flow along the previous flow path once the breakthrough occurred.

The results described in this chapter have been published as: **Y. Hu***, A. Patmonoaji, C. Zhang, T. Suekane, Experimental study on the displacement patterns and the phase diagram of immiscible fluid displacement in three-dimensional porous media, *Adv. Water Resour.* 140 (2020) 103584.

Chapter 3. Effect of capillary number on morphological characterizations of trapped phase in 3D porous media

In this chapter, we studied the capillary desaturation curves at a wide range of capillary number *Ca* from a pore-scale perspective.

3.1 Introduction

A few studies have examined the capillary desaturation curve from a pore-scale perspective in porous media. According to the injection strategies, the desaturation curves can be divided into two different categories according to the strategies to increase capillary number. In the first category, the gas/oil phase is displaced by the flooding water at a low flow rate; after reaching a steady state, the flow rate is progressively increased (Armstrong et al., 2014; Datta et al., 2014; Oughanem et al., 2015). In the second category, a series of drainage-imbibition cycles was performed, and the imbibition flow rate is independently increased (Georgiadis et al., 2013; Herring et al., 2013; Khishvand et al., 2016; Krummel et al., 2013). The desaturation curves show the same shape for both two categories, where the residual saturation remains constant and then almost linearly decreases as the capillary number increases. Datta et al. (Datta et al., 2014) used confocal microscopy to directly visualize the formation and complex morphologies of trapped non-wetting phase in a sintered glass beads packed bed. They found that at $Ca > 2 \times 10^{-4}$, the largest ganglia were increasingly mobilized and flushed out of the porous media. With the increase of *Ca*, the maximal length of the ganglia decreased in a similar manner to the calculated value, which was analyzed by the balance between the viscous and capillary forces exerted on the ganglia. Georgiadis et al. (Georgiadis et al., 2013) investigated the development of oil clusters in a sintered glass beads porous media using micro-CT. At low *Ca*, the size distribution of trapped oil clusters showed a power-law distribution with $\tau = 2.10$, which is in good agreement with other studies (Geistlinger and Mohammadian, 2015; Iglauer et al., 2013). Although the effect of capillary number on residual saturation has been studied, the effect on cluster size distribution has not been considered. Khishvand et al. (Khishvand et al., 2016) performed drainage-imbibition cycle experiments in sandstone and carbonate rocks with capillary numbers ranging from 1.2×10^{-6} to 1.6×10^{-4}. They found that as the capillary

number increased, the imbibition produced smaller trapped oil blobs, resulting in the reduction of residual saturation.

In previous research, residual saturation and cluster size distribution are the two main parameters considered. There are several questions that remain unanswered: what is the difference between the two capillary desaturation curves using different injection strategies? Whether the power-law behavior still exist during dynamic flow regime? In addition, no attempt has been made to investigate the impact of high flow rate on the interfacial area. How does the flow rate affect the ratio of the gas-liquid interfacial area and the total surface area? The gas–liquid interfacial area (meniscus interphase) is believed to be the main factor affecting mass transfer (Geistlinger et al., 2005; Johns and Gladden, 1999; Zhang et al., 2002). The dissolution process through the meniscus interphase not only affects dissolution trapping but also mineral trapping, which is important in the long-term safety of CCS.

3.2 Materials

3.2.1 Porous media

Artificial plastic particles (PP) were selected to represent highly angular particles such as naturally occurring mica minerals and biogenic sands. Various ranges of particle size and uniformity based on the Standard American Society for Testing and Materials (ASTM) were used. Table 3.1 lists the physical properties of these porous media, including the particle size, porosity (ε), and permeability (k_a). More detailed information on the pore/particle size distributions of the different porous media can be found in our previous work (Patmonoaji et al., 2018). These particles were poured into an acrylic column with a 10-mm inner diameter, producing the packing as an unconsolidated porous medium. During preparation of the core sample, the column was continuously shaken to produce as compact a packed bed as possible. For each experiment, the length of the core sample was fixed at around 30 ± 1 mm, which was almost two times longer than the field of view (FOV). To form a uniform incoming flow field, a low permeability sintered glass filter with a thickness of 1 mm was added at the inlet. At the top of the column, a low permeability filter may cause structural trapping. A reservoir was formed with two fine metal meshes and large glass beads to eliminate the outlet effects.

Table 3.1. Physical properties of particles and porous media

Type	Size range (μm)	d_{50}[1] (μm)	G[2] (-)	ε(X-ray)[3] (%)	$d_{p.median}$[4] (μm)	k_a(Cal.)[5] (m^2)	a_p[6] (mm^{-1})
	355-425	390	0.70	0.46	169	3.0×10^{-10}	14.23
	500-600	555	0.68	0.47	340	6.2×10^{-10}	12.75
	600-710	655	0.68	0.47	446	8.7×10^{-10}	12.20
	355-710	533	0.68	0.46	364	5.3×10^{-10}	13.61

[1] d_{50}: median particle diameter;
[2] G: sphericity index of particle;
[3] ε: porosity estimated using micro-CT images;
[4] $d_{p.median}$: median pore diameter;
[5] k_a: absolute permeability calculated by Kozeny–Carman relation, $k_a = \frac{\Psi^2 d_{50}^2}{180} \frac{\varepsilon^2}{(1-\varepsilon)^2}$;
[6] a_p: specific interfacial areas of particles, -: not measured.

3.2.2 Fluid pairs

The gas/water system was used in this study to investigate the capillary trapping in the porous media. High-purity nitrogen gas (99%) and deionized water were used as the trapped phase and mobile phase, respectively. Nitrogen was selected for the gas phase owing to its low solubility and high safety. To obtain a distinguishable contrast between the phases during X-ray scanning, water was doped with 7.5wt% sodium iodine. Previous research has shown that doping at such concentrations has a negligible influence on the fluid properties and capillary trapping processes (Brusseau et al., 2009). All experiments were conducted at ambient temperature (293 K) and pressure (0.1 MPa). The dynamic viscosities of nitrogen and water are $\mu_{nw} = 0.018$ mPa.s and $\mu_w = 1.05$ mPa.s, respectively, resulting in a viscosity ratio Log$M$ = −1.77. The densities of nitrogen and water are ρ_{nw} = 1.204 kg/m^3 and ρ_w = 1005 kg/m^3, respectively. The interfacial tension between the phases was 70.13 mN/m, as measured using the drop pendent method (Kruss, DAS255).

3.3 Analysis methods

3.3.1 Experimental procedures

Fig. 3.1 shows the experimental system, including the visualization section, porous media and fluid flow section. The core sample was fixed vertically on the central stage inside the micro-CT scanner. At the inlet and outlet, 1/8-inch PEEK tube was connected to inject gas and water.

The volume and flow rate of water and CO_2 were controlled by three syringe pumps (KDS-200, KD Scientific Inc.). A gas tank with a regulator was used to inject the nitrogen gas. During CT scanning, a dynamic model was applied in which the sample remained fixed while the X-ray sources and detector rotated horizontally. This model eliminated the effects of rotation on the sample position and fluid redistribution inside the porous media.

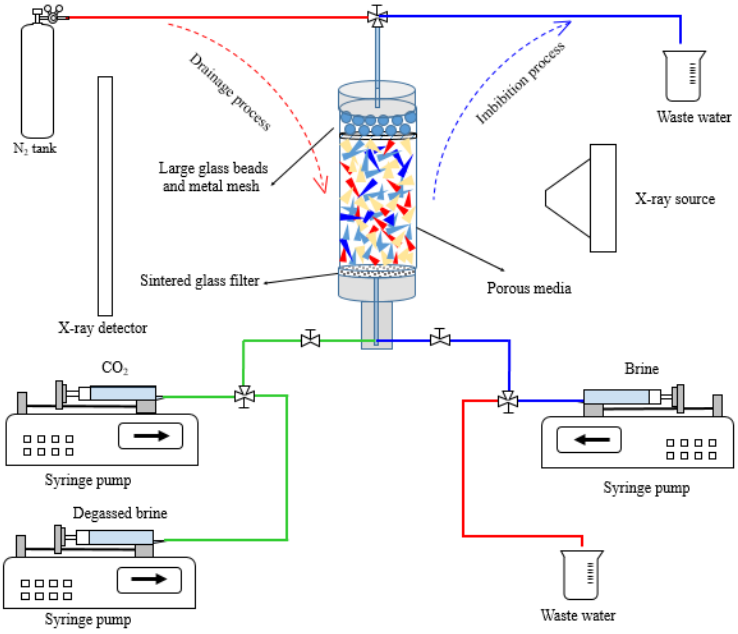

Figure 3.1. Schematic of experimental setup.

The experiments were performed using the following procedures:

1. Dry CO_2 was injected at a high flow rate of 5 mL/min into the packing to replace the air.
2. A dry scan was taken to obtain the pore structure of the porous media, which was used as a reference for further image processing.
3. More than 30 pore volumes (PV) of degassed water were injected at 20 mL/min. Most of the gas was flushed out from the porous media. Residual CO_2 can be quickly dissolved in degassed water owing its high solubility. This approach ensures that the pore space was fully saturated with water before the drainage process.
4. Water was injected at 2 mL/min to remove any degassed water from the porous media.
5. The drainage process was then performed by injecting (downward) N_2 at 0.1 MPa to displace water inside the porous media.
6. A scan was taken to obtain the initial saturation of the gas after the first drainage. After the high pressure N_2 injection, a high initial saturation was reached, i.e., about 90%.

7. The imbibition process was performed by pumping (upward) 3 PV of water to capture gas bubbles.
8. After injection, a scan was taken to obtain the distribution of the trapped gas bubbles.
9. Steps 5–8 were repeated. In order to investigate the influence of imbibition capillary number on capillary trapping, the water injection flow rate in Step 7 was increased from 21 μL/min to 80,000 μL/min, corresponding to capillary numbers from 1.0×10^{-7} to 3.8×10^{-4}.

The above experimental procedures were repeated for all six porous media. Since the solubility of N_2 in water is relatively low, the effect of gas dissolution on the residual gas saturation can be ignored in high permeability unconsolidated porous media (Suekane et al., 2010). The effect of buoyancy force on the capillary trapping was estimated by the Bond number, as follows:

$$Bo = \frac{\Delta\rho g d_{50}^2}{\sigma} \tag{3-1}$$

where $\Delta\rho$ is density difference, g is gravity, and σ is interfacial tension. In this study, the Bone number ranged from 8.35×10^{-3} to 9.32×10^{-2}. This value is lower than 0.35, at which Morrow and Songkran (Morrow and Songkran, 1982) reported that no trapping occurs.

3.3.2 Image processing

A high-resolution X-ray micro-tomography scanner (Comscantechno Co. ScanXmate-RB090SS) was used to capture the three-dimensional topology of trapped phase. The sample was placed midway between the X-ray source and the detector. During the scanning, the X-ray source and detector rotated 360° horizontally within 125 s. The images obtained from the detector were 992 × 992 pixels with a resolution of 16.47 μm/pixel. In all cases, the scanning was conducted at 70 kV and 116 μA. More detailed information on the CT settings can be found in our previous work (Hu et al., 2020a).

The raw images were filtered to remove noise and preserve the edges using a non-local means filter (Andrew et al., 2014). By comparing Figs. 1a and b, it is clear that the filtering improves the signal to noise ratio significantly while keeping the phase boundaries preserved. The filtered image of dry scan was then segmented into grains and pore structures using Otsu's algorithm in ImageJ software (NIH). For the wet scan images, although the agent was doped

into water, it was still very difficult to separate the three phases. As shown in Fig. S4, the histogram showed that the gray value of gas phase was markedly lower than did the water and grain. A global threshold value was employed based on the histogram, and only gas phase was obtained. Next, the three phases, i.e., grain, gas, and water, were combined (Fig. 3.2(g)). The segmented image was then analyzed in 3D. Firstly, the 3D Object Counter plugin in ImageJ was used to label disconnected bubbles. The MorphoLibJ plugin was then applied to measure the volume and interfacial area of each bubble. During the image processing, some small voxels were falsely labeled as bubbles. The small size bubble can also cause significant error on the volume and interfacial area measurement. Therefore, bubbles smaller than 50 voxels were removed as noise. It is worth noting that this approach removed less than 2% of volume.

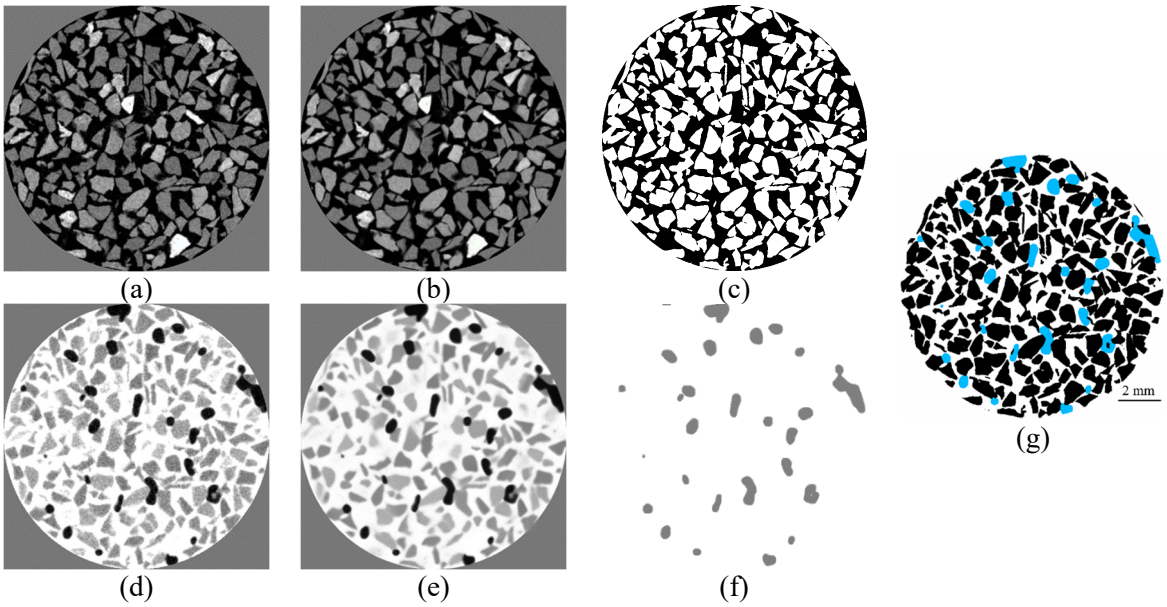

Figure 3.2. Two-dimensional cross-sectional images of (a–c) the dry and (d–f) wet scans; (a, d) raw images; (b, e) images filtered with non-local means filter; (c, f) images after threshold; (g) combination image.

3.3.3 Extraction of interfacial area

The surface of an individual bubble includes two components, i.e., gas–solid and gas–water interfacial areas. Fig. 3.3 depicts the estimation method for extracting the distribution of the two kinds of interfacial area. Firstly, the binary image of the bubble was dilated by one pixel. Then, the original bubble image was subtracted from the dilated image to obtain the total

interfacial area. The dilated image was also used to make a Boolean "AND" operation with the solid image. The overlap region was taken as the interfacial area between the gas and solid phases. Finally, the gas–water interfacial area was obtained by subtracting the gas–solid interfacial area from the total gas surface area. In Fig. 3.3(f), the distribution of gas–water (black) and gas–solid (green) interfacial areas are shown.

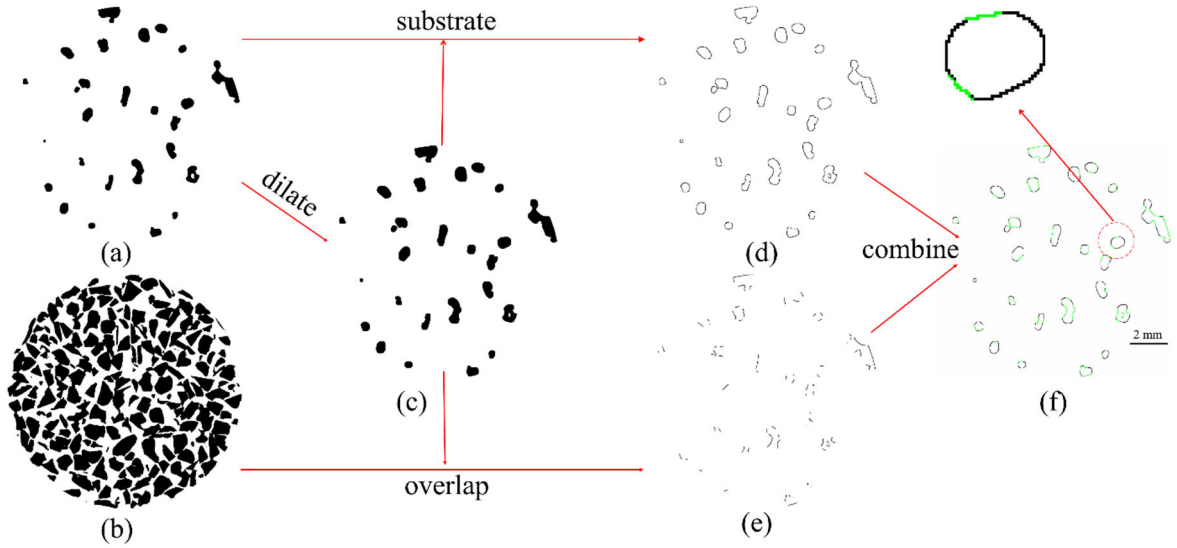

Figure 3.3. Schematic of gas–water interfacial area extraction in porous media. (a) Binary images of bubble and (b) solid; (c) image of bubble after one pixel dilate; (d) total gas surface area; (e) gas–solid interfacial area; (f) distribution of gas-water (black) and gas–solid (green) interfacial areas.

3.3.4 Euler number

Two parameters, namely sphericity index and Euler number, were applied to classify the residual gas patterns inside the porous media. The sphericity index (G) describes how closely a trapped bubble resembles a perfect sphere. It can be calculated as follows:

$$G = \frac{\pi^{1/3}(6V)^{2/3}}{A}, \tag{3-2}$$

where V and A are the volume and surface area of the trapped bubble, respectively.

The Euler number (χ) is a topological invariant used to estimate the connectivity of a trapped bubble (Herring et al., 2013). For a 3D object, the Euler number can be expressed as follows:

$$\chi = \beta_0 - \beta_1 + \beta_2, \tag{3-3}$$

where β_0 is the zeroth Betti number, referring to the number of distinct elements of the bubble; β_1 is the first Betti number, which refers to the number of tunnels; and β_2 is the second Betti number, indicating the number of enclosed voids. In this study, an individual bubble was estimated with the Euler number; therefore, the zeroth Betti number was one ($\beta_0 \equiv 1$). Inside porous media, there are no individual particles without connection to other particles. In addition, a gas bubble cannot surround a particle to form an enclosed void, i.e., $\beta_2 \equiv 0$. Therefore, the Euler number of an individual bubble can be simply assumed as:

$$\chi = 1 - \beta_1. \tag{3-4}$$

Based on the above-mentioned topology of the trapped bubbles, the bubbles were classified into three patterns, i.e., singlet, ganglia, or cluster (Fig. 3.4). Singlet is usually trapped in a single pore and has the smallest volume. The singlet pattern presents a smooth sphere with a high G, whereas the ganglia pattern shows a dimpled surface depending on the sharp of grain. The ganglia pattern exhibits long spans several pores and throats. The sphericity index decreases with an increasing number of pores occupied by ganglia. The Euler number of ganglia and singlet is fixed, $\chi = 1$. As shown in Fig. 3.4, the simplest ganglia only spanned two adjacent pores with a sphericity index of 0.4. We defined $G = 0.4$ as the threshold value from singlet to ganglia. Compared with ganglia, a significant difference of cluster pattern is that they usually exist one or more loops. This feature of cluster is mainly reflected in their smaller Euler numbers ($\chi \leq 0$). In addition, the cluster has a lowest sphericity index owing to its large surface area. The sphericity of the longest single chain ganglia ($G \sim 0.1$) was the threshold value from ganglia to cluster.

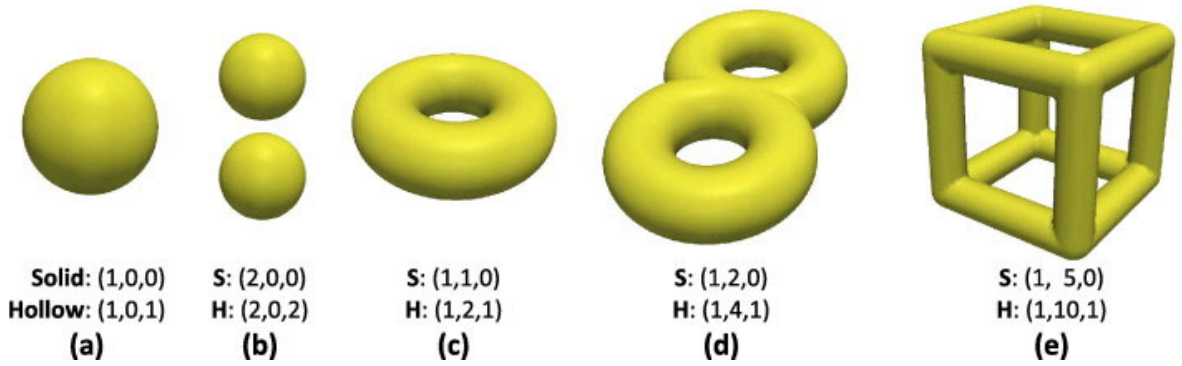

Figure 3.4. Betti numbers listed as a triplet (β_0, β_1, β_2) for simple three-dimensional solid objects: (a) single sphere, (b) two disjoint spheres, (c) torus, (d) double torus, (e) cubic frame (Herring et al., 2013).

3.4 Percolation theory at low flow rate

Trapped gas bubbles can reside in the center of a single pore or span multiple connected pores depending on several factors including local capillary pressure, pore geometry, and pore-throat aspect ratio (Khishvand et al., 2016). Fig. 3.5 shows the cumulative bubble size distributions *CDF*(*s*) in PP 355–425 μm after water flooding with different capillary numbers. The *CDF*(*s*) was calculated using the relative probability distribution frequencies *PDF*(*s*) of trapped gas bubbles of size *s*:

$$CDF(s) = \sum_1^s PDF(s). \quad (3\text{-}5)$$

The largest bubble sizes at the lowest $Ca = 1.0 \times 10^{-7}$ and highest $Ca = 3.8 \times 10^{-4}$ were 2.72 mm^3 and 0.083 mm^3, respectively. In order to compare the universal bubble size distribution at different capillary numbers, a normalized gas bubble size (i.e., bubble volume divided by the largest bubble volume) was used in this study. As shown in Fig. 3.5, the slope of the curve decreased significantly with increasing capillary number. The lower is the slope of the graph for a bubble size group, the more uniform is the trapped gas bubble size distribution.

Geistlinger et al., (Geistlinger et al., 2015) suggested that the trapped gas bubble size distribution in the capillary force dominated region exhibits a universal power law behavior:

$$CDF(s) = 1 - \left(\frac{k}{s}\right)^{\tau-1}, \quad (3\text{-}6)$$

where k denotes an arbitrary constant and τ is the Fisher exponent. A similar fitting method was applied to test whether the power law behavior is suitable in a dynamic flow region. As discussed in Geistlinger and Mohanmmadian (Geistlinger and Mohammadian, 2015) and Iglauer et al. (Iglauer et al., 2012), the consequent test of percolation theory has to exclude the smaller cluster from the dataset. Therefore, we took into account only data for large clusters, which contributed 90% of the total gas saturation, $V_{cutoff} = 90\%$. The critical τ value defined by the percolation theory in 3D porous media is 2.19 (Lorenz and Ziff, 1998). For all flow rates, the cumulative bubble size distribution was fitted to the universal power law given in Eq. (3-6), with $V_{cutoff} = 90\%$ and $\tau = 2.19$. The least-square fit was conducted for the selected data set as shown in Fig. 3.5 inset. For $Ca = 1.0 \times 10^{-7}$, the largest 553 out of the total 1207 bubbles were selected to fit the curves, with a relative error of 3.06%. The agreement between the experimental data and the universal power-law is a good evidence that the experimental bubble

size distribution is caused by a percolation-like trapping process (Geistlinger et al., 2015). At the low flow rate condition, the viscous forces can be ignored, and capillary forces dominate the trapping process. For higher capillary numbers, $Ca = 2.9 \times 10^{-5}$ and 3.8×10^{-4}, N_{cutoff} increased to 813/1538 and 976/1630, with relative errors of 4.92% and 5.51%, respectively. The higher value of N_{cutoff} means that the contribution of the smaller bubble size group increased with increasing water flooding flow rate. Although the relative errors are of small value even at the highest *Ca*, this does not mean that the experimental data exhibit universal power-law behavior. As shown in Fig. 3.5 (inset), the shape of the experimental data deviates significantly from the universal power law when $Ca = 3.8 \times 10^{-4}$. The relative error between the experimental results and the fitting values reached more than 40% for the selected smallest bubble volume. This indicates that the cumulative bubble size distributions in the high *Ca* experiment were no longer power-like, and that the capillary trapping process cannot be described by percolation theory. The viscous forces are competitive compared with capillary forces and jointly control the trapping process.

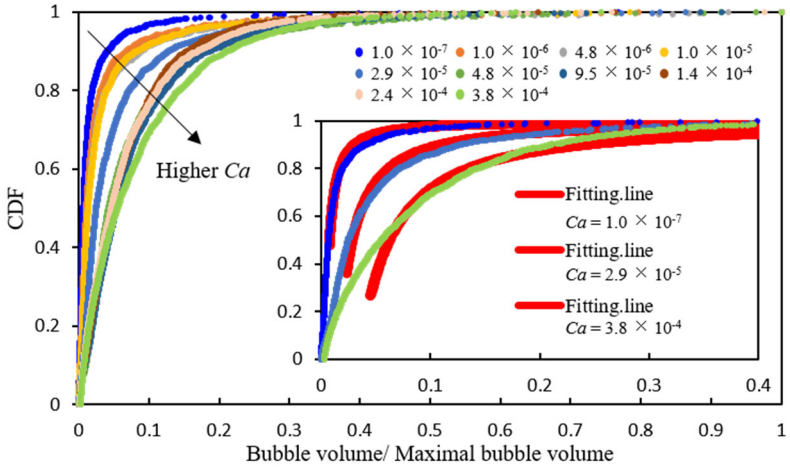

Figure 3.5. Cumulative bubble size distributions in PP 355–425 μm for different capillary numbers.

3.5 Desaturation curves with different injection strategies

Fig. 3.6 shows the 3D spatial distribution of trapped gas bubbles after water flooding at different flow rates. The different colors indicate individual bubbles. Under low *Ca* conditions, the trapped bubbles were mainly multi-pore bubbles, and the length of the largest cluster reached about 11 of d_{50} along the water injection direction. The buoyancy force limits the length of trapped clusters in the capillary force dominated region(Geistlinger and

Mohammadian, 2015). In a NAPL/water system, the largest NAPL cluster is much longer, about 27 of d_{50}, owing to the smaller density difference and the lower buoyancy force (Al-Raoush, 2014). As shown in Fig. 3.6, the size and total volume of trapped bubbles decrease with the increase of capillary number. Under the largest *Ca* condition, single-pore bubbles are the main contributors to the residual saturation. Figs. 3.6(a) and (b) show the 3D images of trapped bubbles in single particle size (PP 355–425 μm) and mixed particle size (PP 355–710 μm) porous media, respectively. The number of trapped bubbles in PP 355–710 μm is less than that in PP 355–425 μm, resulting from the larger size and smaller number of pores in the former.

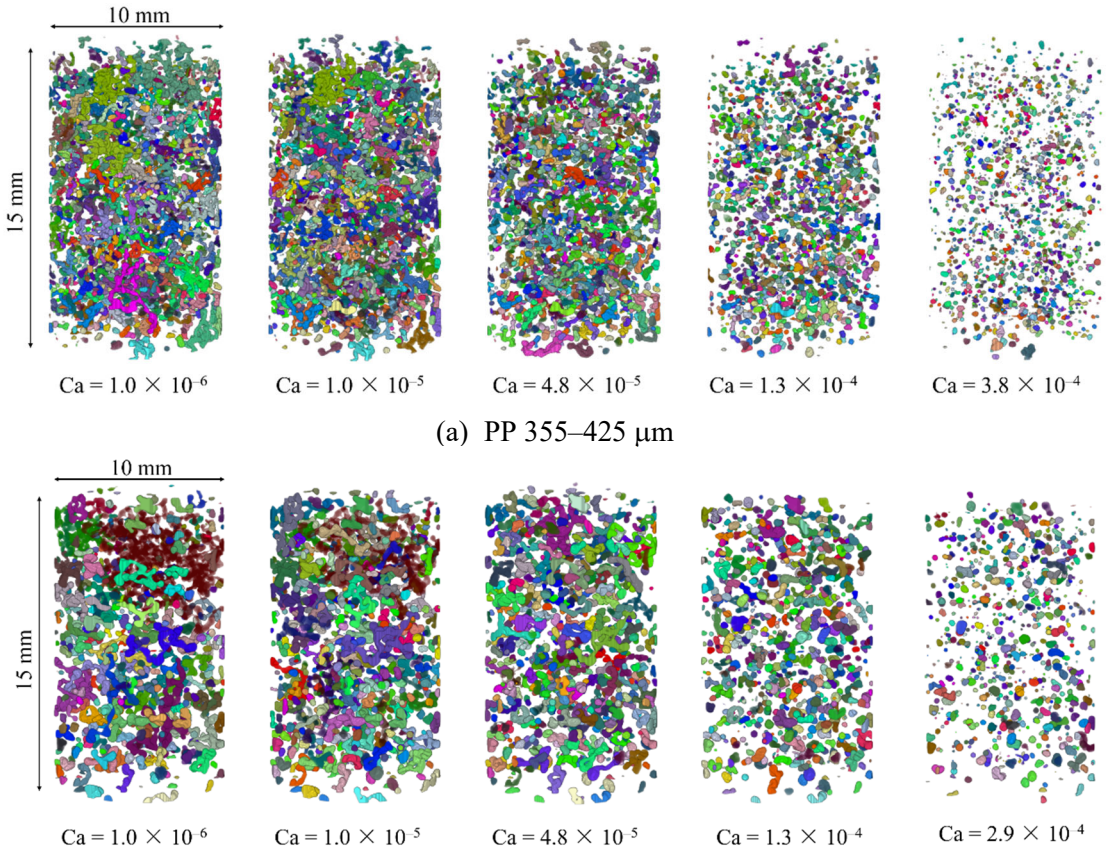

(a) PP 355–425 μm

(b) PP 355–710 μm

Figure 3.6 3D images of trapped bubbles at different capillary numbers.

Residual saturation as a function of capillary number is described as the *capillary desaturation curve* (CDC), which depicts the trapping and mobilization of residual fluids in porous media (Wang et al., 2019). According to different strategies for increasing flow rate, namely progressively increase and independently increase, there are two kinds of CDC. Fig. 3.7(a)

shows the CDCs of four packings using independently increase method, corresponding to Fig. 3.6. The normalized residual saturation was defined by dividing the value at the lowest *Ca*. In order to compare the CDCs, an experiment (PP 500-600) using progressively increase method was also performed. Due to the limitation of injection system, the maximal capillary number can only reach 3.8×10^{-4}. Oughanem et al. (2015) suggested that CDC can be predicted from the initial cluster size distribution and structure geometrical parameters. By estimating the viscous pressure along the trapped cluster, the maximal length of cluster was calculated. Assuming that all clusters longer than the critical length were removed from the porous media, then the residual saturation was predicted. As shown in Fig. 3.7(a), the predicted CDC showed good agreement with the experimental data for progressively increase method, but not for independently increase method. It indicated that the underlying mechanisms were different for the two CDCs.

For progressively increase method, the reduction in residual saturation was caused by the remobilization of largest ganglion due to the viscous force. The balance between the capillary pressure and viscous pressure decided the shape of CDC. For independently increase method, the residual saturation and morphology of trapped bubbles are controlled by the competition between snap-off and piston-like filling. The relative importance of displacement mechanisms depends on the water flooding rates (*Ca*). At low *Ca*, snap-off is the dominant displacement mechanism at pore scale, and the flow behavior can be described by percolation theory. The low flow rate allows water film that covers surface of solid grain to swell and consequent snap-off. Many bubbles are generated resulting from snap-off. On the other hand, at a higher *Ca*, bulk flow advances faster and there is insufficient time for water film swelling. As the capillary number increase, the snap-off is suppressed and residual saturation decreases.

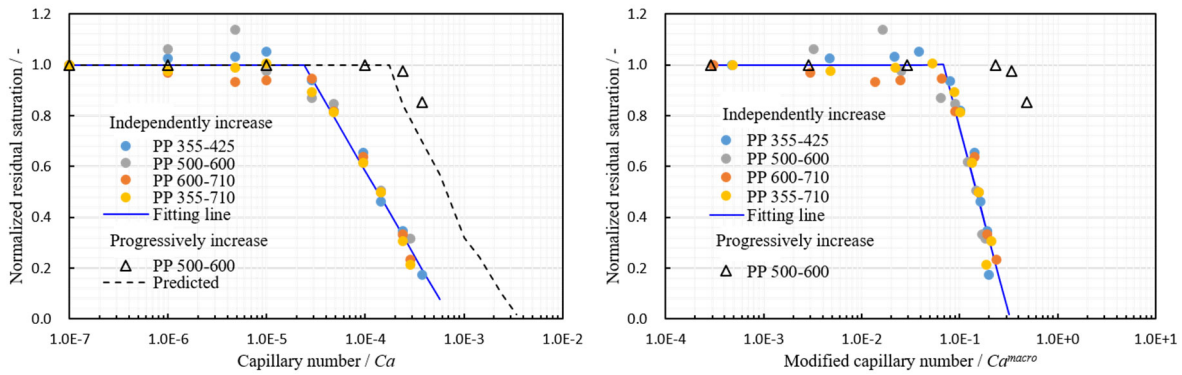

(a) Capillary number (b) Modified capillary number

Figure 3.7. Capillary desaturation curves for four porous media.

According to the topology of individual bubbles, the bubble patterns were classified into singlet trapped within a single pore, ganglia and cluster trapped within several multi pores. Fig. 3.8 shows the volume fraction distributions of the trapped singlet, ganglia, and cluster patterns versus capillary number. For the lowest *Ca*, singlet, ganglia, and cluster contributed about 14–19%, 16–40%, and 43–70% of the total trapped gas saturation, respectively. The volume fraction for the single-pore singlet was close to the value (16%) reported for a glass beads packed bed (Geistlinger and Mohammadian, 2015). As particle size increased, the total number of pores decreased, resulting in a decrease in the volume fraction of the cluster pattern. Additionally, a larger particle size produces a larger buoyancy force, which limits the length of trapped gas bubbles (Wilkinson, 1984). The mixed particle size PP 355–710 μm exhibited a high-volume fraction of cluster pattern owing to the potential for complex formation inside pores. In the capillary force dominated region, the volume fraction of the three patterns remained stable. Around the critical capillary number, $Ca = 1.0 \times 10^{-5}$ to 4.8×10^{-5}, a transition region was found, in which the volume fraction of ganglia reached a maximum. However, the saturation of the captured gas did not change markedly. At the highest *Ca* condition, no cluster can be observed, and the singlet pattern contributes more than 80% of the total trapped gas saturation.

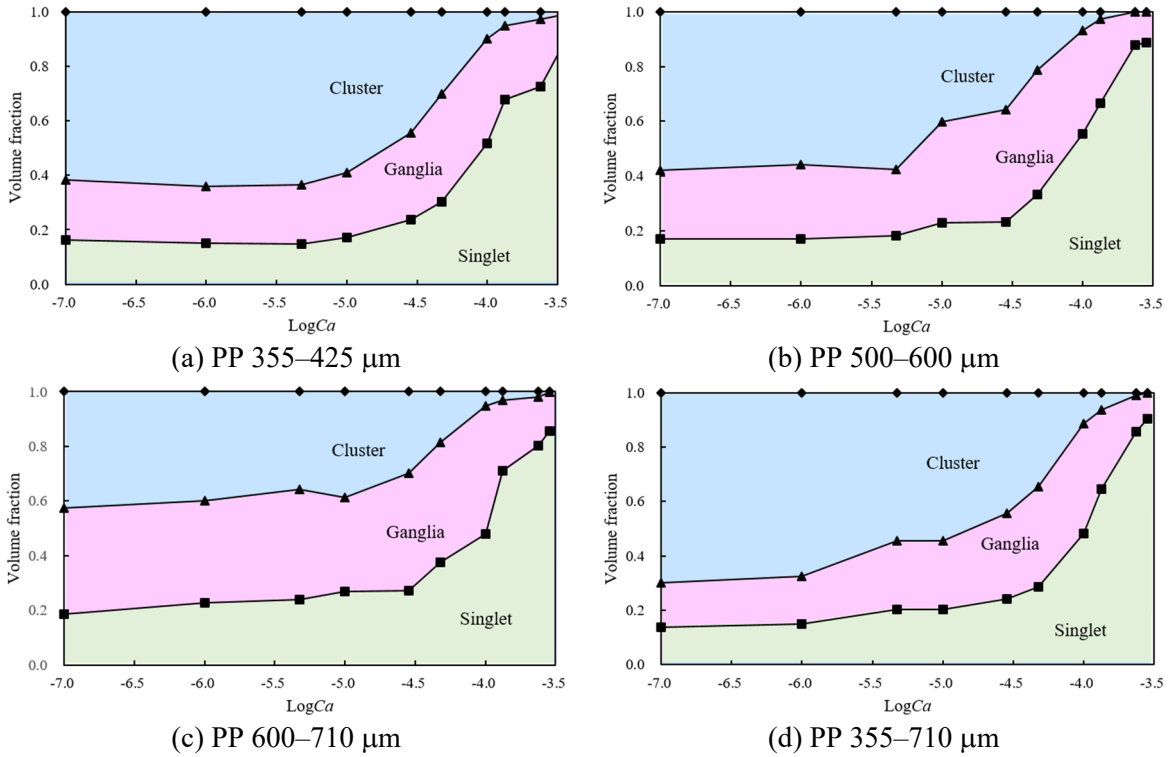

Figure 3.8. Volume fraction of singlet, ganglia, and cluster patterns for different capillary numbers.

3.6 Universal characterization of trapped phase

Individual bubble morphology can be characterized by plotting bubble volume versus surface area. All of the bubbles detected in each sample were averaged and are plotted in Fig. 3.9. Lines representing single-pore and multi-pore bubble morphology models are also plotted as black solid lines and dashed lines, respectively. For the single-pore model, the function of bubble surface and volume can be described by assuming that the bubble shape is close to spherical:

$$A_b = 4.836\, V_b^{\frac{2}{3}}, \tag{3-7}$$

where A_b and V_b are the bubble surface and volume, respectively. If the volume of a bubble is larger than a single pore, the bubble needs to occupy neighboring pores; thus channel-shaped bubbles form, which can be simplified as an elongated capsule. The diameter of this capsule is limited by the diameter of the pore, and the length of the capsule increases as the volume of the bubble increases. Thus, the bubble surface can be predicted as follows:

$$A_b = 4.189\, r_{p.median}^2 + \frac{2}{r_{p.median}} V_b, \tag{3-8}$$

where $r_{p.median}$ is the median pore radius. As shown in Fig. 3.9, the prediction value from the above two models yields an excellent match with the experimental values. Three typical flow conditions, $Ca = 1.0 \times 10^{-6}$, 4.8×10^{-5}, and 3.8×10^{-4}, were selected to illustrate the effect of capillary number on the bubble surface–volume relationships. Although the volume and surface of bubbles tend to become smaller, they still satisfy the single-pore and multi-pore models. For comparison, Geistlinger and Mohanmmadian (Geistlinger and Mohammadian, 2015) fitted the experimental data obtained from a glass bead packings into a power-law relationship $A_b \propto V_b^p$ and found the log-log plot $p = 0.833$, with relative errors of 7%. The single-pore and multi-pore models provide a more accurate assessment interface science in unconsolidated porous media.

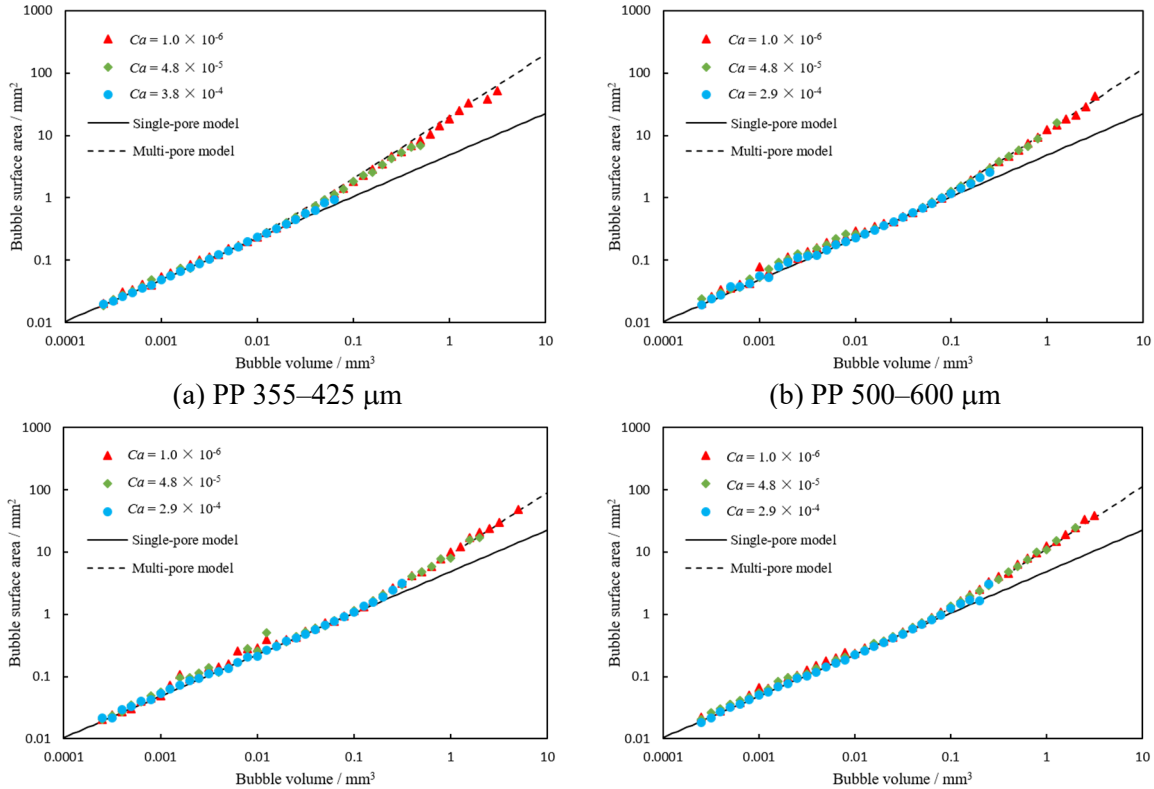

(a) PP 355–425 μm (b) PP 500–600 μm

(c) PP 600–710 μm (d) PP 355–710 μm

Figure 3.9. Average bubble surface area versus average bubble volume.

Trends in the total intrinsic and specific interfacial areas as a function of trapped gas saturation are plotted in Figs. 3.10 and 3.11, respectively. The intrinsic interfacial area defined by the ratio of the interfacial area to the gas volume, was applied to compare the morphological characterizations of NAPL entrapped in a porous medium (Corapcioglu et al., 2009). As shown in Fig. 3.10(a), the intrinsic interfacial area of smaller particles is lower than that of larger particles. In our previous study (Patmonoaji et al., 2018), we found that smaller particles generate smaller pores, and smaller pores generate smaller bubbles. With a similar shape, smaller bubbles exhibit a higher intrinsic interfacial area. Since their d_{50} were similar, PP 355–710 μm had a similar interfacial area to PP 500–600 μm. Because d_{50} is the main factor controlling pore size distribution, the intrinsic interfacial area can be normalized through multiplication by d_{50}. The normalized intrinsic interfacial areas of the four kinds of particle size porous media show the same trend as the trapped gas saturation, as shown in Fig. 3.10(b). When the gas saturation was above 6%, the normalized intrinsic interfacial area is independent of gas saturation, which also means it is independent of flow rate. The steeply increasing section for S_g < 6% suggests a change in bubble morphology to smaller bubbles at higher

surface area-to-volume ratios. This phenomenon concurs with previous observations of NAPL dissolution in a 2D micromodel (Corapcioglu et al., 2009).

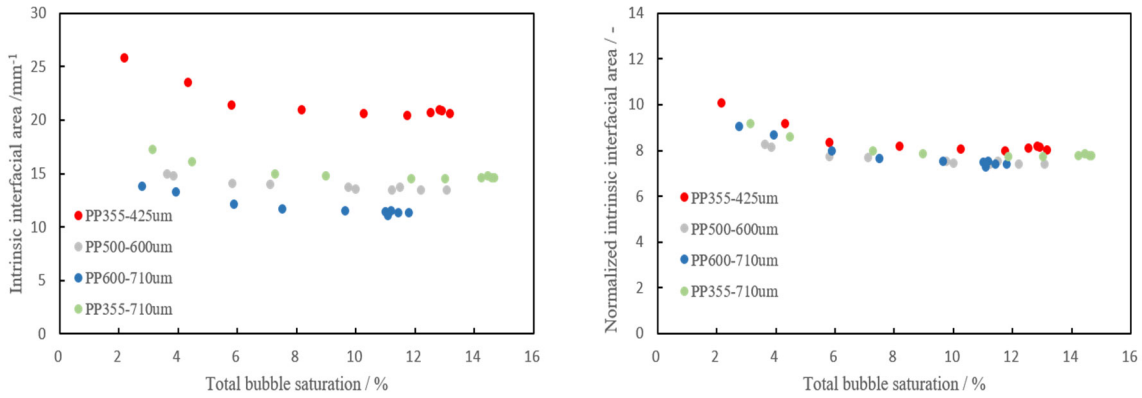

(a) Intrinsic interfacial area (b) Normalized intrinsic interfacial area

Figure 3.10. Intrinsic interfacial area and normalized intrinsic interfacial area versus the total bubble saturation.

Fig. 3.11 shows that the specific interfacial area decreases linearly with a decrease in gas saturation. This linear relationship has been extensively reported for gas or NAPL dissolution processes in porous media (Corapcioglu et al., 2009; Johns and Gladden, 2000; Patmonoaji and Suekane, 2017; Zhang et al., 2002). Gas/NAPL saturation diminished owing to dissolution, and large bubbles shrunk and broke up into smaller bubbles. In this study, the decreases in gas saturation and specific interfacial area were caused by the higher water flooding flow rate. Large clusters and ganglia broke into smaller singlets and were then mobilized under the high-pressure gradient along the flow direction. As shown in Fig. 3.11(a), smaller particle size had a higher specific interfacial area, which depends on the pore size distribution in the porous media. A similar normalized method was applied for the specific interfacial area through multiplication by d_{50}. The relationship between total gas saturation and normalized specific interfacial area followed a uniform trend for all particle sizes (Fig. 3.11(b)). An empirical model for the interfacial area in a plastic particles porous medium can be summarized as follows:

$$a_g * d_{50} = 3.79\, S_g, \tag{3-9}$$

where a_g is the interfacial area.

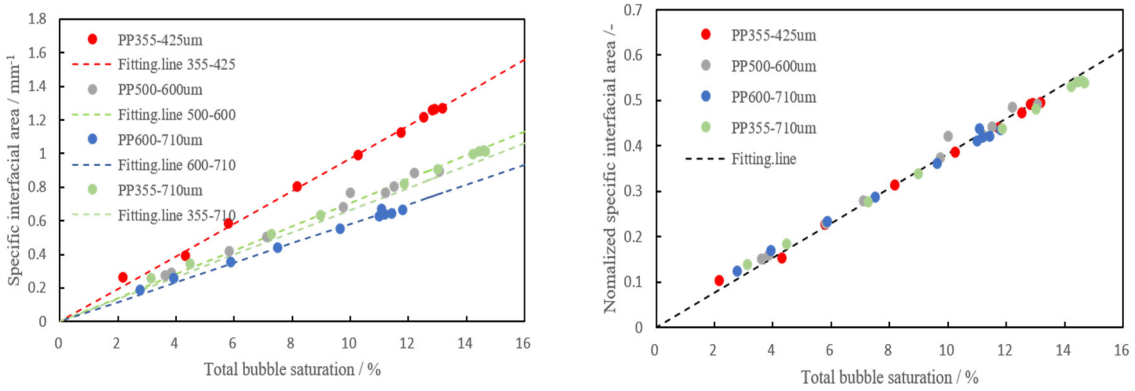

(a) Specific interfacial area (b) Normalized specific interfacial area

Figure 3.11. Specific interfacial area and normalized specific interfacial area versus the total bubble saturation

The trapped gas bubble surface contains two components, i.e., the gas–solid and the gas–water interfacial areas. The latter is also termed the meniscus interface, which is believed to the main factor affecting mass transfer. Fig. 3.12 shows the relationship between total gas/NAPL surface and meniscus interfacial area normalized by the volume of the porous media. Two literature data sets for unconsolidated porous media were selected for comparison with our results, including a gas/water system in glass beads packed beds (Geistlinger et al., 2014) and a NAPL/water system in sand packed beds (Al-Raoush, 2014). Al-Raoush (2014) suggested that meniscus interfacial area is proportional with total interfacial area. As shown in Fig. 3.12, the experimental data in sand packed beds was fitted with a linear relation of slope = 0.622. The slope indicates the ratio between the meniscus interfacial area and the total interfacial area. The value ranges from 0.50 to 0.76 in the sand packed beds, owing to the different particle shape and size distribution. In a uniform glass beads packed bed, the ratio remains stable, about 0.83 ± 0.01. In these two studies, the experiments were performed at low flow rates, where capillary forces dominated the trapping process. In addition to the particle size and shape, flow rate affects the morphology of the trapped bubbles and further affects the ratio between meniscus interfacial area and total interfacial area.

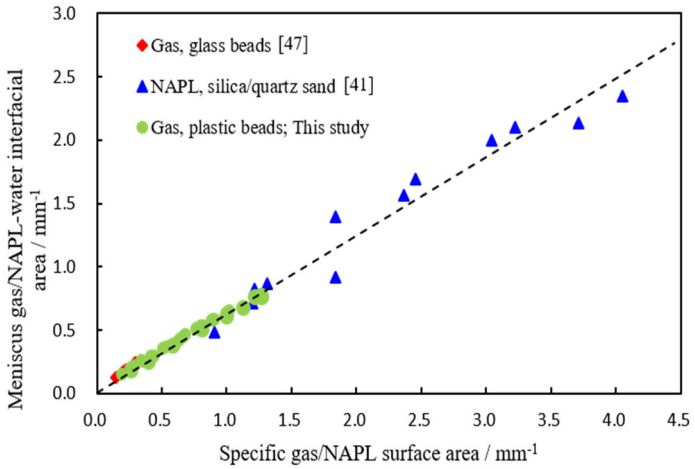

Figure 3.12. Relationship between total gas/NAPL surface area and meniscus interfacial area. For comparison, two experimental results were selected from literatures (Al-Raoush, 2014; Geistlinger et al., 2014).

Fig. 3.12 shows the ratio as a function of water flooding capillary number. At low *Ca* conditions, $Ca = 1.0 \times 10^{-7}$ to 2.9×10^{-5}, the ratio between meniscus interfacial area and total interfacial area is independent with the capillary number. Most saturation results from the multi-pore bubbles (cluster and ganglia), in which the meniscus/total interfacial area is stable, as shown in Fig. 3.13. The plot also shows that the meniscus/total interfacial area ratio tends to increase as particle size decrease. This may due to the higher porosity in the larger particle size porous media. A sharp increase occurs at $Ca > 2.9 \times 10^{-5}$, in which snap-off is suppressed and single-pore bubbles contribute a higher volume fraction of residual saturation. As shown in Fig. 3.13, for these single-pore singlets, the meniscus/total interfacial area ratio tends to increase as bubble volume decreases.

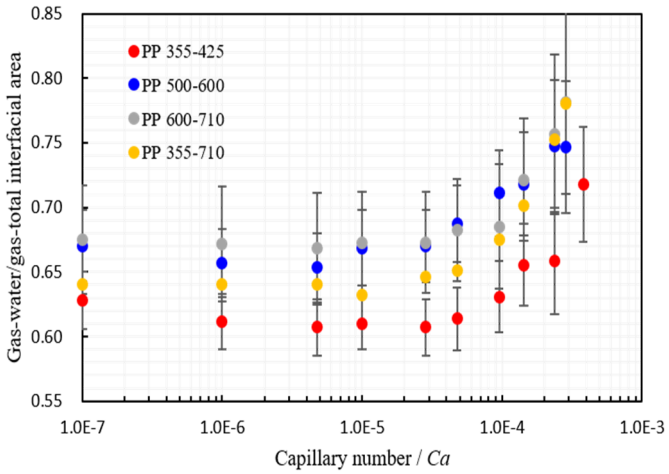

Figure 3.13. Gas-water/gas-total interfacial area ratio versus capillary number. Error bars represent the standard deviation in different slices.

3.7 Summary

In this study, we performed a systematic experimental study of capillary trapping in unconsolidated porous media. High resolution micro-tomography images were taken to determine the pore-scale morphological characterizations of trapped gas bubbles, including residual saturation, bubble size distribution and interfacial area. Ten different water flooding flow rates, spanning four orders of magnitude, were applied to investigate the impact of capillary number on these characterizations.

The distribution of trapped gas bubbles inside the porous media was qualitatively and quantitatively examined, after water flooding at vastly different capillary numbers. When *Ca* was between 1.0×10^{-7} and 1.0×10^{-5}, the residual gas saturation was independent of *Ca*, wherein the capillary force dominates the capillary trapping process. However, once *Ca* exceeded the critical value, as the capillary number increases, the snap-off is suppressed and residual saturation decreases sharply.

Under the lowest *Ca*, the singlet, ganglia, and cluster classes contributed about 14–19%, 16–40%, and 43–70%, respectively, of the trapped gas saturation in PP 355–425 μm, respectively. Higher flow rate generated much smaller trapped bubbles. Under the highest *Ca* condition, no clusters were observed, and the singlets contributed more than 80% of the residual gas saturation. For comparison with invasion percolation, the cumulative bubble size distribution was fitted to the universal power-law equation. The good agreement between the experimental

and predicted results indicates that invasion percolation describes the capillary trapping process in the capillary force dominated region. Percolation theory is invalid in the dynamic flow region, reflecting the fact that the bubble size distribution is no longer power-like.

The single-pore and multi-pore models provided a good prediction of the relationship between bubble volume and surface area, in both the capillary forces dominated region and the dynamic flow region. The specific interfacial area exhibited a linear relation with total gas saturation $a \propto S_g$. The effect of particle size on the intrinsic and specific interfacial area can be normalized through multiplication by d_{50}. With the increase in capillary number, the meniscus/total interfacial area ratio increased from 0.61 to 0.78, since the smaller singlet has a higher interfacial contact with the wetting phase.

The results described in this chapter have been published as: **Y. Hu***, Y. She, A. Patmonoaji, C. Zhang, T. Suekane, Effect of capillary number on morphological characterizations of trapped gas bubbles: Study by using micro-tomography, *Int. J. Heat Mass Transf.* 163 (2020) 120508

Chapter 4. Dissolution of residual phase in 2D and 3D porous media

In this chapter, we experimentally elucidated the pore-scale dissolution process and the macroscopic interphase mass transfer coefficient inside 2D and 3D porous media.

4.1 Introduction

In previous studies (Bradford et al., 2003, 1999; Miller et al., 1990), dissolution experiments were mainly conducted in opaque sand packings, and the dissolution rate was estimated based on the effluent concentration. It was considerably difficult to directly and accurately measure the interfacial area inside porous media because of the heterogeneous pore structures and limitation of experimental apparatus. Therefore, several methods have been proposed to indirectly measure the mass transfer coefficient. The mass transfer rate was estimated by using only the lumped mass transfer coefficient, which is the product of the mass transfer coefficient and specific interfacial area (Miller et al., 1990). The interfacial area could be evaluated with residual saturation by assuming uniform distribution of the trapped phase inside porous media. In such model, the trapped residual NAPL is assumed as spherical or cylindrical blobs (Geller and Hunt, 1993). More recently, the interfacial tracer method has been applied to measure the interfacial area of multiphase systems. For example, Jain et al. (Jain et al., 2003) studied the dependence of the fluid–fluid interfacial area on saturation and wettability using an anionic surfactant as the interfacial tracer. The interfacial area could be calculated from the mass reduction of the surfactant after it was passed through porous media. However, the interfacial area exhibits a complex interdependency with the morphology of the trapped NAPL because of the highly heterogeneous pore structures. The local dissolution behavior at the pore scale cannot be accurately described using the lumped mass transfer coefficient and assumption model.

With the development of nondestructive visualization technology, confocal microscopy, magnetic resonance imaging (MRI), and X-ray micro-computed tomography (micro CT) are considered to be useful tools for investigating the pore-scale characterizations of pore structures and the trapped phase inside porous media (Al-Raoush, 2014; Patmonoaji et al.,

2020, 2018; Werth et al., 2010). The grain geometry of the porous media affects the pore structure; thus, the magnitudes and configurations of the residual NAPL are also affected. The dissolution rate is affected by the heterogeneity of the pore space and the spatial distribution of the residual NAPL. The local pore-scale characterizations provide a reference for improving the accuracy of pore network modeling of the NAPL dissolution processes (Agaoglu et al., 2016; Aminnaji et al., 2019). The dissolution processes of NAPL in column packings have been visualized by the magnetic resonance imaging technology (Johns and Gladden, 1999; Zhang et al., 2002). Unfortunately, the local mass transfer coefficient could not be observed in these studies because of the low image resolution. X-ray CT allows us to obtain high-resolution images, based on which the saturation, cluster size distribution, and interfacial area of the residual phase can be determined. In addition, the CO_2 dissolution process in porous media was observed, and corresponding mass transfer coefficient was calculated using X-ray CT (Jiang et al., 2019, 2017; Patmonoaji and Suekane, 2017). Majority of these studies have focused on gas–liquid systems; in contrast, the pore-level liquid–liquid mass transfer characteristics associate with 3D porous media have been rarely investigated.

Extensive research has been conducted at the pore scale to evaluate the dissolution process of residual liquid phase in two-dimensional (2D) transparent micromodels. The pore-scale characteristics and transport phenomena of multiphase flow through porous media can be observed in real time by installing a high-resolution charge-coupled device (CCD) or a digital single-lens reflex (DSLR) camera (Geistlinger et al., 2005). Chang et al. (2019, 2016) conducted several pore-scale experiments to investigate the supercritical CO_2 dissolution process and the mass transfer behavior associated with a transparent micromodel. They analyzed both overall CO_2 depletion rate in the micromodel and individual bubble depletion rate in the pore space. Chomsurin and Werth (2003) measured the interfacial area of the trapped phase in homogeneous and heterogeneous micromodels during the dissolution process. Subsequently, the dimensionless modified Sherwood number and Sherwood number were used to evaluate the mass transfer rates at various flow rates. The dissolution behavior of different types of hydrocarbons, including trichloroethylene (Corapcioglu et al., 2009) and toluene (Bahar et al., 2018), were carefully studied by using an etched micromodel. The pore-scale characteristics associated with the multiphase-fluid distribution and flow in 3D porous media were significantly different from those associated with the 2D micromodel (Hu et al.,

2020a; Tsuji et al., 2016). However, the NAPL dissolution process has not been directly compared in 2D and 3D porous media.

4.2 Experimental setup and image processing

4.2.1 Materials

Micromodel: A homogeneous micromodel (EOR.PR, Micronit, Netherlands) was considered to be the 2D porous media. The designed pore space was etched in a silica plate to a nominal depth of 20 μm with hydrofluoric acid; subsequently, two symmetrically patterned glass plates were combined. Rock-shaped grains were reserved randomly in the silica plate, resulting in a global porosity of 0.57.

Packed bed*:* A porous medium was created using spherical glass beads with particle sizes of 600–710 μm. The beads were poured into a glass container with an inner diameter of 10 mm. The height of packing is approximately 14 mm; thus, the complete packing can be fully observed during the CT scan. The global porosity is measured about to be approximately 0.35 based on the dry-scan images of packed bed. High-permeability sintered glass filters were placed at the inlet to forming a uniform inflow during water flooding.

Fluid pairs: Trichloroethylene (TCE), which is a common groundwater contaminant, was considered to the model NAPL in this study. Table 4.1 presents the physicochemical properties of TCE and aqueous phase (deionized water). An agent is needed to dope in TCE or water to obtain a distinguishable contrast between TCE and water in the images obtained using the DSLR camera (RGB) or X-ray detector (16-bit grayscale). In the 2D micromodel, water was dyed using methylene blue with a concentration of 0.5 g/L. After dyeing, the water and TCE appeared blue and white in the RGB images, respectively. In the 3D packed bed, TCE was doped using iododecane (12% by weight), thus, its gray value was considerably greater than that of water in the CT images. Previous investigations have shown that doping with agents at the above percentages minimally affects the properties (Al-Raoush, 2014). In the water-NAPL system, the micromodel trends to be water wet and the packed bed is neutral wet.

Table 4.1. Properties of trichloroethylene and water.

Parameters	TCE	Water
Density (kg/m^3)	1420	998
Dynamic viscosity (mPa·s)	0.545	1.001
Solubility (kg/m^3)	1.28	
Diffusion coefficient (m^2/s)	9.1×10^{-10}	
Interfacial tension (mN/m)	36	

4.2.2 Experimental method

Fig. 4.1 schematically presents the experimental apparatus used in this study. The 2D micromodel and 3D packed bed were fed with the same fluid supply system. A syringe pump (KDS-200, KD Scientific Inc., USA) was connected to the inlet to control the volume and flow rates of the water and TCE. The outlet was connected to a waste reservoir at ambient temperature (293 K) and pressure (0.1 MPa). As shown in Fig. 4.1(a), the micromodel was placed horizontally and a DSLR camera (80D, Canon Inc.) with a macrolens (100 mm f/2.8L, Canon Inc., Japan) was used for visualizing the flow patterns. The whole micromodel can be sufficiently captured using the obtained RGB images with 6000 × 4000 pixels corresponding to 16 mm × 25 mm. In each experiment, the micromodel was initially saturated with water; subsequently, an image was captured as a reference to distinguish the pore space and grain. TCE was injected at 50 μL/min to achieve a high-saturation condition. The micromodel was then flushed with water at 25 μL/min until only the residual TCE remained in the pore spaces and blob mobilization ceased. This condition was recorded as the initial state, wherein a global NAPL saturation of 40% to 50% was maintained. Then, the flow rate was changed to the designed value to observe the dissolution process in micromodel. The residual TCE saturation was recorded with a time-lapse function using EOS Utility software (Canon Inc., Japan). The experiments were conducted at flow rates of Q = 2.5, 5.0, 10 and 25 μL/min (see Table 3).

The residual TCE distribution in the packed bed was captured using a high-resolution X-ray microtomography scanner (ScanXmate-RB090SS, Comscantechno Co., Ltd, Japan). As shown in Fig. 4.1(b), the sample was placed vertically at an intermediate point between the X-ray source and the detector. During scanning, the X-ray source and detector were rotated by 360° horizontally within 125 s. The images obtained from the detector were 992 × 992 pixels

with a resolution of 16.49 μm/pixel. In all experiment cases, scanning was conducted at 70 kV and 116 μA. The CT setting has been detailed in our previous study (Hu et al., 2020a). Before fluid injection, the sample was evacuated for 1 h and then saturated with degassed deionized water. A CT scan was then conducted to determine the pore space and grains in the packed bed. TCE was injected upward using a syringe pump at 2.0 mL/min to achieve a high-saturation condition. After this step, majority of the pores were invaded by TCE, and the global saturation exceeded 90%. Subsequently, the packed bed was flushed with 5 pore volumes of deionized water at 2.0 mL/min, and the TCE saturation decreased to approximately 30%. The residual TCE distribution inside the packed bed was recoded as the initial state. Next, the flow rate was changed to its designed value to observe the dissolution process in the packed bed. Several scanning processes were conducted to monitor the dissolution dynamic process. Water was continuously injected during the CT scan. The experiments were conducted at various flow rates of Q = 400, 650, 1 000 and 3 000 μL/min.

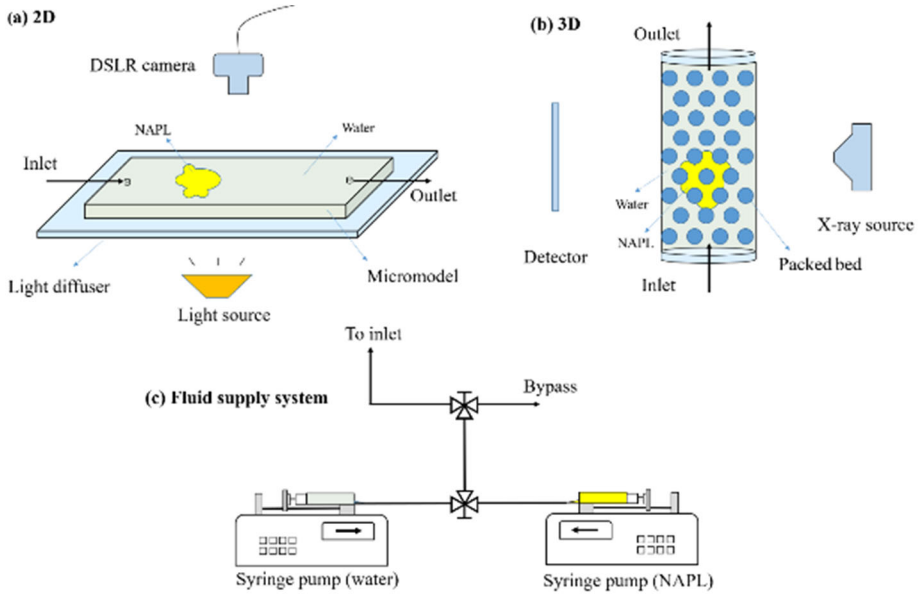

Figure 4.1. Schematic diagrams of experimental apparatus (a) 2D micromodel, (b) 3D packed bed and (c) fluid supply system.

4.2.3 Image processing

The RGB images of the micromodel were recorded during the dissolution processes. These images were imported into the ImageJ software (NIH) to remove the surrounding outer regions. Red channel was then picked from the RGB image for segmentation of three phases, i.e.,

NAPL, water and solid. The segmentation process for micromodel images with water or water-NAPL in the pores is illustrated in Fig. 4.2. The raw grayscale images were filtered to remove noise and preserve the edges using a non-local means filter. The filtering improves the signal to noise ratio significantly while keeping the phase boundaries preserved. After filtering, water saturated image was then segmented into solid and pore structures using Otsu's algorithm. The high-contrast image allows to accurately segment different phases. NAPL was extracted by subtracting the water-saturated image from the water-NAPL-solid image. After that, the gray value of NAPL phase was sufficiently higher than other phases. The intensity-based threshold segmentation method was applied to extract NAPL phase from difference image. Next, the three phases, i.e., solid, water, and NAPL, were combined and colored. The residual saturation and surface area were detected from the binary images of NAPL, water, and solid phase. The NAPL-water interfacial area was calculated as one half of the difference between the combined sum of the water and NAPL surface area and the solid surface area,

$$A_{n-w} = \frac{1}{2}(A_w + A_n - A_s), \tag{4-1}$$

where A_w, A_n, and A_s indicate the total surface areas of water, NAPL, and solid, respectively (Dalla et al., 2002). Similar image processing was also used in 3D CT experiments. For further details, the reader can refer to the previous work (Hu et al., 2020b).

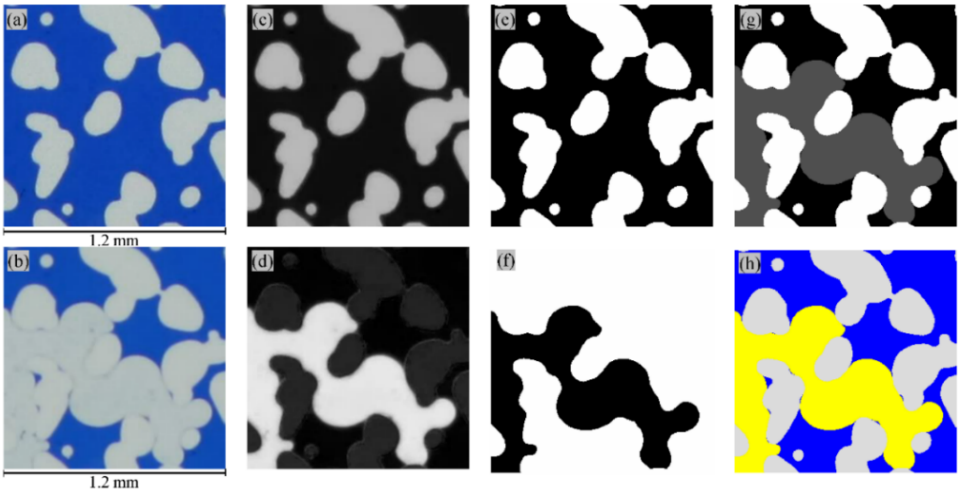

Figure 4.2. The image processing waterflow of the 2D micromodel. (a-b) raw images, (c-d) gray images of red channel, (e-f) binary images. (g) three phases combination image and (h) colored image. In colored image, yellow, grey, and blue colors represent NAPL, solid and water, respectively.

4.2.4 Pore and throat characterization

The pore–throat characteristics associated with the porous media were extracted from the binary images using OpenPNM (Gostick et al., 2016). As shown in Fig. 4.3, the pore network model is an approximate topological representation of the pore geometry. The corresponding date in the micromodel (10 mm × 10 mm) and the packed bed (5 mm × 5 mm × 5 mm) was presented in Table 1. The representative elementary volume analysis confirmed that the sub-volume can be representative of the entire sample. The coordination number of the partial-size micromodel is 2.72, which is consistent with 2.74 obtained from the entire micromodel. The coordination number of the partial-size packed bed is 6.1, which agrees well with previous classic study for random packing, around 6.0 (BERNAL and MASON, 1960). The dead pores represent the pores that are connected to only one throat. In this study, the ratio of dead/total pores in the micromodel was considerably higher, i.e., approximately 7.43%, than that in the packed bed, i.e., 1.48%. The macroscale physical and hydraulic properties of the micromodel are presented in Table 4.2.

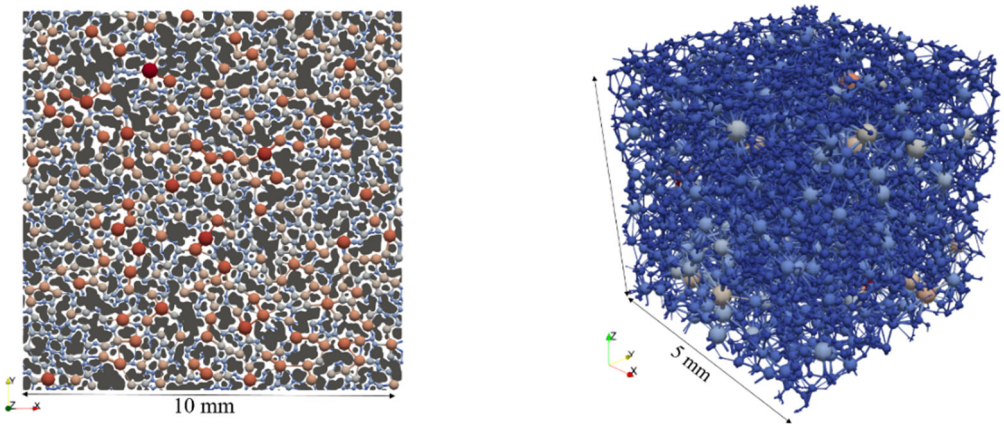

(a) 2D micromodel (b) 3D packed bed

Figure 4.3. Extracted pore networks of porous media, indicating the size and connectivity of pores (balls) and throats (cylinders).

Table 4.2. Macroscale physical properties and pore-scale characteristics of the micromodel and packed bed.

Macroscale (full size)			Pore-scale (partial size*)		
	Micromodel	Packed bed		Micromodel	Packed bed
Length (mm)	20	14	Number of pores	1 090	4 818
Width or diameter (mm)	10	10	Number of throats	1 476	14 618
Thickness (mm)	0.02	-	Dead/total pores	7.43%	1.48%
Porosity (-)	0.57	0.35	Mean pore radius (μm)	86.72	62.97
Mean grain diameter (mm)	0.34	0.66	Mean throat radius (μm)	63.57	51.19
Pore volume (mm^3)	2.28	133	Pore/throat radius ratio	1.36	1.23
Permeability (Darcy)	2.5	892	Coordination number	2.72	6.10

* Data was obtained from part of porous media shown in Fig. 4.3.

4.3 Local mass transfer calculation

For the calculation of mass transfer coefficient in a porous medium, the linear diving force model can be expressed as follows:

$$-\rho\varepsilon\frac{\partial S}{\partial t} = ka(C_s - C), \tag{4-2}$$

where ρ is the NAPL density [kg/m^3], ε is the porosity, S is the NAPL saturation, t is the dissolution time [s], k is the mass transfer coefficient [m/s], a is the effective specific interfacial area [1/m], C_s is the solubility limit of NAPL in water [kg/m^3], and C is the NAPL concentration in mobilized water [kg/m^3].

Previously, direct measurement of the interfacial area inside the 3D porous media was difficult because of the limitations associated with the capabilities of the experimental apparatus. In the present pore-scale experiment, we could accurately determine the interfacial area. Thus, lumped mass transfer coefficient (ka) and mass transfer coefficient (k) were evaluated in the 2D micromodel and 3D packed bed at various flow rates. However, the NAPL concentration in mobilized water (C in Eq. (4-2)) could not be measured directly from the obtained images. The simplified one-dimensional advection/dispersion equation was used to describe the NAPL dissolution process, where only the advection and source terms were considered.

$$-\rho\varepsilon\frac{\partial S}{\partial t} = v\frac{\partial C}{\partial x}, \tag{4-3}$$

where v is the pore velocity of mobilized water [m/s], x is the distance [m]. The simplified expression has been validated in our previous study (Patmonoaji and Suekane, 2017). To obtain the solute concentration at a given location and time. Eq. (4-3) was discretized by specifying a finite length (Δx) and a finite time (Δt)

$$C_{x+\Delta x} - C_x = -\frac{\rho \Delta x \varepsilon \Delta S}{v \Delta t}. \tag{4-4}$$

Based on Eqs. (4-2) and (4-4), the lumped mass transfer coefficient (ka) and mass transfer coefficient (k) can be calculated as follows:

$$ka = \frac{-\rho\varepsilon\frac{\Delta S}{\Delta t}}{C_s - C_{x,avg}}, \tag{4-5}$$

$$k = \frac{-\rho\varepsilon\frac{\Delta S}{\Delta t}}{a_{t,avg}(C_s - C_{x,avg})}, \tag{4-6}$$

where

$$C_{x,avg} = \frac{C_x + C_{x+\Delta x}}{2}, \tag{4-7}$$

$$a_{t,avg} = \frac{a_t + a_{t-\Delta t}}{2}. \tag{4-8}$$

$C_{x,avg}$ is the average solute concentration [kg/m^3] in between x and $x + \Delta x$, and $a_{t,avg}$ is the specific interfacial area [m^{-1}] in between t and $t - \Delta t$.

The water injection flow condition was evaluated by using two dimensionless parameters, i.e., the Reynolds number and the capillary number defined as

$$Re = \frac{\rho v d_{50}}{\mu}, \tag{4-9}$$

$$Ca = \frac{v\mu}{\sigma}, \tag{4-10}$$

where ρ, v, and μ are the density, velocity, and viscosity of water, respectively, and σ is the interfacial tension between water and NAPL. The mass transfer coefficient in porous media was normalized by the diffusion coefficient, was expressed as Sherwood number Sh and modified Sherwood number Sh':

$$Sh = \frac{k d_{50}}{D}, \tag{4-11}$$

$$Sh' = \frac{k a d_{50}^2}{D}, \tag{4-12}$$

where D [m^2/s] is the diffusion coefficient of the component and d_{50} is the mean grain diameter.

4.4 Visualization of dissolution process

Fig. 4.4 presents the progressive dissolution of the NAPL blobs in the 2D micromodel at Re = 0.56. The water was dyed blue, and the NAPL and grain were yellow and gray, respectively. The initial distribution of the NAPL blobs could be observed after water flooding at 25 μL/min corresponding to $Ca = 6.6 \times 10^{-5}$. The initial NAPL saturation was 26.48%, which gradually decreased to become 9.41% within 10 h of dissolution. The decreasing of NAPL saturation was considered to be mainly caused by dissolution because the flow rate during dissolution was lower than the required to remobilize the trapped blobs (Corapcioglu et al., 2009). Furthermore, the observation near the outlet indicated that NAPL did not accumulate before the low-permeability filter. The initial distribution of NAPL was uniform in pore space but became more nonuniform after several hours of water injection. The distribution of residual NAPL was related to the local pore structure of the micromodel. The NAPL blobs were concentrated in the pores near the two sidewalls; here, the pores exhibited poor connectivity, and some dead zones could be observed. In this area, the blobs were easily obscured by other blobs or grains, resulting in slow dissolution. The observation indicated that all the NAPL blobs were not exposed equally to the flowing water. Toward the center of the micromodel, the fluid–fluid interface receded faster on the windward side than on the leeward side.

As suggested by Corapciouglu et al. (2009), the fluid–fluid interfacial area can be segmented into two categories exposed to mobile and immobile water. Even in case of an individual blob, the fluid–fluid interface was not exposed equally to the flowing water. The dissolution rate via mass transfer was generally significant higher in the center of the micromodel owing to the preferential water flow paths inside the micromodel (Yiotis et al., 2019). The residual NAPL saturation did not change considerably from the inlet to the outlet because the distribution of pores and throats in the micromodel was homogeneous along the water injection direction, as shown in Fig. 4.4. During the dissolution process, the multi-pore blobs were observed to shrink in the NAPL–water interface. Finally, they formed smaller single-pore blobs. Subsequently, the smaller blobs were completely dissolved into mobilized water. After 10 h of water injection, majority of the trapped NAPL blobs were removed from the center of the micromodel owing to dissolution via mass transfer.

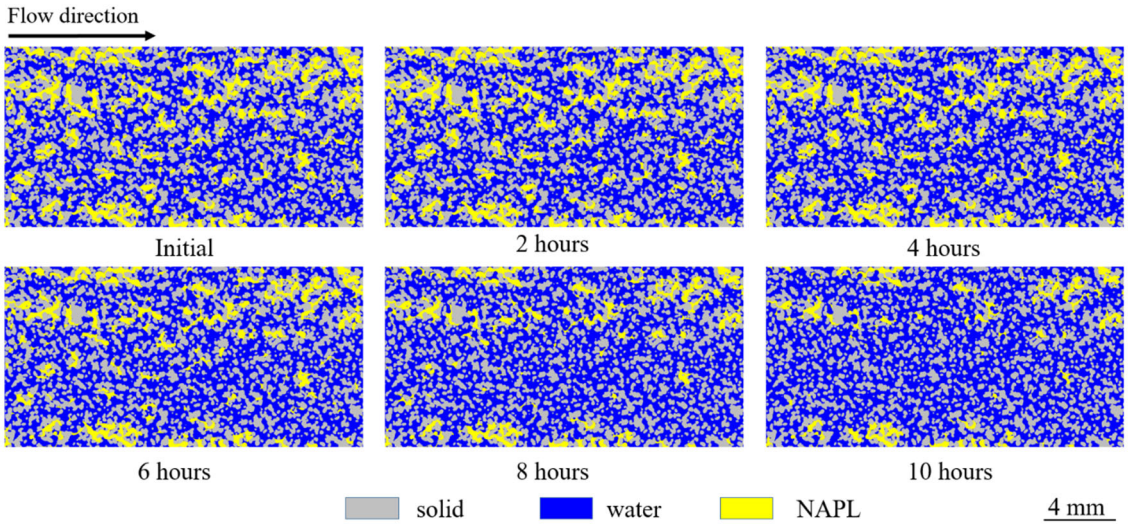

Figure 4.4. Time-lapse images of the dissolution process in the 2D micromodel at *Re* = 0.56.

Fig. 4.5 shows the 3D reconstructed images and 2D cross-sectional images of the packed bed during the dissolution process at *Re* = 0.44. The 3D rendering images present only the NAPL. The initial distribution of NAPL blobs was obtained after water flooding at 2.0 mL/min, corresponding to $Ca = 1.3 \times 10^{-5}$. The morphology of the trapped NAPL clusters in the packed bed was considerably more complicated when compared with that in the micromodel. NAPL was initially trapped with many different sizes and patterns after water flooding. At the beginning, most the residual saturation was contributed by the network-pattern NAPL clusters. When the water flowed through the porous medium, interphase mass transfer occurred at the interfaces between the trapped NAPL and mobile water. The meniscus and arc interfaces progressively receded in the pore space when NAPL dissolved into the water. Consequently, the well-connected clusters degraded into many smaller blobs. In the 2D cross-sectional images, the initial clusters were appropriately connected and spanned several adjacent pores. After several hours of dissolution, the area of NAPL in the cross-section reduced considerably, and majority of clusters occupied only isolated pores. The distribution of residual NAPL in XY plane was uniform because of the well-connected pore structures in the glass beads packing. Some redistribution may have been induced by the density difference between NAPL and water, especially during the early stages. As the dissolution progressed, the largest NAPL cluster gradually split into many isolated blobs, and the redistribution was suppressed. In this study, the experimental data obtained after serval hours of dissolution were selected to estimate the interphase mass transfer coefficient. The observation at the area near the inlet

indicated that NAPL did not accumulate at the bottom of the packed bed. Thus, the major decrease in the amount of entrapped NAPL can be attributed to dissolution. The NAPL saturation in the 2D and 3D porous media will be quantitatively analyzed in the next subsection.

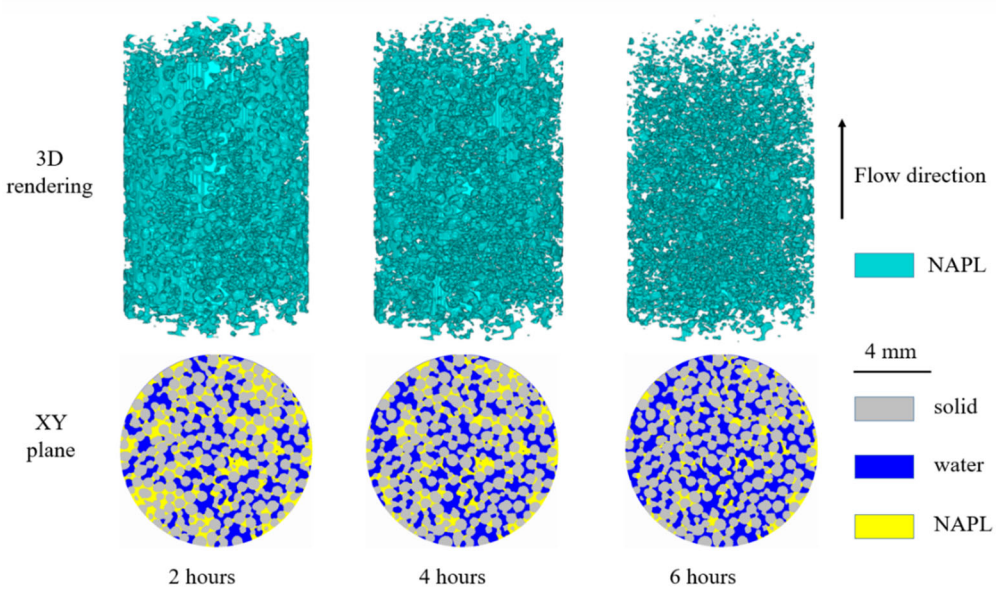

Figure 4.5. Time-lapse images of the dissolution process in the 3D packed bed at *Re* = 0.44.

4.5 Local residual saturation and concentration

Figs. 4.6 and 4.7 present the NAPL saturation distributions along the sample during the dissolution processes in the micromodel and packed bed, respectively. In the micromodel, the initial saturation after water flooding ranged from 0.2 to 0.4. The saturation profile exhibited slight fluctuations because of the local flow fields and porosity variations. The residual saturation gradually decreased as the dissolution progressed. There was no sudden increase in cross-sectional saturation along the sample, suggesting that the decrease in the amount of trapped NAPL was mainly attributed to dissolution. The NAPL degradation increased with increasing water flow rates. When *Re* = 0.28, the average saturation deceased from 0.25 to 0.10 after six hours of water injection, whereas dissolution reduced the average saturation from 0.23 to 0.10 in only three hours at the highest flow rate (*Re* = 1.40). The local reduction rate of the residual saturation varied over time, as shown in Fig. 4.6. The spatial distribution of the NAPL blobs changed as dissolution progressed, affecting the local flow characteristics near the fluid–fluid interface. Spatially, the residual saturation decreased uniformly along the sample. No dissolution front could be observed in the NAPL–water system, as reported by

Imhoff et al. (Imhoff et al., 1994). The packed bed was considerably small in our study, and there was insufficient space for the accumulation of the NAPL in mobile water.

The dynamic distribution of NAPL along the sample was captured according to the sequence of CT images, as shown in Fig. 4.7. *H* indicates the position from the inlet. When *Re* = 1.32, the saturation decreased drastically at the top; however, no significant change could be observed near the bottom (*H* = 1 – 6 mm) from *T* = 0.5 to 1.0 h. The nonuniform reduction of residual saturation can be attributed to redistribution during water injection. The saturation exhibited a similar decreasing trend after *T* = 1.0 h. As the dissolution progressed, the largest NAPL cluster gradually split into many segregated blobs, thereby achieving suppressed redistribution. At this stage, the major decrease in NAPL saturation can be mainly attributed to dissolution. Fig. 4.7 shows only the saturation profiles obtained during the stable dissolution process under other flow rate conditions. The obtained data were used to estimate the mass transfer coefficient.

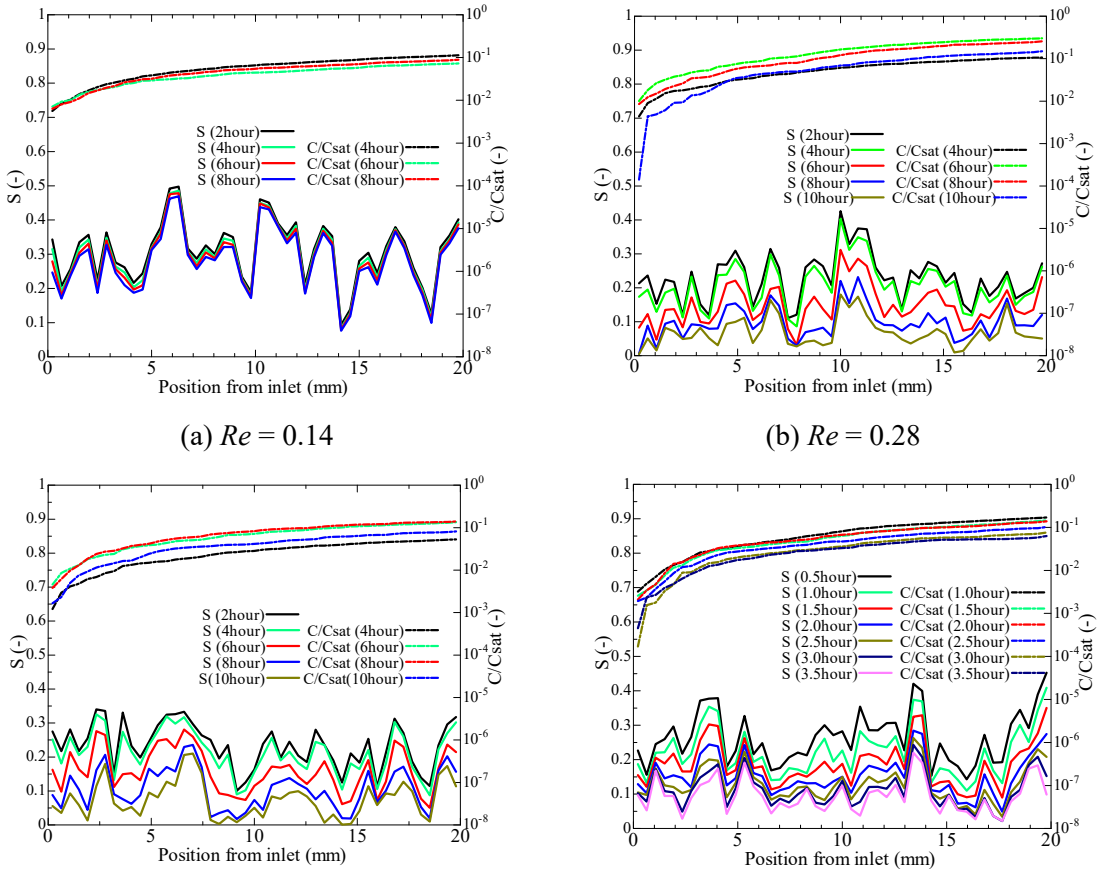

(a) *Re* = 0.14 (b) *Re* = 0.28

(c) *Re* = 0.56 (d) *Re* = 1.40

Figure 4.6. Distributions of NAPL saturation (*S*) and concentration (C/C_{sat}) along the flow direction in the 2D micromodel.

By assuming that the NAPL concentration in mobile water at the inlet was zero, the local concentration was calculated according to the Eq. (4-4). The NAPL concentration in mobile water was normalized based on the saturated concentration of NAPL (C_{sat}) with solubility at the same condition. Figs. 4.6 and 4.7 show the local normalized concentration (C/C_{sat}) of NAPL along the sample during the dissolution processes in case of the micromodel and packed bed, respectively. The concentration initially increased rapidly near the inlet and then increased gradually. The increasing NAPL concentration along the water injection direction can be attributed to the fluid–fluid mass transfer. The local mass transfer characteristics were considerably affecting by the pore geometry. The concentration increased more drastically in the packed bed near the inlet when compared with that in the micromodel, as shown in Figs. 4.6 and 4.7. This indicated a higher dissolution rate in the packed bed, which exhibited a lower porosity and a higher coordination number. The local mass transfer characteristics were also strongly related to the flow rate. As shown in Fig. 4.7, the maximal normalized concentration was approximately 10^{-1} at Re = 1.32, which is an order of magnitude lower than that at Re = 0.18. At low flow rates, there was sufficient resident time for water to contact with the trapped NAPL blobs; thus, a higher NAPL concentration could be observed in mobile water. The dissolution was driven by the difference between the solubility limit and the NAPL concentration in mobile water. The dissolution rate was expected to decrease as the dissolution driving force decreased along the water flooding direction. No significant dissolution front could be observed during the NAPL dissolution experiments, as shown in Figs. 4.6 and 4.7. The saturation distributions of NAPL along the sample were uniform during the dissolution processes. Imhoff et al. (Imhoff et al., 1994) reported that the dissolution would ceased when the downstream concentration in water reached the solubility limit; subsequently, a dissolution front would formed. In this study, the normalized concentration of NAPL in mobile water was lower than 1.0 at the outlet (Figs. 4.6 and 4.7), indicating that the mobile water was unsaturated. Therefore, the mass transfer process continued to occur at the outlet.

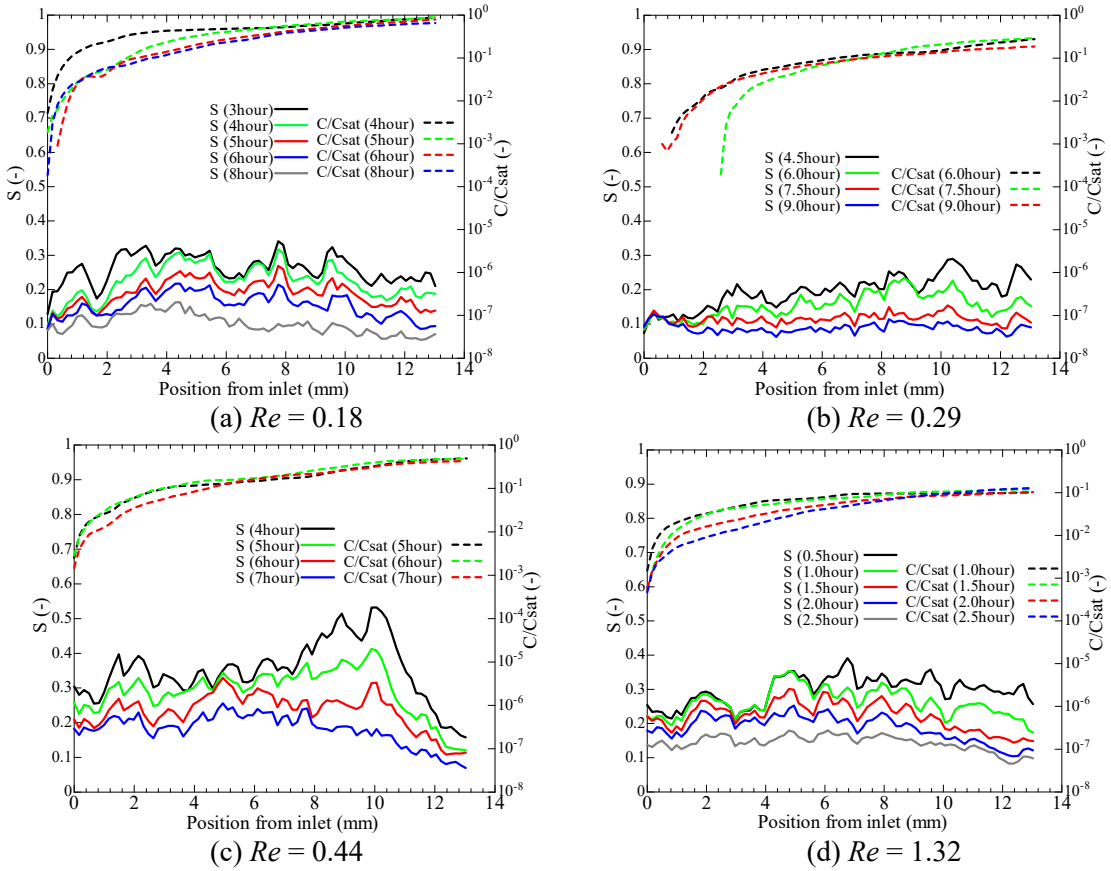

Figure 4.7. Distributions of NAPL saturation (S) and concentration (C/C_{sat}) along the flow direction in the 3D packed bed.

The transparent structure and dying agent allow to direct measurement of the interfacial area of the trapped NAPL in the micromodel. By assuming that the micromodel has uniform thickness (h), the interfacial area of NAPL (A) can be calculated from $A = P \cdot h$, where P is the perimeter of NAPL blobs obtained directly from images. The interfacial areas of the tapped NAPL usually include two parts: the interface between the trapped NAPL and solid and the interface between the trapped NAPL and bulk water (see Fig. 4.8). The latter (also known as the meniscus interface) is considered as the main site of mass transfer. Some researchers have argued that a thin water film exists between NAPL and solid and that mass transfer also occurs in case of the thin film. Thus, the effective interfacial area includes the NAPL–water and NAPL–solid interfacial areas. As shown in Fig. 4.4, only the NAPL–water interface progressively receded during water injection. Therefore, the mass transfer coefficient associated with porous media was calculated based on the meniscus interface area. A similar

process was also applied on the CT images stack to estimate the interfacial area of the packed bed.

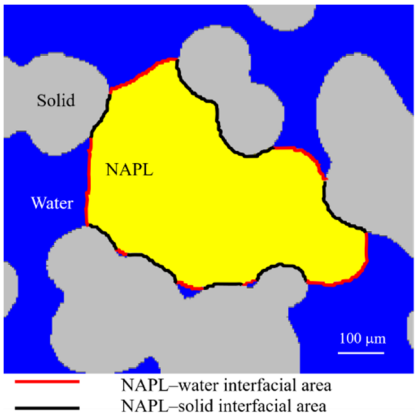

Figure 4.8. Distribution of NAPL–water and NAPL–solid interfacial areas in an isolated blob.

Fig. 4.9 presents the specific interfacial area and specific meniscus interfacial area as a function of NAPL saturation in porous media during dissolution processes. The function was usually described as

$$a = m_1 \cdot S + m_2, \quad (4\text{-}13)$$

where a is the specific interfacial area, S is the residual saturation, and m_1 and m_2 are the arbitrary numbers (Jiang et al., 2019). The specific interfacial area was proportional to the saturation in the micromodel. The volume and interfacial area decreased as the NAPL dissolved in the water. The specific interfacial area (a_t) and specific meniscus interfacial area (a_m) were linearly correlated with the NAPL saturation (S) as follows: $a_t = 9.58\,S$ and $a_m = 3.27\,S$. The ratio of the two slopes (~ 0.34 under all conditions) represents the ratio of the meniscus to the total interfacial areas. Similar linear relations have been reported in case of CO_2 (Patmonoaji and Suekane, 2017) and octanol (Johns and Gladden, 2000) dissolution. Zhang et al. (Zhang et al., 2002) investigated the trifluorobenzene (TFB) dissolution in silica gel packings using MRI. A power law relationship was applied to fit the TFB saturation and specific interfacial area. The exponents of the fitting relation were 0.97 and 0.99 for two porous media, indicating that the power law relation is very similar to the linear relation (i.e., exponent is equal to 1). When compared with the micromodel, the specific interfacial areas in the packed bed exhibited different trends, which reflected the different morphology of NAPL. This was mainly attribute to the heterogeneity of pore structures and the wettability of the

grain surface. As shown in Fig. 4.9(b), the specific total interfacial area decreased linearly with the residual saturation in the packed bed, whereas the specific meniscus interfacial area remained constant. As the dissolution progressed, the surface area of NAPL gradually decreased. Further, the largest cluster decomposed into many isolated small blobs. Small blobs have a higher ratio of the meniscus interfacial area. Thus, the ratio of the meniscus to total interfacial areas increased from 0.22 at S = 39.12% to 0.36 at S = 8.25%.

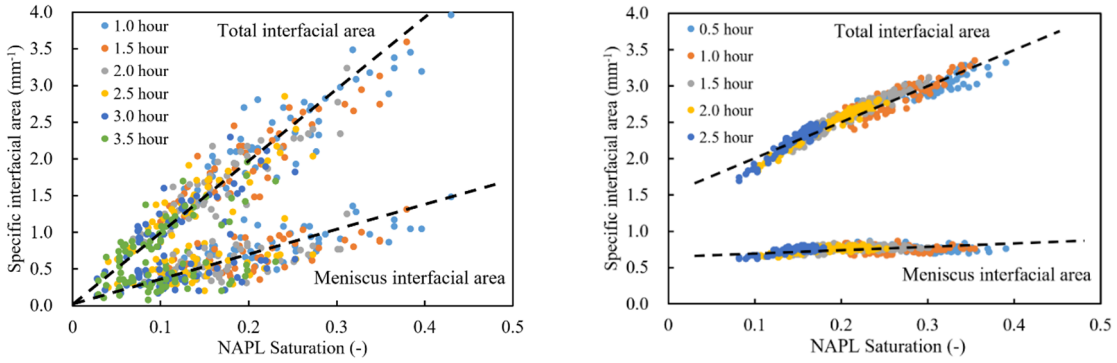

(a) 2D micromodel (b) 3D packed bed

Figure 4.9. Specific NAPL interfacial areas versus saturation at Re = 1.40 in the 2D micromodel and at Re = 1.32 in the 3D packed bed.

4.6 Local mass transfer coefficients

According to the Eqs. (4-5) and (4-6), the local lumped mass transfer coefficient ka and mass transfer coefficient k corrected with the concentration and interfacial area were estimated, as shown in Figs. 4.10 and 4.11. The value of ka was approximately three orders of magnitude greater than the value of k. The lumped mass transfer coefficient is the product of the mass transfer coefficient and the specific interfacial area. In the micromodel, the specific interfacial area ranged from 0.3×10^{-3} m^{-1} to 1.2×10^{-3} m^{-1} during the dissolution process expect for last record time T = 3.5 hour. Although the NAPL concentration in mobile water increased along the sample and the corresponding driving force decreased, the mass transfer coefficient was independent of the position. In the micromodel, the mass transfer coefficient was uniformly distributed; however, some deviations could be observed in the packed bed at early stage. As shown in Fig. 4.10(d), the values of local mass transfer coefficient from H = 1 to 6 mm were missed at T = 0.75 h primarily because of the redistribution of NAPL owing to gravity. In the later stage of the dissolution process, the local mass transfer coefficient distribution became

increasingly uniform along the sample, confirming that the NAPL saturation was reduced by dissolution and that the redistribution was suppressed. The mass transfer process is also considerably dependent on the local flow velocity, and a higher flow rate means a higher mass transfer coefficient. In the micromodel, the local lumped mass transfer coefficient and mass transfer coefficient increased from approximately 10^{-3} s^{-1} and 10^{-6} m^{-1} s, respectively, at *Re* = 0.14 to 10^{-2} s^{-1} and 10^{-5} m^{-1} s, respectively, at *Re* = 1.40. The overall mass transfer coefficient was calculated by averaging the local values along the sample.

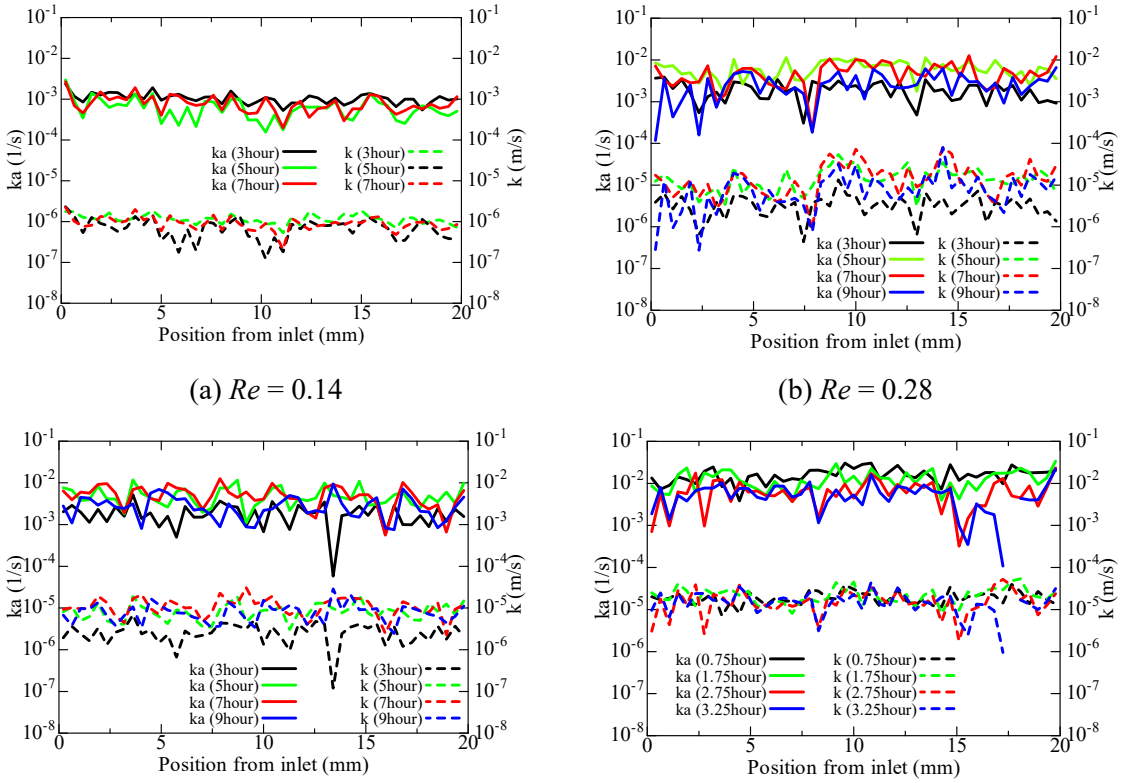

(a) *Re* = 0.14

(b) *Re* = 0.28

(c) *Re* = 0.56

(d) *Re* = 1.40

Figure 4.10. Local lumped mass transfer coefficient and mass transfer coefficient versus position in the 2D micromodel.

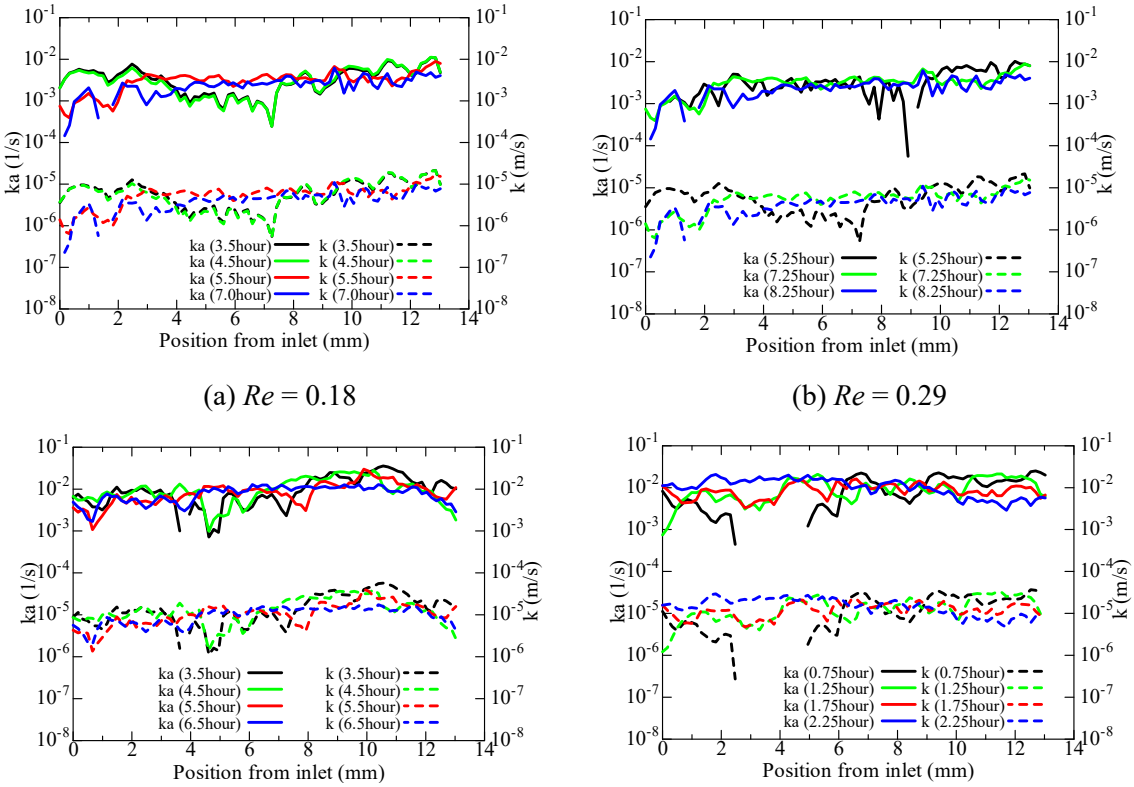

(a) Re = 0.18 (b) Re = 0.29

(c) Re = 0.44 (d) Re = 1.32

Figure 4.11. Local lumped mass transfer coefficient and mass transfer coefficient versus position in the 3D packed bed.

The mass transfer coefficient was usually normalized by molecular diffusion, expressed in terms of the Sherwood number Sh (Eq. (4-11)). The Reynolds number is an important dimensionless parameter used to describe the fluid-flow conditions in porous media. Generally, the empirical correlation of velocity-dependent mass transfer can be approached with a power function as $Sh \sim Re^n$, where n is an arbitrary constant. We generated two empirical models describing the relation between the Sherwood number and Reynolds number to compare the interphase mass transfer processes in the 2D micromodel and 3D packed bed.

$$\text{2D micromodel: } Sh = 1.98Re^{0.79}, \tag{4-14}$$

$$\text{3D packed bed: } Sh = 11.06Re^{0.56}. \tag{4-15}$$

The experimental data and empirical model were compared in Fig. 4.12. The exponent value of the packed bed is in reasonable agreement with that of the CO_2 dissolution experiment (n = 0.645) reported by Patmonoaji and Suekane (2017). The Sherwood number was considerably greater in the packed bed than that in the micromodel. The difference between the mass

transfer coefficient of the micromodel and packed bed can be primarily attributed to the properties of inherent pore structures, including coordination number and connectivity. Table 4.2 indicated that the coordination number is higher in the 3D random packings than that in the 2D micromodel. A higher coordination number means that the mobile water can effectively bring effusion to the downstream, enhancing the local interphase mass transfer. As shown in Fig. 4.4, there are many dead zones near side walls in the micromodel, limiting the rate of NAPL dissolution into water in this area. In the spherical particle packed bed, the well-connected pores allow the mobile water and trapped NAPL to fully exchange mass at their interface. The results indicated that a well-connected pore structures will facilities the dissolution and mass transfer behaviors inside porous media.

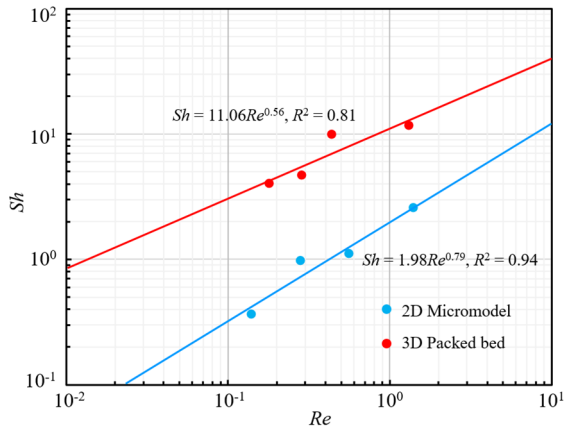

Figure 4.12. Comparison of Sherwood number and Reynolds number in the 2D micromodel and 3D packed bed.

4.7 Summary

The primary objective of this study was to elucidate the pore-scale dissolution process and the macroscopic interphase mass transfer coefficient in porous media. The dissolution process of NAPL trapped inside porous media has been conducted in a 2D micromodel and a 3D packed bed. Nondestructive visualization technologies (DSLP camera and micro CT) were applied to determine the pore-scale characteristics of the residual phase during the dissolution process. According to the linear driving force model, the local NAPL concentration profile in mobile water can be predicted from saturation. The lumped mass transfer coefficient *ka* and mass transfer coefficient *k* corrected with concentration and interfacial area were estimated. The overall mass transfer was expressed as a dimensionless parameter, i.e., the Sherwood number

Sh, and the two porous media were compared to study the impact of pore-scale-correlated heterogeneity on dissolution process.

The dynamic dissolution process showed that in case of the micromodel, NAPL disappeared much faster in the central area than at the side wall during water injection. Further, all blobs were not equally exposed to flowing water, and the dissolution rate was considerably low in the dead-end area. The disappearance of residual NAPL in the packed bed was more uniform than that in the micromodel because the proportion of dead pores was low in this structure. The saturation of NAPL decreased uniformly from the inlet to outlet, and the dissolution front expected in a gas–water system was absent. As NAPL dissolved in mobile water, its aqueous concentration increased along the sample and the corresponding difference in concentration increased. The local mass transfer coefficient remained stable along the sample, indicating that the mass transfer coefficient was independent of the difference in concentration.

The mass transfer coefficient profiles showed that the value of *ka* is approximately three orders of magnitude greater than the value of *k* because the magnitude of the specific interfacial area was about 10^{-3} m^{-1}. In addition, the mass transfer process was considerably dependent on the Reynolds number, and a higher flow rate indicates a higher mass transfer coefficient. Further, two empirical models describing the relation between the Sherwood number and Reynolds number were generated, i.e., $Sh = 1.98Re^{0.79}$ for the 2D micromodel and $Sh = 8.33Re^{0.56}$ for the 3D packed bed. The overall mass transfer coefficient was higher in the packed bed compared with that in the micromodel under the Darcy flow conditions. The difference between mass transfer coefficients of micromodel and packed bed can be primarily attributed to the inherent pore structures.

The results described in this chapter have been published as: **Y. Hu**, A. Patmonoaji*, H. Xu, K. Kaito, S. Matsushita, T. Suekane, Pore-scale investigation on residual nonaqueous phase liquid dissolution and mass transfer in 2D and 3D porous media, *Int. J. Heat Mass Transf.* 169 (2021) 120901.

Chapter 5. Dissolution of residual phase in water-wet and neutral-wet porous media

In this chapter, capillary trapping and dissolution processes were imaged via X-ray computed microtomography in natural porous media which exhibit different degrees of uniform wettability.

5.1 Introduction

In Chapters 3 and 4, we have studied the capillary trapping and dissolution processes in uniform wettability porous media. Although the surface of natural sand is usually water wet, various reasons may change the wettability of soil, such as the organic contaminant, surface roughness, mineral composition, and sorption of active matters to the solid surface (Al-Raoush, 2009). Practically, solid surface varies from water-wet to NAPL-wet in natural systems. Wettability plays an important role in controlling the configuration of immiscible fluids in porous media, thus affecting the flow and transport of NAPL in the subsurface. Extensive experimental and simulation studies investigated the influence of wettability on multiphase flow in pore space, including displacement mechanisms (Hu et al., 2017; Zhao et al., 2016), residual trapping (Al-Raoush, 2009; Iglauer et al., 2012), interfacial area (Bradford et al., 2000; Jain et al., 2003), relative permeability and capillary pressure (Nemer et al., 2020; Zhao et al., 2018), fluids topology (Herring et al., 2016; Liu et al., 2018), pore and throat occupation (Geistlinger and Zulfiqar, 2020), and NAPL dissolution (Seyedabbasi et al., 2008; Zhao and Ioannidis, 2007).

Different spatial configuration of residual NAPL caused by wettability may further affect the dissolution behavior in porous media. Bradford et al. (1999) experimentally studied the dissolution of residual tetrachloroethylene (PCE) in porous media comprising fractional wettability sands and found that wettability has a significant impact on dissolution behavior. According to the effluent concentration curves, the results indicate that PCE dissolves much faster in the fractional wettability systems than those in the water-wet medium. In the fractional wettability medium, the presence of PCE films coating the NAPL-wet sands was believed to increase the dissolution rate. However, due to the limitation of the device in that study, the amount of the PCE films was not possible to be measured. The ganglia distribution

and film present a nonlinear relationship between the mass fraction of water-wet and NAPL-wet particles. Bradford et al. (2000) further developed a mathematical modeling of residual NAPL dissolution for the system comprising fractional wettability sand. By separately estimating the film-water and blob-water mass transfer coefficient and interfacial area, a predictive model was developed to calculate the lumped mass transfer coefficient in the fractional wettability system (Bradford and Abriola, 2001). To the best of our knowledge, there are no research has been conducted to investigate the effect of wettability on NAPL dissolution from pore level.

To mimic the complicate subsurface condition, water-wet and neutral-wet silica sand were prepared for investigating the influence of wettability on these behaviors. X-ray computed microtomography was used to image the dissolution process in opaque porous media. The mass transfer coefficient was calculated from time-resolved images, as described in Chapter 4. Thus, this study provides a better understanding of the pore-scale dissolution behavior of residual NAPL, which may also contribute the development of predictive models for liquid-liquid mass transfer in porous media.

5.2 Materials and methods

5.2.1 Silica sand

In this study, experiments were carried out with silica sands representing natural porous media. Natural silica sand has an angular shape and roughness surface compared with spherical glass beads (See Fig. 5.1). Mixed particles were sieved to a relative uniform size distribution 500–600 μm using a vibrating sieve machine. The average equivalent particle diameter (d_{50}) was 550 μm. Then, particles were packed in an X-ray transparent glass tube with an inner diameter of 10.5 to a height of approximately 30 ± 1 mm. To generate a more homogenous unconsolidated porous medium, the glass tube was shaken frequently during packing. Close random packing was achieved for all experiment cases, resulting a global porosity of 0.43 ± 0.1. The absolute permeability was measured through a water flooding experiment, which is about 1.4×10^{-10} m^2. Two sintered glass frits were placed on both ends of the column to support the unconsolidated porous medium and form a uniform incoming flow. The experimental setup, flow apparatus, and fluids properties have been described in Chapter 4.

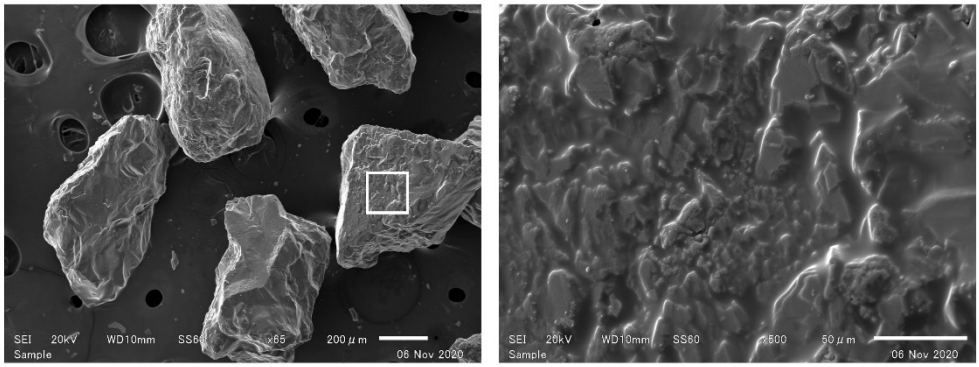

Figure 5.1. Scanning electron microscopy image of the silica sand with scaler (a) 200μm and (b) 50μm.

5.2.2 Wettability alternation

Before the experiment, a series of procedures were carried out to clean the silica sands. First, particles were washed with an ultrasonic water bath (ASU-6M, As One, Japan.) for 30 min to remove surface dust, and then dried in a heat flat. To remove potential organic contaminants, the dried particles were rinsed with toluene, ethanol, and water in sequence (Herring et al., 2016). After washing, sand was evenly placed on a flat to heat 3 h (110℃), then sieved again to eliminate the effect of cracking on the size distribution during the heating process. After that, these particles were regarded as original natural sand in this study and rendered water-wet characteristic in NAPL-water system.

To alter the wettability of silica sands, a coating solution was prepared by diluting octadecyl-trichloro-silane (OTS) with toluene. The coating method has been proven to be a robust and versatile method for the silica surface modification(Geistlinger and Zulfiqar, 2020; Herring et al., 2016). The treatment process can be summarized as follows: a solution is prepared by diluting OTS in toluene. Then add the diluted solution to clean dry sand until it is fully saturated. After stirring the particles and the solution for 30 minutes, rinse the wet particles with toluene, ethanol, and water successively, and the place it evenly on a flat plate in a fume hood and heat it for 3 hours (110°C). The NAPL-water contact angle of the glass slide was measured and assumed to represent the ideal condition of the sand surface. As shown in Fig. 5.2, the average contact angles of untreated and low OTS concentration treated and high OTS concentration treated slides were 137.5°, 75.3° and 15.6° respectively. The sand after OTS coating is treated as neutral-wet and NAPL-wet in the NAPL-water system.

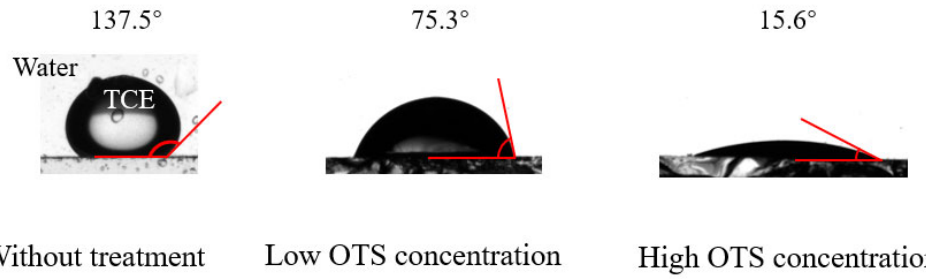

Figure 5.2. Contact angle with treated and untreated glass plate. The contact angle can be changed by using different OTS cibcebtration.

5.3 Morphology of residual phase

After being packed, the column was fully saturated with water using a vacuum chamber. The equivalent 6 pore volume of TCE was then pumped upward into the column at flow rate of 2.0 ml/min using syringe pump. Degassed deionized (DDI) water was then flushed downward at 1.0 ml/min to displace TCE. The capillary number for this water flooding was calculated to be 5.0×10^{-6}, which falls within the capillary force domain region as described in Chapter 3. Once the initial saturation was established, a CT scan was conducted to image the configuration of fluids inside porous media.

To investigate the impact of wettability on NAPL capillary trapping during water flooding, three typical contact angles were selected for visualizing of residual phase in pore space. The configuration of residual NAPL blobs is presented in Fig. 5.3 for the three porous media. Different colors represent the individual NAPL blobs. In water-wet and neutral-wet systems, residual NAPL blobs were mainly isolated and evenly distributed throughout the imaged region, longitudinally and radially, with no preferential accumulation at certain locations. NAPL blobs vary greatly in both size and shape, ranging from small singlet to large cluster. The residual NAPL rendering a distinguish morphology in NAPL-wet medium compared with other two media. In NAPL-wet system, residual NAPL was a well-connected structure throughout the entire porous medium and contributed to most of the saturation. In addition, there are a few small, isolated blobs near the column wall. Considering the difficult on accurately obtaining the interfacial area of film in NAPL-wet porous medium, only water-wet and neutral-wet systems were selected for further analysis and dissolution experiments.

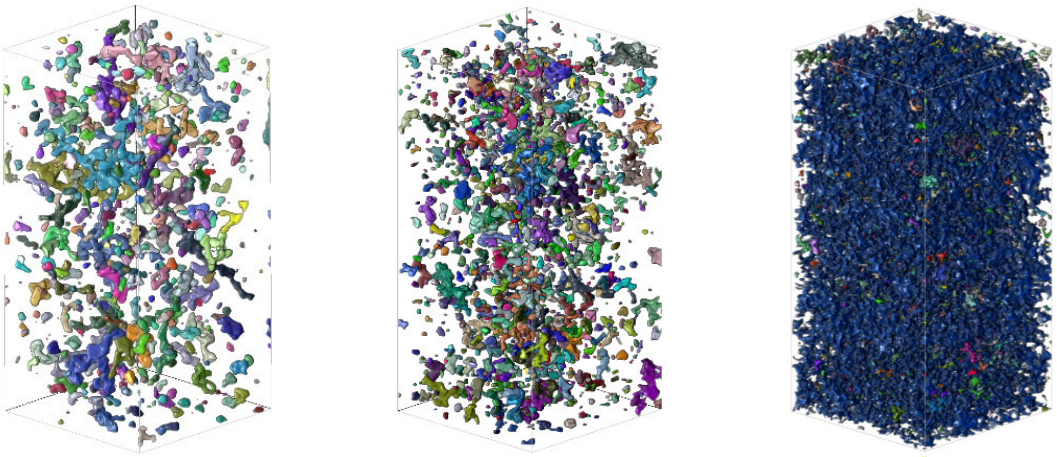

(a) water-wet (b) neutral-wet (c) NAPL-wet

Figure 5.3. Configuration of residual phase in pore space with different wettability

Fig. 5.4 shows the spatial distribution of residual NAPL blobs in water-wet and neutral-wet porous media. Different colors represent the individual NAPL blobs. In order to better show the distribution of residual phases in the pore space, solid particles (grey) were also shown. In the water-wet system, residual NAPL prefers to reside at the center of large pore bodies as disconnected volumes. These blobs range greatly in both in size and shape from simple singlets which occupy single pore bodies to complex ganglia that extend in length to occupy multiple pore-bodies. However, both the entrapped blobs can be found in small and large pores in the neutral-wet system. The shape of entrapped blobs was more complicated which strongly related the local pore geometry. The difference in pore occupation results in a more uniform distribution of NAPL blobs in neutral-wet medium.

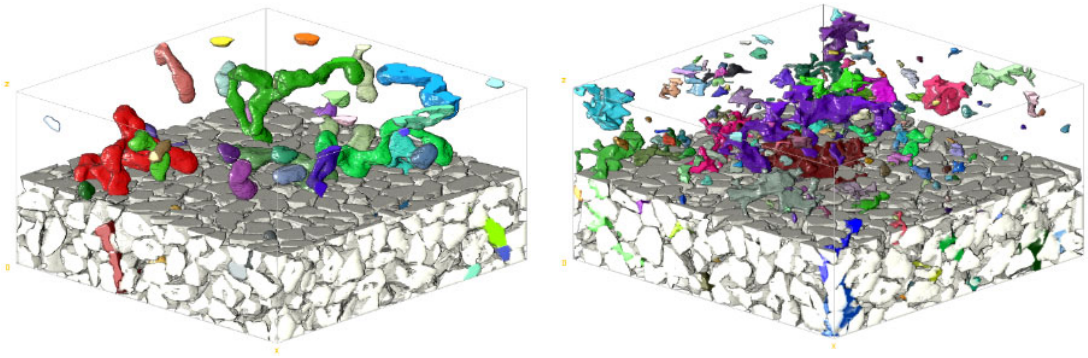

(a) (b)

Figure 5.4. Schematics of residual NAPL blobs in (a) water-wet and (b) neutral-wet porous media.

After water flooding, the residual saturations in pore sapce are similar for water-wet (S_n = 9.4%) and neutral-wet porous media (S_n = 9.5%). The total blobs number in the neutral-wet medium (number = 1402) is greater than that in the water-wet medium (number = 705) at a similar residual saturation. Fig. 5.5 show that the NAPL blobs size distribution and cumulative volume fraction for the two porous media. Although the residual saturation was similar, a significant difference in size distribution between water-wet and neutral-wet systems were observed. For the small blobs (< 300 μm^3), the number in the neutral-wet system is considerable larger than that in the water-wet system. Although the number of large blobs (> 900 μm^3) is small in both systems, their contribution to the total volume is relatively large. Fig. 5.5(b) shows that the volume of large blobs (> 900 μm^3) accounts for 30.24% in the water-wet system and 9.45% in the neutral-wet system. It indicates that the average size of NAPL blobs in the water-wet system is larger than in the neutral-wet system. The uniform spatial distribution is conducive to NAPL blobs mass transfer with freshwater more effectively.

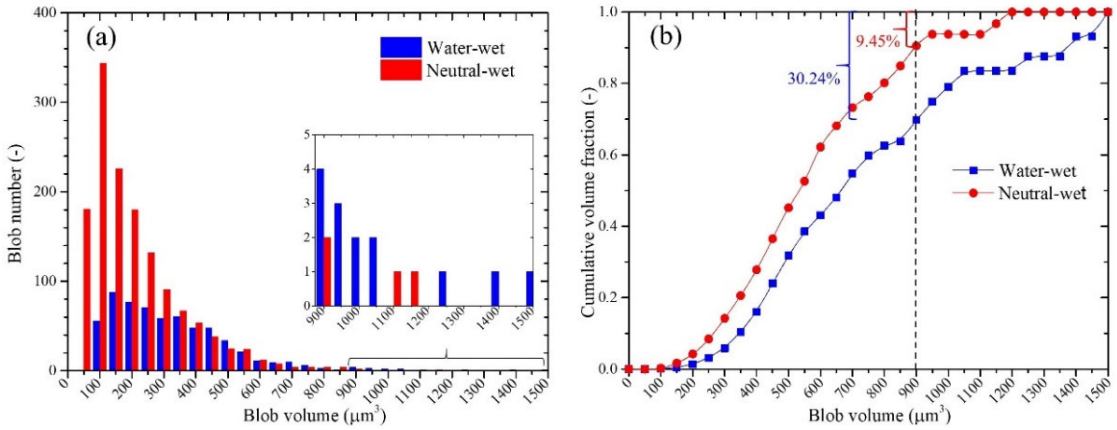

(a) (b)

Figure 5.5. NAPL blobs (a) size distribution and (b) cumulative volume fraction in water-wet and neutral-wet porous media.

5.4 Visualization of residual NAPL dissolution process

To further investigate how those different characteristics of residual NAPL blobs affect the dissolution and mass transfer processes, DDI water was continue injected upward using a piston pump. In this study, five flow rates were set at q = 0.3, 0.5, 1.0, 2.0, and 4.0 ml/min with corresponding Reynolds number Re = 0.033, 0.057, 0.109, 0.219, and 0.438, respectively. The column was then periodically scanned to monitor the progressive dissolution process.

Fig. 5.6 shows the time-resolved images of residual NAPL in water-wet and neutral-wet porous media at q = 0.5 ml/min. T is the dissolution time during the freshwater flushing. As the flushing proceeds, the residual saturation and size of the entrapped NAPL blobs decrease gradually. Obviously, the dissolution of NAPL in neutral-wet medium is faster than that in water-wet medium. Although, the residual saturation decreased with dissolution time, the number remained almost stable. Unlike the gas dissolution in porous media, the remaining small NAPL blobs cannot be completely dissolved. This may be due to the insoluble dopants (iododecane) or tailing effects in liuqid-liquid (Johnson et al., 2003).

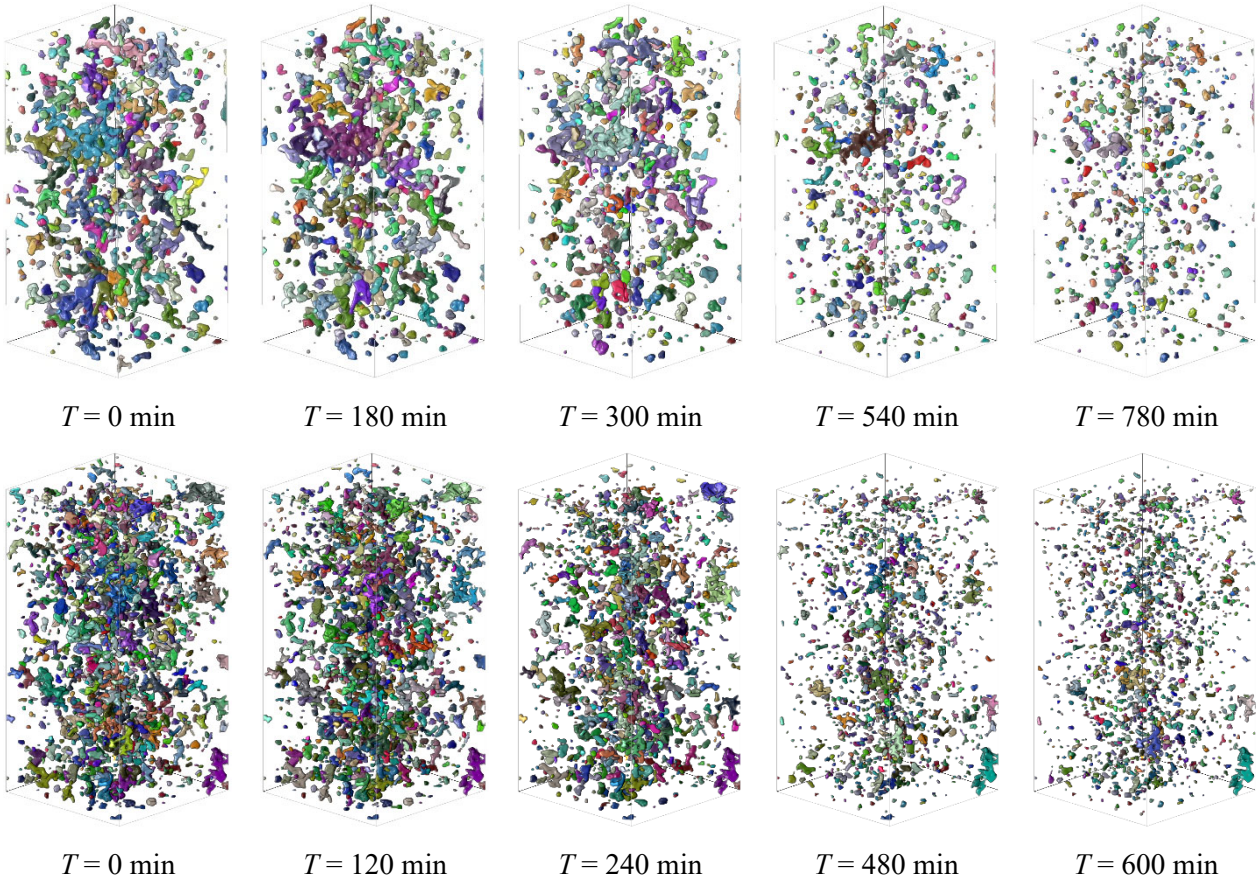

Figure 5.6. Progressive distribution of residual NAPL blobs during dissolution in (a) water-wet and (b) neutral-wet porous media at q = 0.5 ml/min

For a traget blob, the dynamic dissolution during water flushing was nonlinear and affected by its morphology and local pore structure. When a narrower part of multi-pore ganglia (i.e., throat) dissolves faster than the other interfaces, the larger structure may break down into smaller blobs, as shown in Fig. 5.7. Similar snap-off behavior has also been observed in previous CO_2 and NAPL dissolution experiments (Patmonoaji and Suekane, 2017; Schnaar

and Brusseau, 2006). A specific behaviro was first obsered that a well-connected ring breaks up while no new blob is generated. It is more common that the interface recedes from the NAPL-bulk water interface and gradually decreased in size without breaking.

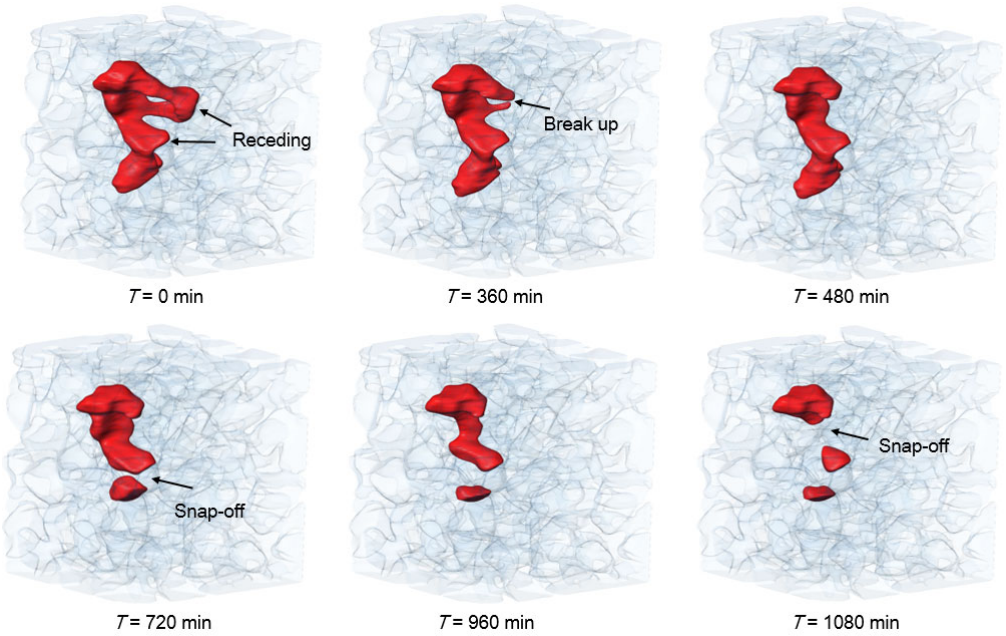

Figure 5.7. The dynamic dissolution process of a traget NAPL blob at q = 0.3 ml/min in water-wet porous medium, including interface receding, break up and snap-off.

The saturations of residual NAPL as a function of dissolution time in water-wet and neutral-wet porous media are presented in Fig. 8 for five water flow rates. At the capillary force dominant region, the initial residual saturation for all experiments range between 8.9% and 11.0%. These values are similar to the residual saturation reported in other unconsolidated porous media (Al-Raoush, 2014; Hu et al., 2020). Once the freshwater was introduced into the column, the active mass transfer occurred between residual phases and flowing water, as evidenced by a decrease in NAPL saturation. A significantly slower rate of dissolution for low water flow rates. The maximal capillary number at the largest flow rate of q = 4 ml/min is about 2.1×10^{-5} which is smaller than the critical value of remobilization, 10^{-3} (Morrow et al., 1988). Therefore, the major decrease in residual saturation is believed to be due to dissolution.

As shown in Fig, 5.8, the residual saturation dropped rapidly at the beginning of the dissolution process and then a leveling off of the rate of change in saturation was observed. The main

reason can be explained by the evolution of the interfacial area between residual NAPL and flowing water. The specific interfacial area decreased rapidly as the NAPL saturation decreased during the progressive dissolution. At the beginning of the dissolution process, large NAPL blobs exposed to flowing water shrink much faster. Slower dissolution occurred at later stage when the residual saturation is lower. In addition, the interfacial area available for mass transfer is that not all NAPL blobs are equally exposed to flowing water. At the later stage, the remaining blobs are mainly those in small pores or crevices that may be shielded by other blobs or particles. The less chance exposes to flowing water means a slower dissolution rate. The pore scale configuration of NAPL blobs may help to explain tailing effects, a leveling off of the rate of change in residual saturation at small saturation.

Figs. 5.8 show that the reduction rate of residual saturation is higher in neutral-wet system than in water-wet porous system. As described in Chapter 5.3, the morphology of residual phase was strongly related to the wettability of solid surface. Tailing effect was obvious in the neutral-wet system, especially at the low flow rate conditions. A large number of NAPL blobs were entrapped in the small pores or crevices and were less change to be exposed to flowing water. Bradford et al. (1999) suggested that the concentration-tailing region is particularly marked in porous media containing fractional NAPL-wet particles.

The specific interfacial area has been recognized as a major parameter in both the entrapment and remediation of NAPLs in porous media. Visualization technology provides the possibility to directly measure the surface area of entrapped phase in opaque porous media. For an individual blob, the interfacial area consists of the capillary-associated interfacial area between NAPL and bulk water, and film-associated interfacial area between NAPL and wetting fluid film. There is still extensive debate about which area is more reasonable for calculating the mass transfer coefficient. Therefore, total or capillary interfacial area was regarded as the major parameter to calculate the mass transfer coefficient. The specific interfacial areas (total or capillary) are obtained by normalizing interfacial area with the volume of the representative elementary volume. During the dissolution progress, the reduction of NAPL saturation was accompanied by a reduction in the specific interfacial area decreases. The decrease rates are faster in neutral-wet system than in the water-wet system. As shown in Figs. 5.9, the curve shapes of residual saturation and specific interfacial area as a function of dissolution are

similar. The decrease in a specific total interfacial area correlates well with the decrease in residual saturation.

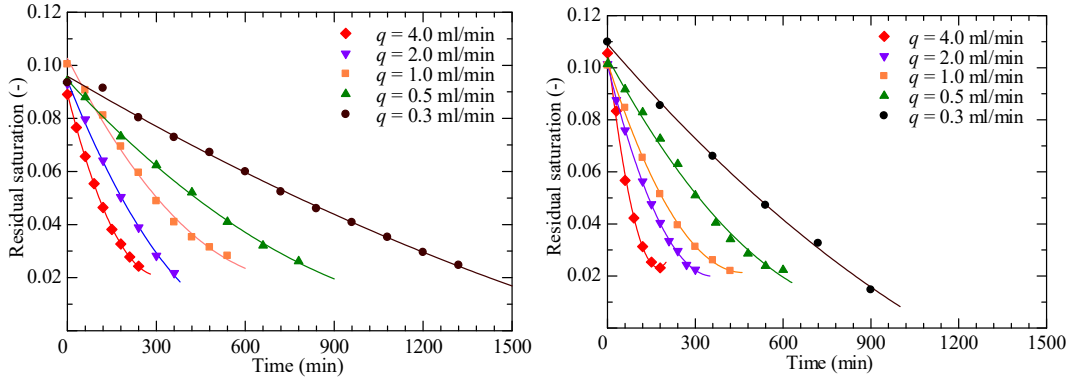

Figure 5.8. Residual NAPL saturation versus time in (a) water-wet and (b) neutral-wet porous media at all flow rate conditions.

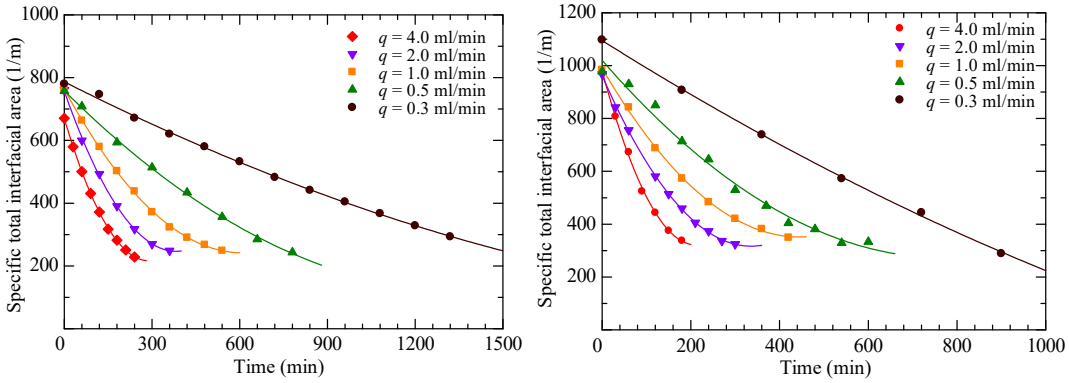

Figure 5.9. Specific total interfacial area versus time in (a) water-wet and (b) neutral-wet porous media at all flow rate conditions.

The specific total and capillary interfacial areas as a function of NAPL saturation for all experiments are presented in Fig. 5.10. These two kinds of specific interfacial area present linearly relationship with residual saturation in water-wet and neutral-wet porous media. Two prediction models have been proposed to fit the experimental data of a_t and S_n: $a_t = c_0 \cdot S_n$ in water-wet systems and $a_t = c_1 \cdot S_n + c_2$ in neutral-wet system, where c_0, c_1 and c_2 are arbitrary constants. The specific total interfacial area is proportional to NAPL saturation, which is consistent with previous observation reported in water-wet porous media. (Chomsurin and Werth, 2003; Schnaar and Brusseau, 2006). The different forms of the fitting formula may be

due to the different morphology and size distribution in water-wet and neutral-wet porous media.

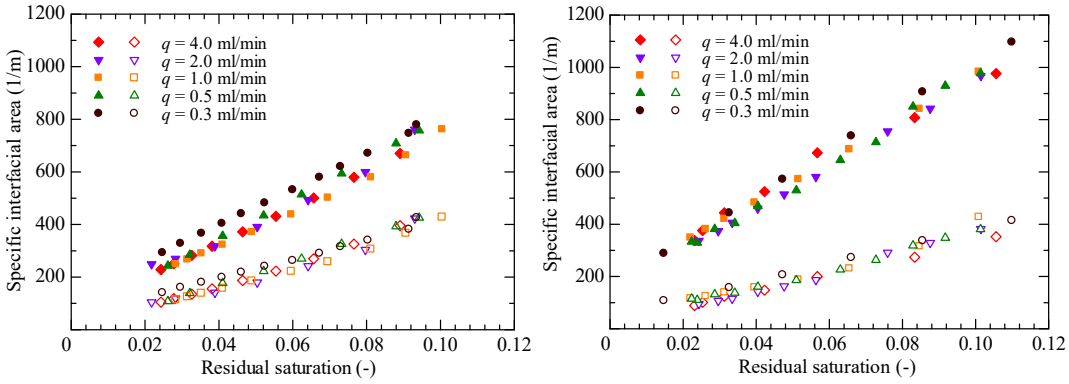

Figure 5.10. Specific capillary interfacial area (hollow dots) and total interfacial area (solid dots) versus residual saturation in (a) water-wet and (b) neutral-wet porous media at all flow rate conditions.

The value of the specific total interfacial area in neutral-wet porous media are higher than in water-wet porous media, whereas the specific capillary interfacial areas are close at the same residual saturation. The ratios of capillary to total interfacial area decreased from 0.59 to 0.42 and 0.39 to 0.26 in water-wet and neutral-wet porous media, respectively. The lower ratio in neural-wet porous media results arises from the higher occupation frequency of residual blobs in small pores. In water-wet unconsolidated porous media, the value of ratio ranged from 0.50 in quartz sand (Al-Raoush, 2014) to 0.67 in plastic particles (Hu et al., 2020). The value is affected by many factors in unconsolidated porous media, such as sand size, shape, roundness, wettability, and the established flow condition. In the water-wet porous media, with the multi-pore blobs break into a smaller singlet, the ratio presents an increased tendency, which is contrary to previous study (Schnaar and Brusseau, 2006). In this study, the remaining small NAPL blobs resided in small crevices and have less chance of contacting flowing water.

5.5 Mass transfer coefficients

According to the Eq. (4-2), the solute concentration at the outlet is necessary for calculating the mass transfer coefficient. An indirect method has been developed to determine the concentration based on the difference of images. The NAPL mass in the target region remains

balanced, which means that the amount released from the blobs into the water is equal to the amount of freshwater water carried out. Because the concentration of NAPL near the inlet is close to zero, the effluent concentration was then calculated using Eq. (4-3).

$$C_{x=L} = -\frac{\rho\varepsilon}{v}\frac{\Delta S}{\Delta t}L \quad (5\text{-}1)$$

where v is the velocity of water, and L is the length of the observation region. The indirect method has been validated by comparing the effluent concentration obtained from direct method using gas chromatography (Schnaar and Brusseau, 2006).

Fig. 5.11 shows the normalized concentration profiles C/C_s calculated by the slice in the water-wet porous media at q = 4.0 ml/min. The values of C/C_s near the oultlet are 0.07 at T = 30 min, then decreased to 0.04 at T = 150 min and 0.02 at T = 240 min in a water-wet porous medium. The decrease in concentration is mainly due to the reduction of dissolution rate. The obtained value of $C_{x=L}/C_s$ was used to calculate the mass transfer coefficient.

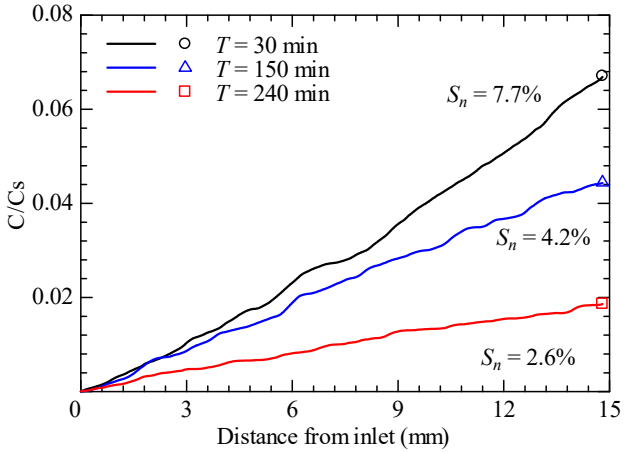

Figure 5.11. Normalized concentrations calculated in water-wet porous medium at q = 4.0 ml/min. Concentrations at three moments were selected corresponding three different residual saturation.

By combining Eqs. (4-2) and (4-3), the steady state 1D mass balance equation can also expressed as follow:

$$v\frac{dC}{dx} = -ka(C - C_s). \quad (5\text{-}2)$$

When fresh water was flushed into an initially contaminated column at equilibrium, the solute concentration at the inlet was regarded as zero. Thus, by solving differential equations Eq. (5-2), the mass transfer coefficient k can be expressed as follows:

$$k = -\left(\frac{v}{La}\right)\ln\left(1 - \frac{C_{x=L}}{C_s}\right). \quad (5\text{-}3)$$

According to Eqs. (4-5) and (4-6), the overall lumped mass transfer coefficient *ka* and mass transfer coefficient *k* were then calculated in water-wet and neutral-wet porous media. The lumped mass transfer coefficient and mass transfer coefficient were usually normalized with characteristic length and molecular diffusion, expressed in terms of the modified Sherwood number *Sh*' and Sherwood number *Sh*, respectively. Figs. 5.12 and 5.13 show the values of *Sh*' and Sh_t versus residual saturation in water-wet and neutral-wet porous media. In Figs. 5.12(a) and 13(a), values of *Sh*' generally decrease with decreasing S_n, which show a well agreement with the previous studies (Chomsurin and Werth, 2003; Imhoff et al., 1994; Miller et al., 1990; Powers et al., 1992). Values of Sh_t are relatively constant for each experiment during most dissolution time, except when $S_n < 3.0\%$ in neutral-wet porous media. As discussed in Chapter 5.4, the tailing effect was significant in neutral-wet system especially at low S_n. In addition, the small blobs also bring a relatively large deviation on the surface area measurement. The value of surface area for small blobs might be overestimated especially in neutral-wet porous media, which means an underestimate the value of Sh_t. As shown in Fig. 12(b), many experimental data present extremely low values, when S_n close to 3%. Thus, we discarded these data with S_n less than 3.0% in the subsequent discussion. The values of *Sh'* and Sh_t are significantly affected by the flow conditions, and a higher flow rate indicates a higher mass transfer rate.

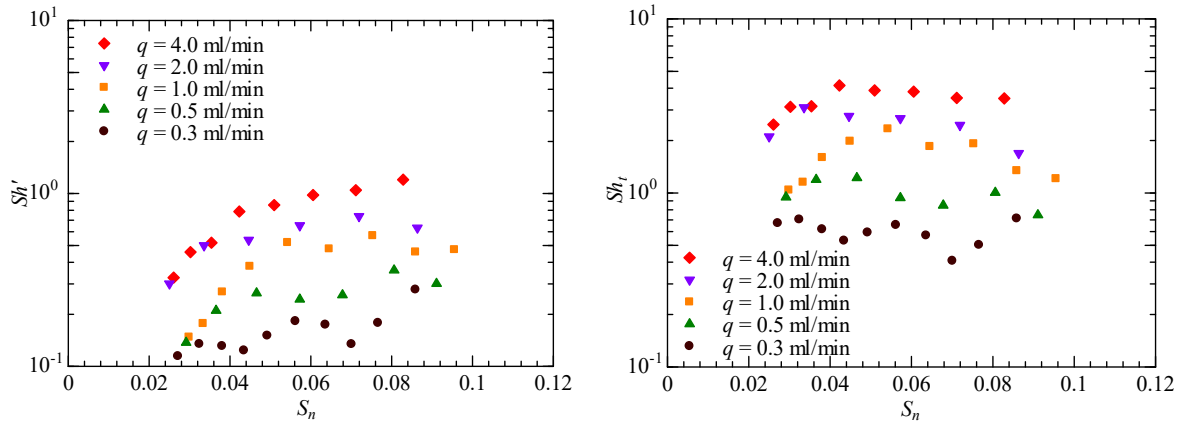

Figure 5.12. Modified Sherwood number and Sherwood number in water-wet porous media at all flow conditions.

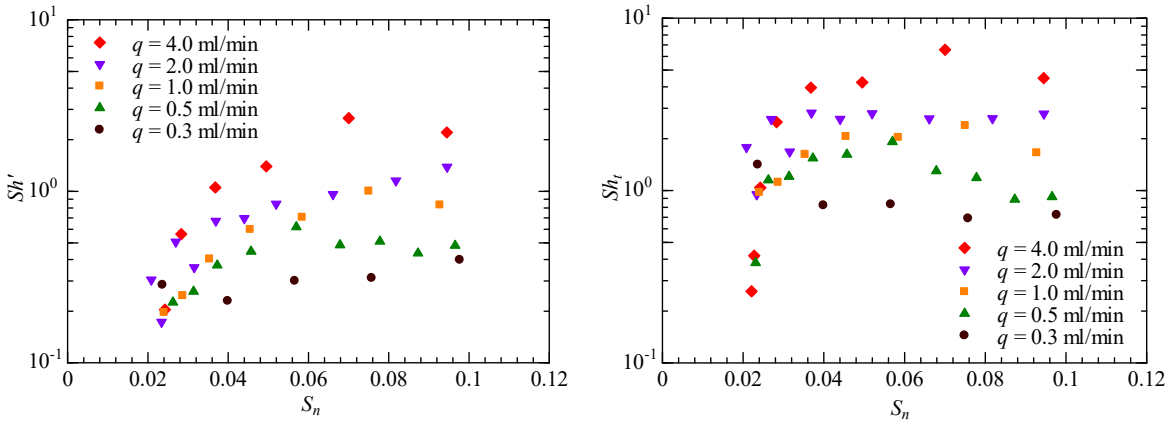

Figure 5.13. Modified Sherwood number and Sherwood number versus Reynolds number in neutral-wet porous media.

5.6 Comparison with literatures

There is still extensive debate about which area is more reasonable for calculating the mass transfer coefficient. The capillary interfacial area refers to the part exposed to bulk water, while many findings revealed the existence of water film between NAPL and solid. The thin water film also facilities the pore-scale events in porous media, such as capillary trapping and dissolution. The thin water film coating the solid particles has been directly observed using fluorescence microscopy (Grate et al., 2010). Kazemifar et al. (2016) quantified the flow dynamic of supercritical CO_2-water displacement in a 2D micromodel using micro-PIV and fluorescence microscopy. The raw micro-PIV video showed the motion of the tracer particles within the water films coating the solid pillars. In this study, limited by the image resolution, it is insufficient to detect the water film. We conducted a scanning electron microscopy image of silica sand, as shown in Fig. 5.1. From the figure, it can be found that silica sand has a rough surface, and the roughness is much smaller than the X-ray image resolution. We believed that a thin water film exits between the NAPL blobs and sand particles. The mass transfer between NAPL and water occurs in both capillary interfacial area and thin film, while the mass transfer extensive should be different.

In order to directly compare with literatures, two kinds of mass transfer coefficients, k_t and k_c were derived from the total and capillary interfacial area, corresponding to two Sherwood numbers, Sh_t and Sh_c. Chomsurin and Werth, 2003 used the Peclet number ($Pe = Re{\cdot}Sc$) to represent the flow condition. When only one kind of NAPL was studied, Reynolds number

was often selected to represent the flow condition. Fig. 5.14 plotted the average values of Sh_t and Sh_c during the dissolution processes at a fixed flow rate. When considering the total interfacial area as the main region for liquid-liquid mass transfer, the wettability has a slight effect on the mass transfer coefficient. The flow rate and magnitude of the total infacial area are the two main parameters in controlling the dissolution rate of residual NAPL in flowing water. At the same flow condition, the value of Sh_t in neutral-wet system is about an average of 1.1 times that in water-wet system.

When treating the capillary interfacial area as the main region for NAPL-water mass transfer, the wettability shows a significant effect on the mass transfer coefficient. The average value of Sh_c in the neutral-wet system is about 1.8 times that in the water-wet system. The difference in Sherwood number is due to the spatial distribution and configuration of residual NAPL blobs in porous media. In the neutral-wet porous media, the number of blobs is larger; the distribution is more uniformly residing in small and large pores. Thus, the NAPL blobs have a higher chance to expose fresh water in neutral-wet porous media.

The relationship between Sh (i.e. Sh_t and Sh_c) and Re follows a power-function $Sh \sim Re^n$, where n is an arbitrary constant. To estimate the influence of flow conditions on the mass transfer coefficient, all experimental data shown in Fig. 13 were fitted as follow:

In water-wet porous media,

$$Sh_t = 6.94Re^{0.69} \quad (5\text{-}4)$$

$$Sh_c = 14.85Re^{0.74} \quad (5\text{-}5)$$

In neutral-wet porous media,

$$Sh_t = 7.90Re^{0.66} \quad (5\text{-}6)$$

$$Sh_c = 26.85Re^{0.72} \quad (5\text{-}7)$$

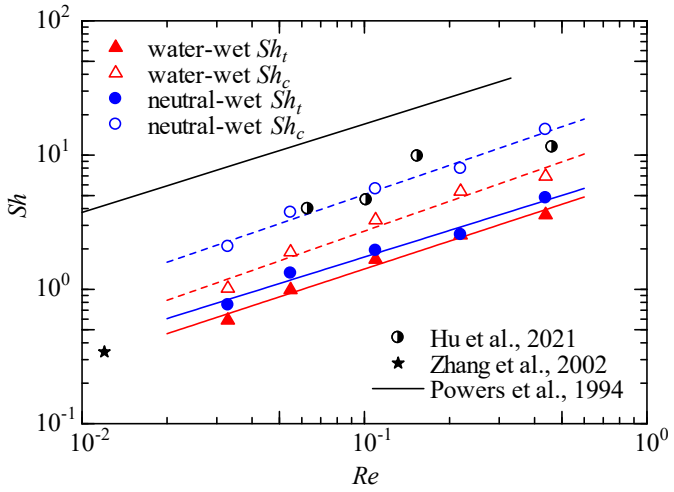

Figure 5.14. Sherwood number versus Reynolds number in water-wet and neutral-wet porous media. A comparison of Sherwood number in water-wet silica gel (Zhang et al., 2002) and sand (Powers et al., 1994), and in neutral-wet glass beads packing (Hu et al., 2021).

In Fig. 5.15, experimental data, the empirical models and previous literature's result are compared at range of *Re*. In The corresponding residual saturation range is between 3.0% and 10.6%. The value of *n* various only in a small range for all experimental conditions, from 0.66 to 0.74. The obtained value of *n* is also fell in the range obtained in the previous 3D dissolution experiments, 0.56 in Hu et al. (2021); 0.61 in Powers et al. (1992); 0.65 in Patmonoaji and Suekane (2017); 0.71 in Imhoff et al. (1994) and 0.75 in Miller et al. (1990). Various dissolution experiments have measured the Sherwood number calculating using the capillary or total interfacial area. Zhang et al. (2002) obtained that the values of Sh_t mostly fall in the range of 0.1 to 0.7 at $Re = 0.01$ in a water-wet 425-500 μm silica gel packing. The average values approximately 0.34 agree well with the prediction value 0.47 using Eq. (5-4). Hu et al. (2021) obtained the value of Sh_c ranges from 4.0 to 11.5 at $Re = 0.063$ to 0.462 in neutral-wet glass beads packing. The corresponding predicted values are 3.7 to 15.4 using Eq. (5-7), which shows a reasonable agreement with the experimental data. Notedly, in that study, they used Re/ε to represent the flow condition. For direct comparison, we unified the definition of Reynolds number. Powers et al. (1994) conducted the dissolution of naphthalene to water, and summarized an empirical correlation as $Sh_t = 77.6Re^{0.658}$. In the range of *Re* of this study ($Re = 0.03$~0.44), the value of Sh_t predicted by the Powers equation increase from 7.7 to 45.2, which is almost seven times the values obtained in this study. The difference in Sherwood

numbers may be due to the different dissolution mechanisms between liquid-liquid and solid-liquid systems.

Various researchers have established empirical correlations between Sh' and S_n, ε and Re in a power-law form. Some empirical correlations sometimes consider the influence of Schmidt number, which defined as the ratio of momentum diffusivity and mass diffusivity. In this study, we did not take Schmidt number into consideration, since the value of Sc is constant. Residual saturation and medium porosity were usually combined into a single variable, volumetric fraction ($\theta_n = \varepsilon S_n$). The simplified form was used to fit all experimental data as $Sh' = aRe^b\theta_n^c$, where a, b and c are the arbitrary constant. The stepwise least squares regression was widely used to find the optimum combination of parameters. Although this method can obtain a minimized deviation between the experimental data and the predicted value, it may lack physical interpretation. We developed a novel method to obtain the fitting parameters based on the pore-scale characteristics of the residual phase. For NAPL dissolution experiment in a water-wet medium, the values of d_{50} and D_m remain constant; thus, $Sh' \sim ka$. As shown in Fig. 5.11, the specific surface area is proportional (or nearly linear) to the residual saturation, $a \sim S_n$ or $a \sim \theta_n$. The influence of the Reynolds number on the mass transfer coefficient presents a power-law form, with an exponent of about 0.7, i.e., $k \sim Re^{0.7}$. Thus, the simplified empirical correlation of Sh' was yielded as $Sh' = aRe^{0.7}\theta_n$. A linear regression analysis was performed on the experimental data, as shown in Fig. 5.15. The models yielding the best fit in the power-law form are:

in water-wet porous media,

$$Sh' = 67.22Re^{0.7}\theta_n \quad (5\text{-}8)$$

in neutral-wet porous media,

$$Sh' = 114.24Re^{0.7}\theta_n \quad (5\text{-}9)$$

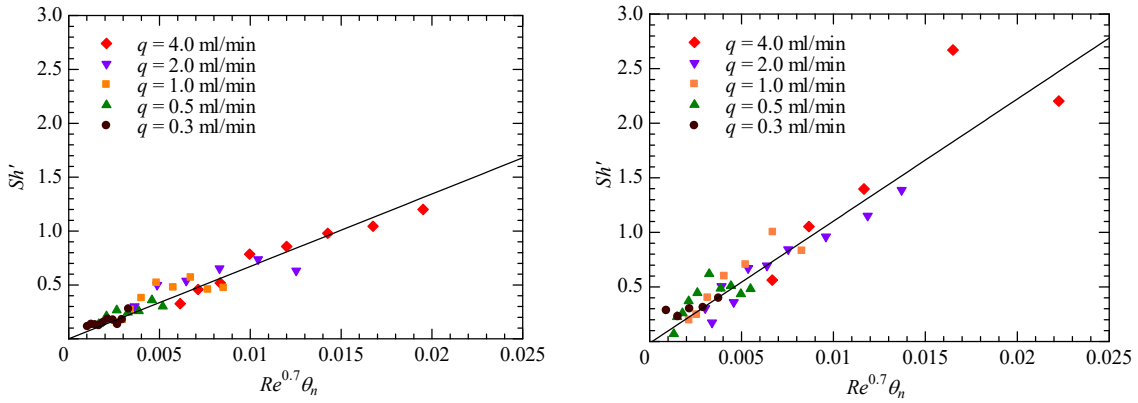

Figure 5.15. Modified Sherwood number versus Reynolds number and volume fraction in water-wet (a) and neutral-wet (b) porous media.

5.7 Summary

The results showed that the wettability of pore surfaces has a significant impact on the pore-scale morphology of residual NAPL; thus, affecting the dissolution behavior in natural porous media. Our main conclusions are summarized as follows:

The residual NAPL blobs are mainly trapped in the central of larger pore bodies in water-wet system, whereas in neutral-wet system, they can be found in large and small pores. The total interfacial area in neutral-wet media is higher than in water-wet porous media, whereas the capillary interfacial area is similar for the two media at the same saturation.

Under the same flow condition, the average value of Sh_t in the neutral-wet media is about 1.1 times that in the water-wet media. It indicates that when the total surface area is regarded as the active region for mass transfer, wettability has a slight effect on the mass transfer coefficient in porous media. The average value of Sh_c in the neutral-wet porous media is about 1.8 times that in the water-wet porous media. The reason may be that blobs are more evenly distributed in the neutral-wet porous media, allowing the capillary interfacial area efficiently exposed to freshwater.

Several empirical correlations with the power-law form were proposed to predict the Sherwood number and modified Sherwood number under various flow conditions. The mass transfer coefficient was independent of the residual saturation, and the Sherwood number was summarized $Sh \sim Re^n$ as in previous studies. The results showed that the wettability has little

effect on the exponent value, which ranges from 0.66 to 0.74 in water-wet and neutral-wet systems. Based on the pore-scale characteristics of residual NAPL, the empirical correlations of *Sh'* were yielded as $Sh' = 67.22Re^{0.7}\theta_n$ in water-wet media, and $Sh' = 114.24Re^{0.7}\theta_n$ in neutral-wet media.

The results described in this chapter have been published as: **Y. Hu**, Y. She, C. Zhang, A. Patmonoaji*, S. Matsushita, T. Suekane, Pore-scale investigation of wettability impact on residual nonaqueous phase liquid dissolution in natural porous media, *Sci. Total Environ*. (2021).

Chapter 6. Conclusion and future work

6.1 Conclusion

In this work, we explored the behavior of immiscible liquids in porous media to mimic the flow and transport of NAPL or CO_2 in the subsurface. The pore-scale characterizations of the non-wetting phase were determined by using an X-ray microtomography. Three typical processes involved in soil and groundwater remediation, and CO_2 geological sequestration were investigated, namely drainage displacement, imbibition displacement (also known as capillary trapping) and dissolution. Various impact factors affecting these processes in porous media were discussed, such as pore structures, surface wettability, flow conditions and fluid properties. The obtained results may reveal the underlying mechanism and provide benchmark data for large-scale modeling in the practical applications.

Chapter 2, we studied the impacts of viscous and capillary forces on the drainage displacement in 3D porous media with a wide range of capillary number *Ca* and viscosity ratio *M*. The displacement patterns are controlled by the balance of viscous force and capillary force, and manifest as viscous fingering, capillary fingering, and stable displacement. The pore-scale characterizations of the non-wetting phase were analyzed, including saturation, finger width and fractal dimension, a phase diagram (*Ca*-*M*) was then proposed to predict the different displacement patterns in 3D porous media. Compared with the results obtained from the 2D micromodel (Zhang et al., 2010), the transition zone in 3D porous media is wider. The reason may be that the structural dimensional, pore size distribution and coordination number in 3D porous media are more likely to cause to mixed displacement patterns.

Chapter 3, we determined the effect of capillary number on the pore-scale morphology of residual phase in capillary trapping. The capillary desaturation curves were conducted with two injection strategies to increase the flow rate, namely progressively increase and individually increase. The results show that the individually increase has a lower critical *Ca* which reflect that the well-connected cluster is easily being mobilized. The *Ca* has a significant influence on the size distribution of residual phase. At high *Ca*, the viscous forces dominate the capillary trapping, resulting in smaller bubbles, and the percolation theory was invalid. In addition, the interfacial area of the trapped bubbles at various flow rate exhibits some universal

characterizations, such as $A_b - V_b$, $a_t - S_n$ and $a_i - S_n$. The effect of particle size on the intrinsic interfacial area a_i and specific interfacial area a_t can be normalized through multiplication by d_{50}.

Chapter 4, the effect of pore structure on dissolution process was investigated. The direct observation indicates that not all blobs are equal to contact with flowing water. The preference flow path play an important role on the dissolution rate. The mass transfer process was considerably dependent on the Reynolds number, and a higher flow rate indicates a higher mass transfer coefficient. Further, two empirical models describing the relation between the Sherwood number and Reynolds number were generated in the 2D micromodel and 3D packed bed. The overall mass transfer coefficient was higher in the packed bed compared with that in the micromodel under the Darcy flow conditions. The difference between mass transfer coefficients of micromodel and packed bed can be primarily attributed to the inherent pore connectivity and coordination number of pore structures.

Chapter 5, the effect of wettability on dissolution process in natural porous media was investigated. The pore occupation and interfacial area of the trapped NAPL blobs are significant different in water-wet and neutral-wet porous media. In the neutral-wet system, NAPL was trapped in small pores and has a higher interfacial area. In addition, the value of *Sh'* in the neutral-wet media is greater than that in the water-wet media under the same flow conditions. However, the average value of Sh_t in the neutral-wet media is about 1.1 times that in the water-wet media, which indicates that wettability has a slight effect on the mass transfer coefficient in porous media. Several empirical correlations with the power-law form were proposed to predict the Sherwood number and modified Sherwood number under various fluid flow and surface wettability conditions.

6.2 Future work

The main contribution of this work is to provide the pore-scale information of multiphase flow in porous media using X-ray imaging methods, with the aim of better understanding of CO_2 geological sequestration, soil and groundwater remediation. Furthermore, the results are also can be applied to many other fields of research, such as polymer electrolyte fuel cell and oil

and gas exploration from reservoirs. Thus, in the future, many research works deserve to be extended for practical applications.

(1) In this work, artificial porous media produced by discrete particles are used to mimic underground rock and soil. All experiments were conducted at normal temperature and ambition pressure. In geological sequestration, CO_2 is injected into the storage site where the depths are usually higher than 800m, and the CO_2 reaches the supercritical state. The physical properties between the supercritical state and the gas state are significantly different, and some different phenomena may appear in the multiphase flow. Under different storage sites, the state between injected CO_2 and remaining oil can present from immiscible, near miscible to miscible. Thus, it is necessary to identify the displacement patterns at a representation of reservoir conditions. In Chapter 2 and Sin et al. (2019), we have investigated the viscous fingering at immiscible and miscible fluids at normal temperature and ambition pressure, respectively. Future work can be conducted under specific pressure and temperature to obtain different states of CO_2, and then to observe the viscous fingering under different miscible states. Moreover, the dissolution behavior of residual CO_2 in different phases is also worth studying to gain insight into the solubility trapping in CCS.

(2) Lab-based microtomography with minutes of acquirement time can only capture static and quasi-static multiphase flow phenomena in porous media. In Chapter 3, the static characterizations of the residual phase with a wide range of flow rates were visualized and quantified. Recently, high-speed synchrotron X-ray CT can capture 3D images within seconds, providing an effective method for exploring the more fundamental and detailed physical phenomenon. Singh et al. (2017) determined the dynamics of snap-off and pore-filling events in 3D media at a very low flow rate. The frequency of these two events decides the residual phase saturation. It is necessary to determine the competition between snap-off and pore-filling events at a high flow rate. In addition, with the increase of *Ca*, the pore-scale physics underlying the phenomenon of the mobilization of oil blobs remains intensely debated. Some researcher suggested that the largest cluster firstly break up into smaller droplets and then was removed from pore space. By contrast, other results indicated that the largest cluster beyond a threshold size would be removed without break up. With the aid of high-speed synchrotron X-ray CT, direct observation of the mobilization of oil clusters in highly disordered 3D porous media will provide a clear conclusion for this debate.

(3) In this work, only a kind of NAPLs was used to study the dissolution process in porous media and the corresponding mass transfer coefficient. The proposed empirical correlations for *Sh'* only include the Reynolds number, which does not consider the influence of NAPLs' physical properties. In soil and groundwater remediation, a variety of contaminants with different properties will be encountered. Thus, in order to expand the scope of the application of proposed correlations, different NAPLs need to be investigated. The typical impact factors including the solubility, molecular diffusion coefficient, and viscosity, which can be represented with Schmidt number *Sc* and Prandtl number *Pr*. In practical applications, the contaminant source is usually a mixture of multi-components. Aqueous concentrations of each component from the mixture are expected to be less than their pure component solubility, with an effective solubility that decreases with decreasing mole fraction in the trapped phase(Geller and Hunt, 1993). More attention should be paid to the multicomponent phase dissolution process and the mass transfer coefficient.

(4) At the underground, the fluctuation of water level will change the spatial distribution of NAPL and air and surrounding water. Under different groundwater levels, the morphology of NAPL sources may present as residual, free, and occluded in pore space and the NAPL morphology strongly controls mass transfer. The pilot-scale experiment within a 2D sand-packed flow tank has been conducted to study the impact of water table fluctuations on the mass transfer between NAPL-water-air in the vadose zone (Joun et al., 2016; Petri et al., 2015). The pore-scale characterizations of three phases and the local mass transfer coefficients will provide new insight into the complex behavior in the vadose zone. The presented characterization method of the residual phase in Chapter 3 and the mass transfer calculation method in Chapters 4 and 5 will benefit the related research. In the future, the pore-scale study can provide an insight into the underlying mechanism and the benchmark data for large-scale modeling.

References

Agaoglu, B., Copty, N.K., Scheytt, T., Hinkelmann, R., 2015. Interphase mass transfer between fluids in subsurface formations: A review. Adv. Water Resour. 79, 162–194. https://doi.org/10.1016/j.advwatres.2015.02.009

Agaoglu, B., Scheytt, T., Copty, N.K., 2016. Impact of NAPL architecture on interphase mass transfer: A pore network study. Adv. Water Resour. 95, 138–151. https://doi.org/10.1016/j.advwatres.2015.11.012

AIP, 2003. Answers to frequently asked questions about managing risk at LNAPL sites. API Soil Groundw. Res. Bull. 1–20.

Al-Raoush, R.I., 2014. Experimental investigation of the influence of grain geometry on residual NAPL using synchrotron microtomography. J. Contam. Hydrol. 159, 1–10. https://doi.org/10.1016/j.jconhyd.2014.01.008

Al-Raoush, R.I., 2009. Impact of wettability on pore-scale characteristics of residual nonaqueous phase liquids. Environ. Sci. Technol. 43, 4796–4801. https://doi.org/10.1021/es802566s

Aminnaji, M., Rabbani, A., J. Niasar, V., Babaei, M., 2019. Effects of Pore-Scale Heterogeneity on Macroscopic NAPL Dissolution Efficiency: A Two-Scale Numerical Simulation Study. Water Resour. Res. 55, 8779–8799. https://doi.org/10.1029/2019WR026035

Anbari, A., Chien, H.T., Datta, S.S., Deng, W., Weitz, D.A., Fan, J., 2018. Microfluidic Model Porous Media: Fabrication and Applications. Small. 14, 1703575. https://doi.org/10.1002/smll.201703575

Andrew, M., Bijeljic, B., Blunt, M.J., 2014. Pore-scale contact angle measurements at reservoir conditions using X-ray microtomography. Adv. Water Resour. 68, 24–31. https://doi.org/10.1016/j.advwatres.2014.02.014

Andrew, M.G., 2014. Reservoir-Condition Pore-Scale Imaging of Multiphase Flow. PhD thesis, Imp. Coll. London. Imperial College London.

Armstrong, R.T., Evseev, N., Koroteev, D., Berg, S., 2015. Modeling the velocity field during Haines jumps in porous media. Adv. Water Resour. 77, 57–68. https://doi.org/10.1016/j.advwatres.2015.01.008

Armstrong, R.T., Georgiadis, A., Ott, H., Klemin, D., Berg, S., 2014. Critical capillary number: Desaturation studied with fast X-ray computed microtomography. Geophys. Res. Lett. 41, 55–60. https://doi.org/10.1002/2013GL058075

Bahar, T., Golfier, F., Oltéan, C., Lefevre, E., Lorgeoux, C., 2018. Comparison of theory and experiment for NAPL dissolution in porous media. J. Contam. Hydrol. 211, 49–64. https://doi.org/10.1016/j.jconhyd.2018.03.004

Bakhshian, S., Hosseini, S.A., 2019. Pore–scale analysis of supercritical CO_2–brine immiscible displacement under fractional–wettability conditions. Adv. Water Resour. 126, 96–107. https://doi.org/10.1016/j.advwatres.2019.02.008

Bakhshian, S., Hosseini, S.A., Shokri, N., 2019. Pore-scale characteristics of multiphase flow in heterogeneous porous media using the lattice Boltzmann method. Sci. Rep. 9, 1–13. https://doi.org/10.1038/s41598-019-39741-x

Barca, F., Caporossi, T., Rizzo, S., 2014. Silicone oil: Different physical proprieties and clinical applications. Biomed Res. Int. 2014, 502143. https://doi.org/10.1155/2014/502143

Berg, S., Ott, H., Klapp, S.A., Schwing, A., Neiteler, R., Brussee, N., Makurat, A., Leu, L., Enzmann, F., Schwarz, J.O., Kersten, M., Irvine, S., Stampanoni, M., 2013. Real-time 3D imaging of Haines jumps in porous media flow. Proc. Natl. Acad. Sci. U. S. A. 110, 3755–3759. https://doi.org/10.1073/pnas.1221373110

BERNAL, J.D., MASON, J., 1960. Packing of Spheres: Co-ordination of Randomly Packed Spheres. Nature 188, 910–911. https://doi.org/10.1038/188910a0

Blunt, M.J., 2017. Multiphase Flow in Permeable Media, Multiphase Flow in Permeable Media. Cambridge University Press, Cambridge. https://doi.org/10.1017/9781316145098

Blunt, M.J., Bijeljic, B., Dong, H., Gharbi, O., Iglauer, S., Mostaghimi, P., Paluszny, A., Pentland, C., 2013. Pore-scale imaging and modelling. Adv. Water Resour. 51, 197–216. https://doi.org/10.1016/j.advwatres.2012.03.003

Boretti, A., Rosa, L., 2019. Reassessing the projections of the World Water Development Report. npj Clean Water 2. https://doi.org/10.1038/s41545-019-0039-9

Bradford, S.A., Abriola, L.M., 2001. Dissolution of residual tetrachloroethylene in fractional wettability porous media: Incorporation of interfacial area estimates. Water Resour. Res. 37, 1183–1195. https://doi.org/10.1029/2000WR900374

Bradford, S.A., Phelan, T.J., Abriola, L.M., 2000. Dissolution of residual tetrachloroethylene in fractional wettability porous media: Correlation development and application. J. Contam. Hydrol. 45, 35–61. https://doi.org/10.1016/S0169-7722(00)00118-2

Bradford, S.A., Rathfelder, K.M., Lang, J., Abriola, L.M., Brown, G.E., 2003. Entrapment and dissolution of DNAPLs in heterogeneous porous media. J. Contam. Hydrol. 67, 133–157. https://doi.org/10.1016/S0169-7722(03)00071-8

Bradford, S.A., Vendlinski, R.A., Abriola, L.M., 1999. The entrapment and long-term dissolution of tetrachloroethylene in fractional wettability porous media. Water Resour. Res. 35, 2955–2964. https://doi.org/10.1029/1999WR900178

Brusseau, M.L., Narter, M., Schnaar, G., Marble, J., 2009. Measurement and estimation of organic-liquid/water interfacial areas for several natural porous media. Environ. Sci. Technol. 43, 3619–3625. https://doi.org/10.1021/es8020827

Buades, A., Coll, B., Morel, J.-M., 2011. Non-Local Means Denoising. Image Process. Line 1, 208–212. https://doi.org/10.5201/ipol.2011.bcm_nlm

Chang, C., Zhou, Q., Kneafsey, T.J., Oostrom, M., Ju, Y., 2019. Coupled supercritical CO_2 dissolution and water flow in pore-scale micromodels. Adv. Water Resour. 123, 54–69. https://doi.org/10.1016/j.advwatres.2018.11.004

Chang, C., Zhou, Q., Kneafsey, T.J., Oostrom, M., Wietsma, T.W., Yu, Q., 2016. Pore-scale supercritical CO_2 dissolution and mass transfer under imbibition conditions. Adv. Water Resour. 92, 142–158. https://doi.org/10.1016/j.advwatres.2016.03.015

Chen, Y.F., Fang, S., Wu, D.S., Hu, R., 2017. Visualizing and quantifying the crossover from capillary fingering to viscous fingering in a rough fracture. Water Resour. Res. 53, 7756–7772. https://doi.org/10.1002/2017WR021051

Chen, Y.F., Wu, D.S., Fang, S., Hu, R., 2018. Experimental study on two-phase flow in rough fracture: Phase diagram and localized flow channel. Int. J. Heat Mass Transf. 122, 1298–1307. https://doi.org/10.1016/j.ijheatmasstransfer.2018.02.031

Chomsurin, C., Werth, C.J., 2003. Analysis of pore-scale nonaqueous phase liquid dissolution in etched silicon pore networks. Water Resour. Res. 39, 1265. https://doi.org/10.1029/2002WR001643

Corapcioglu, M.Y., Yoon, S., Chowdhury, S., 2009. Pore-Scale Analysis of NAPL Blob Dissolution and Mobilization in Porous Media. Transp. Porous Media 79, 419–442. https://doi.org/10.1007/s11242-008-9331-8

Dalla, E., Hilpert, M., Miller, C.T., 2002. Computation of the interfacial area for two-fluid porous medium systems. J. Contam. Hydrol. 56, 25–48. https://doi.org/10.1016/S0169-7722(01)00202-9

Darbon, J., Cunha, A., Chan, T.F., Osher, S., Jensen, G.J., 2008. Fast nonlocal filtering applied to electron cryomicroscopy, in: 2008 5th IEEE International Symposium on Biomedical Imaging: From Nano to Macro, Proceedings, ISBI. IEEE, 1331–1334. https://doi.org/10.1109/ISBI.2008.4541250

Datta, S.S., Ramakrishnan, T.S., Weitz, D.A., 2014. Mobilization of a trapped non-wetting fluid from a three-dimensional porous medium. Phys. Fluids 26, 022002. https://doi.org/10.1063/1.4866641

Dias, M.M., Wilkinson, D., 1986. Percolation with trapping. J. Phys. A Gen. Phys. 19, 3131–3146. https://doi.org/10.1088/0305-4470/19/15/034

Eggersdorfer, M.L., Kadau, D., Herrmann, H.J., Pratsinis, S.E., 2011. Multiparticle sintering dynamics: From fractal-like aggregates to compact structures. Langmuir 27, 6358–6367. https://doi.org/10.1021/la200546g

Emami-Meybodi, H., Hassanzadeh, H., Green, C.P., Ennis-King, J., 2015. Convective dissolution of CO_2 in saline aquifers: Progress in modeling and experiments. Int. J. Greenh. Gas Control 40, 238–266. https://doi.org/10.1016/j.ijggc.2015.04.003

Ferer, M., Ji, C., Bromhal, G.S., Cook, J., Ahmadi, G., Smith, D.H., 2004. Crossover from capillary fingering to viscous fingering for immiscible unstable flow:Experiment and modeling. Phys. Rev. E - Stat. Physics, Plasmas, Fluids, Relat. Interdiscip. Top. 70, 7. https://doi.org/10.1103/PhysRevE.70.016303

Gao, Y., Lin, Q., Bijeljic, B., Blunt, M.J., 2020. Pore-scale dynamics and the multiphase Darcy law. Phys. Rev. Fluids 5, 13801. https://doi.org/10.1103/PhysRevFluids.5.013801

Geistlinger, H., Ataei-Dadavi, I., Mohammadian, S., Vogel, H.J., 2015. The impact of pore structure and surface roughness on capillary trapping for 2-D and 3-D porous media:

Comparison with percolation theory. Water Resour. Res. 51, 9094–9111. https://doi.org/10.1002/2015WR017852

Geistlinger, H., Ataei-Dadavi, I., Vogel, H.J., 2016. Impact of Surface Roughness on Capillary Trapping Using 2D-Micromodel Visualization Experiments. Transp. Porous Media 112, 207–227. https://doi.org/10.1007/s11242-016-0641-y

Geistlinger, H., Beckmann, A., Lazik, D., 2005. Mass transfer between a multicomponent trapped gas phase and a mobile water phase: Experiment and theory. Water Resour. Res. 41, 1–15. https://doi.org/10.1029/2004WR003885

Geistlinger, H., Mohammadian, S., 2015. Capillary trapping mechanism in strongly water wet systems: Comparison between experiment and percolation theory. Adv. Water Resour. 79, 35–50. https://doi.org/10.1016/j.advwatres.2015.02.010

Geistlinger, H., Mohammadian, S., Schlueter, S., Vogel, H.-J.J., 2014. Quantification of capillary trapping of gas clusters using X-ray microtomography. Water Resour. Res. 50, 4514–4529. https://doi.org/10.1002/2013WR014657

Geistlinger, H., Zulfiqar, B., 2020. The Impact of Wettability and Surface Roughness on Fluid Displacement and Capillary Trapping in 2-D and 3-D Porous Media: 1. Wettability-Controlled Phase Transition of Trapping Efficiency in Glass Beads Packs. Water Resour. Res. 56, 1–15. https://doi.org/10.1029/2019WR026826

Geller, J.T., Hunt, J.R., 1993. Mass transfer from nonaqueous phase organic liquids in water-saturated porous media. Water Resour. Res. 29, 833–845. https://doi.org/10.1029/92WR02581

Georgiadis, A., Berg, S., Makurat, A., Maitland, G., Ott, H., 2013. Pore-scale micro-computed-tomography imaging: Nonwetting-phase cluster-size distribution during drainage and imbibition. Phys. Rev. E - Stat. Nonlinear, Soft Matter Phys. 88, 1–9. https://doi.org/10.1103/PhysRevE.88.033002

Gostick, J., Aghighi, M., Hinebaugh, J., Tranter, T., Hoeh, M.A., Day, H., Spellacy, B., Sharqawy, M.H., Bazylak, A., Burns, A., Lehnert, W., Putz, A., 2016. OpenPNM: A Pore Network Modeling Package. Comput. Sci. Eng. 18, 60–74. https://doi.org/10.1109/MCSE.2016.49

Grate, J.W., Zhang, C., Wietsma, T.W., Warner, M.G., Anheier, N.C., Bernacki, B.E., Orr, G., Oostrom, M., 2010. A note on the visualization of wetting film structures and a nonwetting immiscible fluid in a pore network micromodel using a solvatochromic dye. Water Resour. Res. 46, 1–6. https://doi.org/10.1029/2010WR009419

Guo, C., Wang, X., Wang, H., He, S., Liu, H., Zhu, P., 2018. Effect of pore structure on displacement efficiency and oil-cluster morphology by using micro computed tomography (MCT) technique. Fuel 230, 430–439. https://doi.org/10.1016/j.fuel.2018.05.058

Herring, A.L., Gilby, F.J., Li, Z., McClure, J.E., Turner, M., Veldkamp, J.P., Beeching, L., Sheppard, A.P., 2018. Observations of nonwetting phase snap-off during drainage. Adv. Water Resour. 121, 32–43. https://doi.org/10.1016/j.advwatres.2018.07.016

Herring, A.L., Harper, E.J., Andersson, L., Sheppard, A., Bay, B.K., Wildenschild, D., 2013.

Effect of fluid topology on residual nonwetting phase trapping: Implications for geologic CO_2 sequestration. Adv. Water Resour. 62, 47–58. https://doi.org/10.1016/j.advwatres.2013.09.015

Herring, A.L., Sheppard, A., Andersson, L., Wildenschild, D., 2016. Impact of wettability alteration on 3D nonwetting phase trapping and transport. Int. J. Greenh. Gas Control 46, 175–186. https://doi.org/10.1016/j.ijggc.2015.12.026

Hu, R., Wan, J., Kim, Y., Tokunaga, T.K., 2017a. Wettability effects on supercritical CO_2–brine immiscible displacement during drainage: Pore-scale observation and 3D simulation. Int. J. Greenh. Gas Control 60, 129–139. https://doi.org/10.1016/j.ijggc.2017.03.011

Hu, R., Wan, J., Kim, Y., Tokunaga, T.K., 2017b. Wettability impact on supercritical CO_2 capillary trapping: Pore-scale visualization and quantification. Water Resour. Res. 53, 6377–6394. https://doi.org/10.1002/2017WR020721

Hu, Y., Patmonoaji, A., Xu, H., Kaito, K., Matsushita, S., Suekane, T., 2021. Pore-scale investigation on nonaqueous phase liquid dissolution and mass transfer in 2D and 3D porous media. Int. J. Heat Mass Transf. 169, 120901. https://doi.org/10.1016/j.ijheatmasstransfer.2021.120901

Hu, Y., Patmonoaji, A., Zhang, C., Suekane, T., 2020a. Experimental study on the displacement patterns and the phase diagram of immiscible fluid displacement in three-dimensional porous media. Adv. Water Resour. 140, 103584. https://doi.org/10.1016/j.advwatres.2020.103584

Hu, Y., She, Y., Patmonoaji, A., Zhang, C., Suekane, T., 2020b. Effect of capillary number on morphological characterizations of trapped gas bubbles: Study by using micro-tomography. Int. J. Heat Mass Transf. 163, 120508. https://doi.org/10.1016/j.ijheatmasstransfer.2020.120508

IEA, 2012. World Energy Outlook.

Iglauer, S., Fernø, M.A., Shearing, P., Blunt, M.J., 2012. Comparison of residual oil cluster size distribution, morphology and saturation in oil-wet and water-wet sandstone. J. Colloid Interface Sci. 375, 187–192. https://doi.org/10.1016/j.jcis.2012.02.025

Iglauer, S., Paluszny, A., Blunt, M.J., 2013. Simultaneous oil recovery and residual gas storage: A pore-level analysis using in situ X-ray micro-tomography. Fuel 103, 905–914. https://doi.org/10.1016/j.fuel.2012.06.094

Iglauer, S., Pentland, C.H., Busch, A., 2015. CO_2 wettability of seal and reservoir rocks and the implications for carbon geo-sequestration. Water Resour. Res. 51, 729–774. https://doi.org/10.1002/2014WR015553

Imhoff, P.T., Jaffé, P.R., Pinder, G.F., 1994. An experimental study of complete dissolution of a nonaqueous phase liquid in saturated porous media. Water Resour. Res. 30, 307–320. https://doi.org/10.1029/93WR02675

IPCC, 2007. Climate change 2007: impacts, adaptation and vulnerability.

Jain, V., Bryant, S., Sharma, M., 2003. Influence of wettability and saturation on liquid - Liquid interfacial area in porous media. Environ. Sci. Technol. 37, 584–591.

https://doi.org/10.1021/es020550s

Jiang, F., Tsuji, T., Hu, C., 2014. Elucidating the Role of Interfacial Tension for Hydrological Properties of Two-Phase Flow in Natural Sandstone by an Improved Lattice Boltzmann Method. Transp. Porous Media 104, 205–229. https://doi.org/10.1007/s11242-014-0329-0

Jiang, L., Wu, B., Liu, Y., Suekane, T., Wang, D., 2019. Dynamic evolution of the CO_2-brine interfacial area during brine imbibition in porous media. Int. J. Heat Mass Transf. 128, 1125–1135. https://doi.org/10.1016/j.ijheatmasstransfer.2018.09.089

Jiang, L., Wu, B., Song, Y., Yang, M., Wang, D., Liu, Y., Xue, Z., 2017. Mass transfer coefficient measurement during brine flush in a CO2-filled packed bed by X-ray CT scanning. Int. J. Heat Mass Transf. 115, 615–624. https://doi.org/10.1016/j.ijheatmasstransfer.2017.08.012

Johns, M.L., Gladden, L.F., 2000. Probing ganglia dissolution and mobilization in a water-saturated porous medium using MRI. J. Colloid Interface Sci. 225, 119–127. https://doi.org/10.1006/jcis.2000.6742

Johns, M.L., Gladden, L.F., 1999. Magnetic resonance imaging study of the dissolution kinetics of octanol in porous media. J. Colloid Interface Sci. 210, 261–270. https://doi.org/10.1006/jcis.1998.5950

Johnson, G.R., Zhang, Z., Brusseau, M.L., 2003. Characterizing and quantifying the impact of immiscible-liquid dissolution and nonlinear, rate-limited sorption/desorption on low-concentration elution tailing. Water Resour. Res. 39, 1–8. https://doi.org/10.1029/2002WR001435

Joun, W.T., Lee, S.S., Koh, Y.E., Lee, K.K., 2016. Impact of Water Table Fluctuations on the Concentration of Borehole Gas from NAPL Sources in the Vadose Zone. Vadose Zo. J. 15, vzj2015.09.0124. https://doi.org/10.2136/vzj2015.09.0124

Karlsons, K., De Kort, D.W., Sederman, A.J., Mantle, M.D., Freeman, J.J., Appel, M., Gladden, L.F., 2021. Characterizing pore-scale structure-flow correlations in sedimentary rocks using magnetic resonance imaging. Phys. Rev. E 103, 23104. https://doi.org/10.1103/PhysRevE.103.023104

Kazemifar, F., Blois, G., Kyritsis, D.C., Christensen, K.T., 2016. Quantifying the flow dynamics of supercritical CO_2–water displacement in a 2D porous micromodel using fluorescent microscopy and microscopic PIV. Adv. Water Resour. 95, 352–368. https://doi.org/10.1016/j.advwatres.2015.05.011

Khishvand, M., Akbarabadi, M., Piri, M., 2016. Micro-scale experimental investigation of the effect of flow rate on trapping in sandstone and carbonate rock samples. Adv. Water Resour. 94, 379–399. https://doi.org/10.1016/j.advwatres.2016.05.012

Krummel, A.T., Datta, S.S., Münster, S., Weitz, D.A., 2013. Visualizing multiphase flow and trapped fluid configurations in a model three-dimensional porous medium. AIChE J. 59, 1022–1029. https://doi.org/10.1002/aic.14005

Landis, E.N., Keane, D.T., 2010. X-ray microtomography. Mater. Charact.61, 1305–1316. https://doi.org/10.1016/j.matchar.2010.09.012

Lenormand, R., Touboul, E., Zarcone, C., 1988. Numerical models and experiments on immiscible displacements in porous media. J. Fluid Mech. 189, 165–187. https://doi.org/10.1017/S0022112088000953

Liu, H., Valocchi, A.J., Kang, Q., Werth, C., 2013. Pore-Scale Simulations of Gas Displacing Liquid in a Homogeneous Pore Network Using the Lattice Boltzmann Method. Transp. Porous Media 99, 555–580. https://doi.org/10.1007/s11242-013-0200-8

Liu, H., Zhang, Y., Valocchi, A.J., 2015. Lattice boltzmann simulation of immiscible fluid displacement in porous media: Homogeneous versus heterogeneous pore network. Phys. Fluids 27, 052103. https://doi.org/10.1063/1.4921611

Liu, Z., McClure, J.E., Armstrong, R.T., 2018. Influence of wettability on phase connectivity and electrical resistivity. Phys. Rev. E 98, 043102. https://doi.org/10.1103/PhysRevE.98.043102

Lorenz, C.D., Ziff, R.M., 1998. Precise determination of the bond percolation thresholds and finite-size scaling corrections for the sc, fcc, and bcc lattices. Phys. Rev. E - Stat. Physics, Plasmas, Fluids, Relat. Interdiscip. Top. 57, 230–236. https://doi.org/10.1103/PhysRevE.57.230

Løvoll, G., Méheust, Y., Toussaint, R., Schmittbuhl, J., Måløy, K.J., 2004. Growth activity during fingering in a porous Hele-Shaw cell. Phys. Rev. E - Stat. Physics, Plasmas, Fluids, Relat. Interdiscip. Top. 70, 12. https://doi.org/10.1103/PhysRevE.70.026301

Mandelbrot, B.B., 1983. The Fractal Geometry of Nature. Freeman, New York. https://doi.org/10.2307/3615422

Mansoori, S. Al, Iglauer, S., Pentland, C.H., Bijeljic, B., Blunt, M.J., 2009. Measurements of Non-Wetting Phase Trapping Applied to Carbon Dioxide Storage. Energy Procedia 1, 3173–3180. https://doi.org/10.1016/j.egypro.2009.02.100

Middleton, R.S., Keating, G.N., Stauffer, P.H., Jordan, A.B., Viswanathan, H.S., Kang, Q.J., Carey, J.W., Mulkey, M.L., Sullivan, E.J., Chu, S.P., Esposito, R., Meckel, T.A., 2012. The cross-scale science of CO_2 capture and storage: From pore scale to regional scale. Energy Environ. Sci. 5, 7328–7345. https://doi.org/10.1039/c2ee03227a

Miller, C.T., Poirier-McNeil, M.M., Mayer, A.S., 1990. Dissolution of Trapped Nonaqueous Phase Liquids: Mass Transfer Characteristics. Water Resour. Res. 26, 2783–2796. https://doi.org/10.1029/WR026i011p02783

Morrow, N.R., Chatzis, I., Taber, J.J., 1988. Entrapment and mobilization of residual oil in bead packs. SPE Reserv. Eng. (Society Pet. Eng. 3, 927–934. https://doi.org/10.2118/14423-PA

Morrow, N.R., Songkran, B., 1982. Effect of Viscous and Bouyancy Forces on Nonwetting Phase Trapping in Porous Media. 387–411.

Nemer, M.N., Rao, P.R., Schaefer, L., 2020. Wettability alteration implications on pore-scale multiphase flow in porous media using the lattice Boltzmann method. Adv. Water Resour. 146, 103790. https://doi.org/10.1016/j.advwatres.2020.103790

Orr, F.M., 2009. Onshore geologic storage of CO_2. Science 325, 1656-8. https://doi.org/10.1126/science.1175677

Oughanem, R., Youssef, S., Bauer, D., Peysson, Y., Maire, E., Vizika, O., 2015. A Multi-Scale Investigation of Pore Structure Impact on the Mobilization of Trapped Oil by Surfactant Injection. Transp. Porous Media 109, 673–692. https://doi.org/10.1007/s11242-015-0542-5

Patmonoaji, A., Muharrik, M., Hu, Y., Zhang, C., Suekane, T., 2020. Three-dimensional fingering structures in immiscible flow at the crossover from viscous to capillary fingering. Int. J. Multiph. Flow 122, 2–12. https://doi.org/10.1016/j.ijmultiphaseflow.2019.103147

Patmonoaji, A., Suekane, T., 2017. Investigation of CO_2 dissolution via mass transfer inside a porous medium. Adv. Water Resour. 110, 97–106. https://doi.org/10.1016/j.advwatres.2017.10.008

Patmonoaji, A., Tsuji, K., Muharrik, M., Suekane, T., 2018. Micro-tomographic analyses of specific interfacial area inside unconsolidated porous media with differing particle characteristics from microscopic to macroscopic scale. J. Colloid Interface Sci. 532, 614–621. https://doi.org/10.1016/j.jcis.2018.08.023

Patmonoaji, A., Zhang, Y., Xue, Z., Park, H., Suekane, T., 2019. Experimental and numerical simulation of supercritical CO_2 microbubble injection into a brine-saturated porous medium. Int. J. Greenh. Gas Control 91, 102830. https://doi.org/10.1016/j.ijggc.2019.102830

Pentland, C.H., Itsekiri, E., Al Mansoori, S.K., Iglauer, S., Bijeljic, B., Blunt, M.J., 2010. Measurement of nonwetting-phase trapping in sandpacks. SPE J. 15, 274–281. https://doi.org/10.2118/115697-PA

Petri, B.G., Fučík, R., Illangasekare, T.H., Smits, K.M., Christ, J.A., Sakaki, T., Sauck, C.C., 2015. Effect of NAPL Source Morphology on Mass Transfer in the Vadose Zone. Groundwater 53, 685–698. https://doi.org/10.1111/gwat.12284

Powers, S.E., Abriola, L.M., Dunkin, J.S., Weber, W.J., 1994. Phenomenological models for transient NAPL-water mass-transfer processes. J. Contam. Hydrol. 16, 1–33. https://doi.org/10.1016/0169-7722(94)90070-1

Powers, S.E., Abriola, L.M., Weber, W.J., 1992. An experimental investigation of nonaqueous phase liquid dissolution in saturated subsurface systems: Steady state mass transfer rates. Water Resour. Res. 28, 2691–2705. https://doi.org/10.1029/92WR00984

Reddy, K.R., 2008. Physical and Chemical Groundwater Remediation Technologies, in: Overexploitation and Contamination of Shared Groundwater Resources. pp. 257–274. https://doi.org/10.1007/978-1-4020-6985-7_12

Saffman and Taylor, 1958. The penetration of a fluid into a porous medium or Hele-Shaw cell containing a more viscous liquid. Dyn. Curved Front. 155–174.

Scanziani, A., Singh, K., Menke, H., Bijeljic, B., Blunt, M.J., 2020. Dynamics of enhanced gas trapping applied to CO_2 storage in the presence of oil using synchrotron X-ray micro tomography. Appl. Energy 259, 114136. https://doi.org/10.1016/j.apenergy.2019.114136

Schnaar, G., Brusseau, M.L., 2006. Characterizing Pore-Scale Dissolution of Organic Immiscible Liquid in Natural Porous Media Using Synchrotron X-ray Microtomography.

Environ. Sci. Technol. 40, 6622–6629. https://doi.org/10.1021/es0602851

Setiawan, A., Suekane, T., Deguchi, Y., Kusano, K., 2014. Three-Dimensional Imaging of Pore-Scale Water Flooding Phenomena in Water-Wet and Oil-Wet Porous Media. J. Flow Control. Meas. & Vis. 02, 25–31. https://doi.org/10.4236/jfcmv.2014.22005

Seyedabbasi, M.A., Farthing, M.W., Imhoff, P.T., Miller, C.T., 2008. The influence of wettability on NAPL dissolution fingering. Adv. Water Resour. 31, 1687–1696.

Sheppard, A.P., Sok, R.M., Averdunk, H., 2004. Techniques for image enhancement and segmentation of tomographic images of porous materials. Phys. A Stat. Mech. its Appl. 339, 145–151. https://doi.org/10.1016/j.physa.2004.03.057

Sin, S., Suekane, T., Nagatsu, Y., Patmonoaji, A., 2019. Three-dimensional visualization of viscous fingering for non-Newtonian fluids with chemical reactions that change viscosity. Phys. Rev. Fluids 4, 054502. https://doi.org/10.1103/PhysRevFluids.4.054502

Singh, K., Menke, H., Andrew, M., Lin, Q., Rau, C., Blunt, M.J., Bijeljic, B., 2017. Dynamics of snap-off and pore-filling events during two-phase fluid flow in permeable media. Sci. Rep. 7, 1–13. https://doi.org/10.1038/s41598-017-05204-4

Speight, J.G., 2019. Natural water remediation: Chemistry and technology, Natural Water Remediation: Chemistry and Technology. Elsevier. https://doi.org/10.1016/C2013-0-16022-9

Stokes, J.P., Weitz, D.A., Gollub, J.P., Dougherty, A., Robbins, M.O., Chaikin, P.M., Lindsay, H.M., 1986. Interfacial stability of immiscible displacement in a porous medium. Phys. Rev. Lett. 57, 1718–1721. https://doi.org/10.1103/PhysRevLett.57.1718

Suekane, T., Nguyen, H.T., 2013. Relation between the Initial and Residual Gas Saturations of Gases Trapped by Capillarity in Natural Sandstones. J. Fluid Sci. Technol. 8, 322–336. https://doi.org/10.1299/jfst.8.322

Suekane, T., Zhou, N., Hosokawa, T., Matsumoto, T., 2010. Direct observation of trapped gas bubbles by capillarity in sandy porous media. Transp. Porous Media 82, 111–122. https://doi.org/10.1007/s11242-009-9439-5

Teramoto, E.H., Isler, E., Polese, L., Baessa, M.P.M., Chang, H.K., 2019. LNAPL saturation derived from laser induced fluorescence method. Sci. Total Environ. 683, 762–772. https://doi.org/10.1016/j.scitotenv.2019.05.262

Trojer, M., Szulczewski, M.L., Juanes, R., 2015. Stabilizing Fluid-Fluid Displacements in Porous Media Through Wettability Alteration. Phys. Rev. Appl. 3, 1–8. https://doi.org/10.1103/PhysRevApplied.3.054008

Tsuji, T., Jiang, F., Christensen, K.T., 2016. Characterization of immiscible fluid displacement processes with various capillary numbers and viscosity ratios in 3D natural sandstone. Adv. Water Resour. 95, 3–15. https://doi.org/10.1016/j.advwatres.2016.03.005

Wang, M., Xiong, Y., Liu, L., Peng, G., 2018. LBM Investigation of Immiscible Displacement in a Channel with Regular Surface Roughness. Transp. Porous Media 123, 195–215. https://doi.org/10.1007/s11242-018-1032-3

Wang, Y., Song, R., Liu, J.J., Cui, M.M., Ranjith, P.G., 2019. Pore scale investigation on

scaling-up micro-macro capillary number and wettability on trapping and mobilization of residual fluid. J. Contam. Hydrol. 225, 103499. https://doi.org/10.1016/j.jconhyd.2019.103499

Wardlaw, N.C., Yu, L., 1988. Fluid topology, pore size and aspect ratio during imbibition. Transp. Porous Media 3, 17–34. https://doi.org/10.1007/BF00222684

Werth, C.J., Zhang, C., Brusseau, M.L., Oostrom, M., Baumann, T., 2010. A review of non-invasive imaging methods and applications in contaminant hydrogeology research. J. Contam. Hydrol. 113, 1–24. https://doi.org/10.1016/j.jconhyd.2010.01.001

Wilkinson, D., 1984. Percolation model of immiscible displacement in the presence of buoyancy forces. Phys. Rev. A 30, 520–531. https://doi.org/10.1103/PhysRevA.30.520

Yamabe, H., Tsuji, T., Liang, Y., Matsuoka, T., 2015. Lattice boltzmann simulations of supercritical CO2-water drainage displacement in porous media: CO_2 saturation and displacement mechanism. Environ. Sci. Technol. 49, 537–543. https://doi.org/10.1021/es504510y

Yang, X., Scheibe, T.D., Richmond, M.C., Perkins, W.A., Vogt, S.J., Codd, S.L., Seymour, J.D., McKinley, M.I., 2013. Direct numerical simulation of pore-scale flow in a bead pack: Comparison with magnetic resonance imaging observations. Adv. Water Resour. 54, 228–241. https://doi.org/10.1016/j.advwatres.2013.01.009

Yiotis, A.G., Dollari, A., Kainourgiakis, M.E., Salin, D., Talon, L., 2019. Nonlinear Darcy flow dynamics during ganglia stranding and mobilization in heterogeneous porous domains. Phys. Rev. Fluids 4, 1–19. https://doi.org/10.1103/PhysRevFluids.4.114302

Zacharoudiou, I., Boek, E.S., Crawshaw, J., 2018. The impact of drainage displacement patterns and Haines jumps on CO_2 storage efficiency. Sci. Rep. 8, 1–13. https://doi.org/10.1038/s41598-018-33502-y

Zhang, C., Oostrom, M., Wietsma, T.W., Grate, J.W., Warner, M.G., 2011. Influence of viscous and capillary forces on immiscible fluid displacement: Pore-scale experimental study in a water-wet micromodel demonstrating viscous and capillary fingering. Energy & Fuels 25, 3493–3505. https://doi.org/10.1021/ef101732k

Zhang, C., Werth, C.J., Webb, A.G., 2002. A magnetic resonance imaging study of dense nonaqueous phase liquid dissolution from angular porous media. Environ. Sci. Technol. 36, 3310–3317. https://doi.org/10.1021/es011497v

Zhao, B., MacMinn, C.W., Juanes, R., 2016. Wettability control on multiphase flow in patterned microfluidics. Proc. Natl. Acad. Sci. U. S. A. 113, 10251–10256. https://doi.org/10.1073/pnas.1603387113

Zhao, J., Kang, Q., Yao, J., Viswanathan, H., Pawar, R., Zhang, L., Sun, H., 2018. The Effect of Wettability Heterogeneity on Relative Permeability of Two-Phase Flow in Porous Media: A Lattice Boltzmann Study. Water Resour. Res. 54, 1295–1311. https://doi.org/10.1002/2017WR021443

Zhao, W., Ioannidis, M.A., 2007. Effect of NAPL film stability on the dissolution of residual wetting NAPL in porous media: A pore-scale modeling study. Adv. Water Resour. 30, 171–181. https://doi.org/10.1016/j.advwatres.2005.03.025

Acknowledgement

First of all, I would like to express my sincere appreciation and gratitude to my supervisor Prof. Suekane Tetsuya. This dissertation would not have been possible, without his guidance, advice and encouragement in the past three years. He not only taught me professional knowledge related my research work, but also guided me on how to think logically and solve problems efficiently. He always encouraged us to conduct novel and challenging research instead of following hot topics. His influence has been instrumental to my personal development as a young researcher, and this influence will accompany me throughout my career. To my mind, he is the best supervisor a student could ask for.

Outside of work, he is also the best role model. When I am typing this part, many unforgettable memories come to my mind, such as the Nomikai in izakaya, the Momiji in Kamakura, the private party in his home. We spent a lot of time sharing each other's daily stories like friends. He impressed me that he never confuses having a career with having a life. He insists on long-distance cycling and hiking on weekends for many years.

Secondly, I sincerely thank all the members and alumni of the Suekane Lab for their precious input to my research and for the great time I have had in Tokyo. I would like to express a special thanks to Dr. Anindityo Patmonoaji, whose expertise in experimental techniques was hugely helpful in the early stages of my Ph.D. Chunwei Zhang as a doctoral student who joined the lab the same year, we always fight side by side. Yun She assisted in part of the experimental works and deserves a special thank.

Thirdly, thanks to my motherland and the China Scholarship Council for funding me the entire period of studying at Tokyo Tech.

Finally, I would like to thank my parents, parents-in-law and sister's family for their unwavering love and support. My heartfelt thanks to my wife, Yaqian, who has stood by me through the joy and pain. She gave me support, help, and sometimes caused some trouble. The three-year Ph.D. journey has been the best three years of my life. Without her company, I cannot imagine how tough it would be.

Appendixes

Appendix 1. Visualization technologies

Understanding the fluid structure and flow dynamics in porous media is important in many natural and industrial processes. Visualization technology has made great progress in detecting what happens in pores, providing insights for revealing the underlying mechanism and benchmark data for larger-scale modeling (Blunt et al., 2013). Fig. A1 presents several typical imaging methods using for investigating multiphase flow in porous media. These technologies can provide a direct observation on one-dimensional (1D), two-dimensional (2D) and three-dimensional (3D) processes occurring in porous media from pore to core scale. In this thesis, we mainly focus on the pore-scale behavior in 3D porous media.

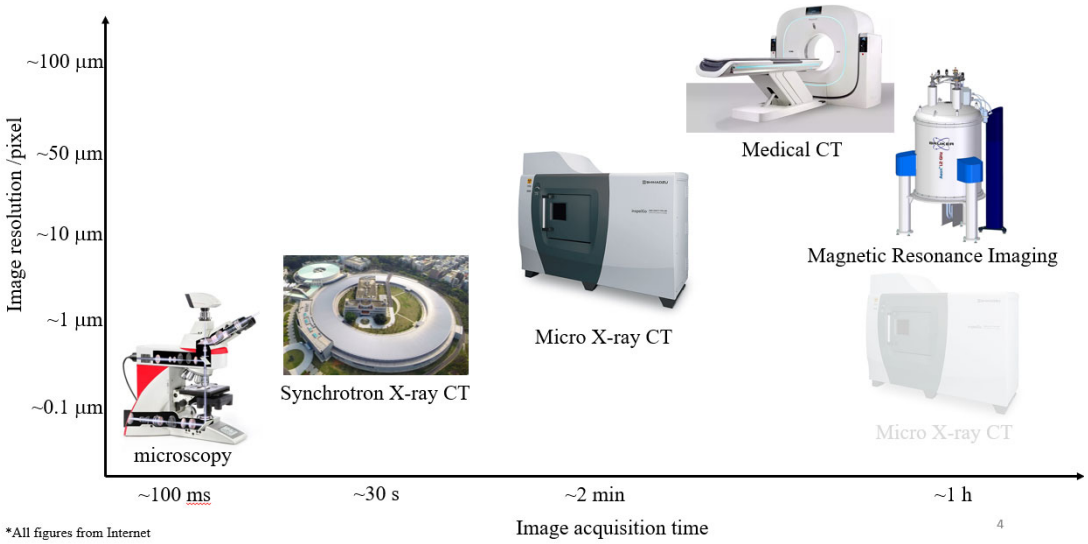

Figure A1. Several typical visualization technologies.

Appendix 2. Visualization technologies for 2D media

The most accessible visualization technology is an optical system integrating with a microscope and a camera. The spatial and temporal resolutions of the optical system are the highest among these visualization technologies presented in Fig. A1. The high resolution enables a pore-level observation of fluid flow under transient conditions in a transparent micromodel. Depending on the research purposes, the micromodel can be designed into the simplest lattices or real rock shapes. The designed flow paths were etched in an optically

transparent plate, such as glass and some polymer materials. Generally, the depth of the etching channels is only tens of micrometers, and the micromodel can be regarded as a 2D structure. Although some new concepts have been proposed to fabricate 2.5D or 3D micromodels by using additive or non-additive manufacturing, the pore connectivity in the micromodel is still much simpler than that in real rock. For detailed information on fabrication and applications of 2D and 3D micromodel, readers can refer to a review (Anbari et al., 2018).

Appendix 3. Visualization technologies for 3D media

To resolve the limitation of the micromodel, nondestructive visualization technology was developed to detect the inside information in realistic porous media. Three of the most common methods are confocal microscopy, magnetic resonance imaging (MRI), and X-ray computed tomography (CT), which are considered to be useful tools for investigating pore-scale multiphase flow inside 3D porous media. With the aid of these technologies, many traditional research fields have gained new insights, including pore and throat characterization, multiphase fluid distribution, local fluid velocities, solute transport and mixing, mass transfer, and chemical reactions. Werth et al. summarized several non-invasive imaging methods, applications in the contaminant hydrogeology field (Werth et al., 2010). By comparing the pros and cons of these methods, they made a conclusion that there is no perfect method or tool for nondestructive imaging.

Confocal laser scanning microscopy only can be used to scan the inner cross-sections of the media. To obtain the 3D fluid structure, the stack of 2D images was obtained by moving the focus plane, and then reconstructed into a 3D object (Anbari et al., 2018). Since the scattering of light from surfaces of solid particles may preclude direct observation, this method requires the refractive indices of fluids to carefully match with that of the solid matrix. In other words, this method is only suitable for specific fluid pairs and transparent solid substrates. This feature limits its application in environmental and energy fields, which mainly involve opaque rocks and soils.

MRI has flexible spatial and temporal resolutions (See Fig. A1). Although it can obtain fast image pulse sequences within seconds, it takes tens of minutes to hours to obtain high-resolution 3D volumetric imaging. Compared with other non-invasive technologies, MRI has a very specific function that it can measure local fluid velocities in 3D artificial porous media with a high spatial resolution (Karlsons et al., 2021; Yang et al., 2013). However, the imaging

principle of MRI limits its wide application in engineering. MRI signal is attenuated by ferromagnetic materials, and by paramagnetic species when present in sufficient quantities (Werth et al., 2010). When MRI is used to detect the multiphase flow inside porous media, solid matrix must be a low-content ferromagnetic material, such as glass beads, silica gel or quartz sand. Although a longer acquisition time can produce a higher spatial resolution, the achievable resolution is tens of micrometers, which is insufficient for geophysical processes (Zhang et al., 2002).

X-ray CT has the strongest penetrating ability and highest spatial resolution among these 3D nondestructive visualization technologies. These advantages contribute it to be the most widely used in geophysical processes. Recently, digital rock analysis combining pore-scale imaging with advanced numerical simulation has become a routine procedure in the oil and gas industry (Blunt et al., 2013). The basic procedures of X-ray acquisition and reconstruction processes as shown in Fig. A2. The absorption of X-rays after passing through the object is received by the scintillator, and then converted into visible light to be captured by the detector. By rotating the object, a series of 2D projections captured at different angles can be recoded. The 3D object is reconstructed from these projections using a tomographic reconstruction algorithm.

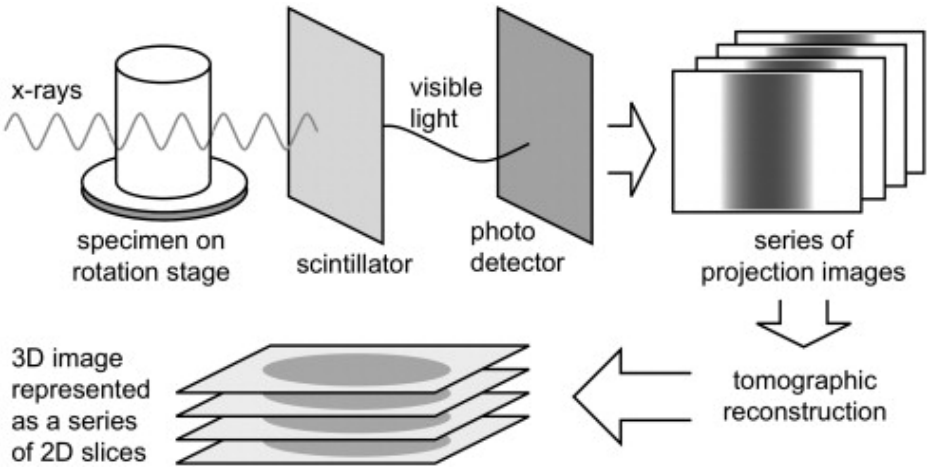

Figure A2. Schematic illustration of X-ray CT acquisition and reconstruction processes (Landis and Keane, 2010).

Depending on the X-ray source and usage, the three most common CTs used to study multiphase flow in porous media are medical CT, lab-based micro-CT, and synchrotron CT. Medical CT has the lowest spatial resolution and is usually used to scan core plugs obtained

from oil reservoirs in EOR and CCS (Patmonoaji et al., 2019). The saturation and distribution of the residual phase inside the core are determined by the volume average of the image gray. The resolution of medical CT is tens to hundreds of micrometers and is insufficient to observe the pore-scale processes. As shown in Fig. A1, synchrotron CT has a very high spatial resolution (a few micrometers) and high temporal resolution (a few seconds). Therefore, it provides an efficient way to explore the dynamics behavior of multiphase flow in pore space, such as snap-off (Singh et al., 2017), Haines jumps (Berg et al., 2013), ganglia mobilization (Armstrong et al., 2014) and intermittent flow (Gao et al., 2020). As the state-of-the-art technology, its high cost makes it not accessible to everyone. Japan has the world's largest third-generation synchrotron radiation facility, Spring-8. However, only a small part of the research proposal is approved to use the high-energy equipment.

The lab-based micro-CT is the widest tool to determine the multiphase flow in 3D porous media at pore level, due to its good balance between cost and image resolution. A longer acquisition time can produce a higher spatial resolution. For instance, images with a spatial resolution of about 1 μm/pixel need an acquisition time of about 2 hours (Scanziani et al., 2020). When the spatial resolution increases to 15 μm/pixel, the acquisition time can reduce to only 75 seconds (Patmonoaji and Suekane, 2017). In this study, the experiments were conducted in a ScanXmate-RB090SS and a ScanXmate-RB090SS micro-CT scanner in our laboratory. Fig. A3 illustrates the inside structure of the laboratory-based ScanXmate-RB090SS micro-CT scanner. It consists of a sealed X-ray transmission source, a rotation sample stage, and a flat panel detector. The scanner provides two rotation models, namely static model and dynamic model. In the static model, the sample fixed on the stage is rotated 360 degrees to acquire a series of projections. In the dynamic model, the sample is fixed in the middle and the X-ray source and detector in a circle during the scanning. When performing a fast scan, the dynamic model can avoid the rearrangement of fluids distribution in the sample that may be caused by the centrifugal force.

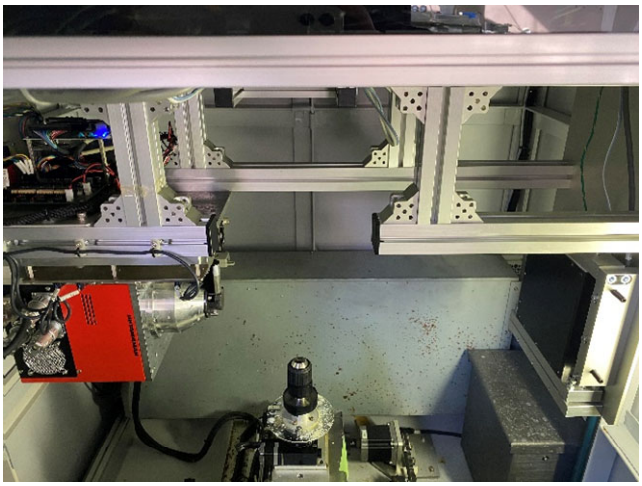

Figure A3. The lab-based ScanXmate-RB090SS micro-CT scanner with the flat panel.

After the CT scan, the collected projection will be reconstructed using the built-in software. Then, a series of slices (usually XY plane) is output for further process. Images need to be cropped, filtering, segmentation, and data processing. The detailed procedures of the image process are different for different research purposes. Thus, we described the detailed information of image processing in each separate chapter.